



UNIVERSITÀ DI PISA

**Dipartimento di Fisica
Corso di Laurea in Astronomia e Astrofisica**

MASTER THESIS

**Investigating the star formation
history of galaxies in the first
billion years of the Universe**

Supervisor:
Dott. Stefano Carniani

Supervisor:
Prof. Michele Cignoni

Candidate:
Pietro Benotto

Academic year 2023/2024

*To each one of you
who helped shape the person I am today*

“Or perhaps we’ve just forgotten that we are still pioneers.
And we’ve barely begun”

Interstellar teaser trailer

In this thesis, I determined the star formation histories of a sample of galaxies at redshift $z > 6$ through the technique of the spectral energy distribution (SED) fitting applied to spectroscopic data obtained with the JWST NIRSpec spectrograph. The main goals were to characterize the history of star formation, estimate the properties of these galaxies, investigate correlations between their inferred properties, and compare them with theoretical models. The SED fitting method compares the observed SEDs (photometric and/or spectrophotometric measurements) of individual galaxies to a grid of spectroscopic templates generated using various models such as stellar population, dust and initial mass functions models. Such models are combined to create a template spectrum that matches the experimental data. The combination of the grid of models depends on a set of free parameters that are constrained in the fitting process. In this thesis, the free parameters fitted by the SED fitting were the star formation history, dust attenuation, ionization parameter, gas-phase metallicity and stellar age.

I analyzed the spectra of the largest sample of galaxies observed so far with NIRSpec obtained in the observing program JADES. I used the code BAGPIPES to perform the SED fitting on the spectroscopic data. However, this code is not optimized for the NIRSpec data and the input models adopted to reproduce the emission line from the interstellar medium are not adequate for primordial galaxies. Therefore I modified the code to ingest NIRSpec data taking into account the characteristics of the spectrograph (i.e., spectral resolution as a function of wavelength), and provided a new grid of models for emission lines with the code CLOUDY by using a new set of parameters. Finally, I determined the biases of BAGPIPES by running the code on a set of mock galaxies and comparing the results with the input data.

Based on the SED fitting results, I found that massive galaxies present higher dust extinctions: in galaxies that formed in a characteristic time longer than 50 Myr the dust extinction in the visible band is $A_V > 0.1$ only for galaxies with a stellar mass $M_\star \gtrsim 10^{8.5} M_\odot$. Galaxies that formed in less than 50 Myr present $A_V > 0.1$ for stellar mass $M_\star \gtrsim 10^{7.5} M_\odot$. Some theories predict that galaxies that formed stars with a specific star formation rate¹ greater than $\text{sSFR} \gtrsim 25 \text{ Gyr}^{-1}$ may experience a strong radiation field from starlight able to push away the dust produced by stars and resulting in unextinct galaxies. This theory was proposed to explain the unexpectedly high number of bright galaxies detected at high redshift. However, I found no evidence of dust-free galaxies caused by high specific star formation rates. Instead, the analysis revealed that

¹The specific star formation rate is the ratio between the rate of star formation and the stellar mass of the galaxy

galaxies with $\text{sSFR} \gtrsim 25 \text{ Gyr}^{-1}$ are more extinct on average.

Further analysis of the inferred properties of galaxies allowed me to determine that the characteristic time of star formation depends on both mass and redshift. Less massive and higher redshift galaxies formed, on average, in a shorter time. The correlation between the time it takes for stars to form, their mass, and their redshift is challenging to measure. Indeed I needed to account for the bias caused by the sensitivity limit of the NIRSpec instrument, which restricts the observation of galaxies that formed slowly and the one that contains more dust. I measured the average time of formation of galaxies with stellar masses $10^{7.2} \leq M_\star [\text{M}_\odot] < 10^8$ to be 41_{-8}^{+14} Myr at redshift $6 < z < 7.5$ and 14_{-3}^{+4} Myr at redshift $8 < z < 11$. Analogously, for galaxies more massive than $M_\star \gtrsim 10^8 \text{ M}_\odot$ the measured characteristic time of star formation passes from $0.4_{-0.1}^{+0.1}$ Gyr to $0.06_{-0.02}^{+0.06}$ Gyr in the same redshift ranges. This result suggests that, at higher redshifts, galaxies tend to have higher specific star formation rates.

I also found $\approx 20\%$ of the analyzed galaxies exhibiting bursts of high star formation interspersed with periods of shallow star formation. The percentage found is five to seven times higher than what is currently expected from cosmological simulations at redshift $z \sim 6$. In general, such galaxies experienced periods of low ($\text{SFR} < 5 \times 10^2 \text{ M}_\odot/\text{yr}$) star formation rates which last on average 100 Myr but that can be as fast as 10 Myr or last for more than 300 Myr in the most extreme cases. The obtained star formation histories tend to exclude the presence in the analyzed galaxies of multiple bursts attributable to almost feedback-free star formation theories.

The results obtained in this thesis represent only the beginning of the investigation into the star formation histories (SFH) and their relation to the physical properties of early galaxies. Firstly, a larger sample of spectroscopic data would provide a better characterization of galaxy properties and reduce the uncertainties of the results. Furthermore, many galaxies in our sample showed significantly different results in their SED fitting when the oxygen emission lines were excluded from the observed spectrum. It is crucial to understand whether the emission of the interstellar medium is adequately reproduced with current models. The analysis of this thesis suggested that the current models are unable to reproduce the high luminosity of the oxygen lines without invoking extreme conditions in the interstellar medium. Finally, another prospect of this thesis will be to analyze the spectrum of these early galaxies with different SED fitting codes, looking for limitations and reliability of the results found.

Contents

• Introduction	9
1 Cosmology and galaxy formation	13
1.1 The cosmological framework	13
1.2 The Hubble parameter	14
1.2.1 Redshift and Hubble's law	14
1.2.2 Cosmological distances	16
1.3 The evolution of the Universe	17
1.3.1 The Friedmann equations	17
1.3.2 The cosmological parameters	18
1.4 Key moments in the history of the Universe	19
1.5 Linear structure growth	20
1.5.1 Subhorizon linearized fluid equations	21
1.5.2 Superhorizon growth	23
1.6 Nonlinear structure growth	24
1.7 Press-Schechter theory	27
1.8 The stellar mass function	30
1.9 Stellar feedback	32
1.10 Dust	34
2 The <i>Blue monsters</i> problem	39
2.1 Evidences of super-early galaxies	40
2.1.1 The ultraviolet luminosity function	40
2.1.2 The ultraviolet continuum slope	41
2.2 The UV luminosity function issue: proposed theories	42
2.2.1 Changes to the cosmological framework	43
2.2.2 Evolving initial mass function	44
2.2.3 Stochastic star formation rates	45
2.2.4 Almost feedback-free star-formation	46
2.2.5 Brightening due to low dust attenuation	46
3 The James Webb Space Telescope and JADES data	51
3.1 JWST	51
3.2 NIRSpec	53
3.2.1 The multi-object spectroscopy mode	53
3.2.2 NIRSpec dispersers	54

3.3	Data reduction	56
3.4	JADES	61
3.5	Data selection	62
3.6	Resolving power	63
4	Data analysis	67
4.1	Bagpipes	67
4.1.1	Stellar population models	68
4.1.2	Dust extinction	71
4.1.3	Nebular emission	71
4.1.4	Star formation history shapes	72
4.1.5	Fitting bursty star	76
4.2	Fine adjustments to the resolving power	76
4.3	Oxygen lines issue	78
4.3.1	Reliability of metallicity measurements	80
4.4	Electron density	81
4.4.1	Direct measurement of electron density	82
4.5	Dust content and Balmer decrement	84
5	Results	91
5.1	Inferred properties of the sample	91
5.2	Star formation histories	93
5.2.1	Burstiness of the star formation history	93
5.2.2	Mini-quenching evidences	93
5.2.3	Characteristics of the SFH	96
5.3	Dust and super-Eddington galaxies	98
5.3.1	Mass - sSFR - dust extinction	99
5.3.2	Redshift - sSFR - mass	102
6	Summary and conclusions	107
•	Acknowledgments	111
•	Bibliography	113

Introduction

Prior to the launch of the *James Webb Space Telescope* (JWST), only a few dozen galaxies had been identified within the first 700 Myr of the Universe using the Hubble Space Telescope. The farthest known galaxy was at a redshift² $z \sim 11$ (Jiang et al. 2021). However, the early-Universe landscape changed with the advent of the JWST. During the first two years of operations, the JWST has detected numerous super-early galaxy photometric candidates (Adams et al. 2023, Naidu et al. 2022, Finkelstein et al. 2022, Castellano et al. 2022, Donnan et al. 2023) with the exceptional discovery of a spectroscopically confirmed galaxy at redshift $z = 14.3$ (Carniani et al. 2024).

The first few hundred million years after the Big Bang is the epoch in which the first galaxies were born, outlining a separation between a dark Universe permeated by neutral hydrogen to the formation of the first stars and galaxies that populate the Universe as we know it today. In less than one billion years the newly formed stars emitted enough radiation to almost completely ionize the atomic hydrogen in the entire Universe (Dayal & Ferrara 2018). The study of super-early galaxies is the key to understanding the infancy of the Universe.

One of the already reached results of the JWST mission is the discovery of a high number of bright³ ($M_{\text{UV}} \gtrsim 22$) and blue galaxies (Finkelstein et al. 2023, McLeod et al. 2024; see Chapter 2). The high number of bright galaxies and their strong ultraviolet (UV) emission is puzzling the astrophysicists: these galaxies are more numerous than what was previously expected from extrapolation of observations at lower redshift and numerical simulations and pose a serious challenge to essentially all galaxy evolution models (Mason et al. 2023, Di Cesare et al. 2023, Mirocha & Furlanetto 2023, Gong et al. 2023, Furlanetto & Mirocha 2023).

To study the physical properties of galaxies, to put constraints on the theories that have been developed to explain the abundance of luminous galaxies, we have to rely on the light coming from these far sources. For non-local galaxies it is impossible

²The redshift z is defined as the fractional change in the observed wavelength of light λ_o compared to its wavelength when emitted λ_e : $z = \frac{\lambda_o - \lambda_e}{\lambda_e}$. In this context, the redshift is linked to the expansion of the Universe (Sec. 1.2)

³Here we are considering the AB magnitude at 1500 Å which is defined as:

$$m_{AB} = -2.5 \log_{10} f_\nu - 48.60 \quad (1)$$

where f_ν is the observed flux density of the source at 1500 Å expressed in $\text{erg s}^{-1}\text{cm}^{-2}\text{Hz}^{-1}$. The absolute magnitude of an object is the magnitude it would have if it was at a distance of 10 parsecs.

to directly study the light coming from single stars, what can be done instead is to spectroscopically analyze the integrated light coming from the entire galaxy (or a portion of it). The observed spectrum contains lots of physical information. In the optical and UV rest-frame frequencies the light we observe comes from a multitude of mechanisms, such as the starlight, which is the sum of the light from all the stars in the galaxy with different ages and masses, the dust absorption, the nebular emission, the absorption from neutral medium in front of the object, AGN and outflows emission. Every physical process occurring in the galaxy has its own more or less characteristic signature visible on the spectrum. When analyzing the light coming from an entire galaxy a SED fitting (Walcher et al. 2011, Conroy 2013) can be performed. This methodology consists of comparing the observed SEDs (photometric and/or spectrophotometric measures) of individual galaxies to existing galactic templates based on various models (stellar population models, dust models, initial mass function, etc.) to ultimately estimate the physical properties of such galaxies. The creation of a galactic spectrum through the sum of the spectra of its stars is called stellar population synthesis and was pioneered by Searle et al. 1973, Larson & Tinsley 1978. After having modeled the effects of each process involved in creating the observed spectrum, the free parameters of the fitting are tuned to obtain the best fit. In SED fitting, like any other fit, some parameters are fixed by the physics, while others are left as free parameters and returned by the fit. Among the others, one of the results a SED fitting can retrieve is the star formation history (SFH) of the observed object. The SFH analysis offers a unique window into the early Universe, providing insights into the formation and evolution of galaxies, as well as shedding light on the processes that shaped the cosmos in the different Universe's eras.

Initially, only photometric measures of SEDs were performed, nowadays the state-of-art is (when possible) to fit the spectrum of the object (Pacifici et al. 2023), which contains much more information on the object itself than photometry and helps to reduce the degeneracy between the parameters (e.g. Zavala et al. 2023, Bisigello et al. 2016).

The most visible features in the rest-frame optical and UV frequencies of a galaxy spectrum that can track the SFH are: high UV fluxes ($\lambda \lesssim 300$ nm rest frame) and a big UV slope are key indicators of recent ($\lesssim 100$ Myr) star formation. Prominent emission lines can be tracers of H_α regions and therefore of very young star formation ($\lesssim 10$ Myr). The Balmer break, visible as a discontinuity of the spectrum at 364 nm, is instead visible for older (200 – 800 Myr) populations.

On the other hand, a spectrophotometry SED fitting is more powerful because it can use the entire spectrum to infer the physical properties of the analyzed galaxy. Nevertheless, even with the spectra, the SED fitting is not perfect: because of the intrinsic uncertainties of the data, some degeneracy remains, like the age-dust degeneracy (Pacifici et al. 2023). Indeed, using only the rest-frame optical part of the spectrum, a dust-free galaxy spectrum can appear similar to the one of a very young population.

This is why the process of SFH retrieving must always be done considering the physical environment.

Moreover, the retrieval of the SFH is particularly delicate at high redshifts: even if the history of these objects is short, and so in principle easier to recover, the burstiness of the star formation is high ([Tacchella et al. 2016](#), [Faucher-Giguère 2018](#), [Dome et al. 2024a](#)) and recent episodes of star formation, with their brightness, can cast a shadow on past phenomena and return large uncertainties in the stellar masses of the analyzed galaxies. The SFH prior selection to perform the fits at such a high redshift is still an unexplored field, and validating the possibility of a bursty star formation would require physical constraints very different from their more steady counterpart at lower redshift (e.g. [Leja et al. 2017](#)).

The best instrument we can use nowadays to perform SED fitting of these objects is the JWST NIRspec ([Jakobsen et al. 2022](#), [Ferruit et al. 2022](#)), which provides near-IR spectroscopy from $0.6\text{ }\mu\text{m}$ to $5.3\text{ }\mu\text{m}$. In combination with the prism disperser, which can cover the full bandwidth, it is the perfect instrument for SFH studies: due to its wavelength range, at high redshift it can reveal both some important bright rest-frame optical emission lines (like H α for $z \lesssim 8$, H β and [OIII] for $z \lesssim 10.5$) both the stellar continuum. Moreover, it can be used even on high redshift faint objects thanks to its low dispersion.

In performing a SED fitting the continuum is particularly important, because it is dominated by the light from the stars and the λ -dependent absorption from the dust. Absorption lines are produced in stellar atmospheres and generally from neutral gas in front of the source, while emission lines in these wavelengths are mainly produced by recombination in ionized regions (H α regions, outflows, AGNs, ...), this is the reason for which a spectrometer with lower-resolution capable of catching all these characteristics is the best for SED fitting. In particular, at redshift $5 < z < 14$ both the Lyman alpha frequency and the Balmer break are accessible from NIRSpec prism spectrophotometry.

Through the application of SED fitting techniques to high-redshift galaxies, we aim to refine our understanding of the early Universe. The ultimate goal of this research is to uncover potential correlations between the burstiness of star formation, the mass of galaxies, their dust extinction, and redshift. Identifying such relationships would not only enhance our comprehension of galactic evolution processes but also offer insights into the mechanisms driving star formation across cosmic time.

The thesis is structured as follows: Chapter 1 provides the cosmological framework for the formation of galaxies and describes the main astrophysical processes involving gas and dust in galaxies. Chapter 2 describes the evidence about high redshift galaxies by JWST and the main theories developed to explain the high number of bright galaxies observed at redshift $z > 10$. Chapter 3 describes JWST and its near-infrared spectrograph NIRSpec, together with a highlight about JADES 3rd ([D'Eugenio et al. 2024](#)) release that is the survey we used in this thesis. In Chapter 4 the analysis performed on the data is described, while Chapter 5 shows the results obtained. Chapter 6 summarizes the outcomes.

CHAPTER



Cosmology and galaxy formation

The evolution and properties of the very first galaxies are deeply connected with cosmology, which provides the framework within which these objects formed. This chapter outlines the cosmological context essential for studying these early galaxies.

Sec. 1.1 introduces the Lambda Cold Dark Matter (Λ CDM) model, the prevailing theoretical model in cosmology, which is the one adopted in this thesis. This is followed by Sec. 1.2 and Sec. 1.3, which review the principal concepts relating to the cosmological evolution of the Universe. Sec. 1.4 presents a brief history of the Universe, while Sec. 1.5 discusses the linearized theory of structures formation. Sec. 1.6 is dedicated to the nonlinear collapse of spherical halos and Sec. 1.7 derives the distribution of dark matter halos in the Universe following the Press-Schechter derivation. Finally, the last sections are dedicated to baryons: Sec. 1.8 describes the distribution of galaxies as a function of their stellar mass in the Universe, Sec. 1.9 shows the feedback mechanisms that act in galaxies and Sec. 1.10 describes the dust production and extinction.

1.1 The cosmological framework

In modern astrophysics, the most widely accepted cosmological model describing the evolution of the Universe is the Λ Cold Dark Matter (Λ CDM) (Blumenthal et al. 1984, Perivolaropoulos & Skara 2022).

A set of assumptions defines it:

- General relativity is the correct theory that describes gravity on cosmological scales.
- The cosmological principle holds, which says that the Universe is statistically homogeneous and isotropic at sufficiently large scales ($\gtrsim 100$ Mpc).
- The Universe consists of radiation (relativistic matter), ordinary matter (baryons

and leptons), cold dark matter, and a cosmological constant Λ . The dark matter is cold and collisionless. The cosmological constant is a homogeneous form of energy responsible for the present-time observed accelerated expansion of the Universe. The cosmological constant is currently associated with a dark energy whose density remains constant even in an expanding background.

- The spatial part of the cosmic metric is assumed to be flat.
- A primordial phase of rapid accelerated expansion named inflation is assumed.

In such a Universe the metric that describes this type of space-time is the Friedmann-Lemaître-Robertson-Walker (FLWR) metric:

$$ds^2 = -c^2 dt^2 + a^2(t) \left[\frac{dr^2}{1 - kr^2} + r^2(d\theta^2 + \sin^2 \theta d\varphi^2) \right] \quad (1.1)$$

where t is the cosmological proper time, (r, θ, φ) are the comoving spherical coordinates, $a(t)$ is a scale factor which only depend on time and k is the curvature that is null ($k = 0$) for a flat Universe as prescribed by the Λ CDM model. Following this prescription, a flat Universe is assumed in this thesis, unless where otherwise specified.

1.2 The Hubble parameter

1.2.1 Redshift and Hubble's law

The general arguments of the previous section do not indicate if the scale factor $a(t)$ in the FLWR metric is increasing, decreasing, or constant. It's important to note that $a(t)$ is the only free parameter in the metric, so to characterize it means to know everything about the history of the Universe from a cosmological standpoint.

The $a(t)$ evolution is set by the density ratio of the different components of the Universe, as shown in Sec. 1.3.1, but from an observational point of view the recent history of the scale factor comes to us from the observation of a shift in the frequencies of spectral lines from distant galaxies as compared with their values observed in terrestrial laboratories.

A ray of light obeys the equation $ds^2 = 0$ so from Eq. 1.1, if it was emitted at t_e and observed at t_o in a flat Universe, than:

$$r = c \int_{t_e}^{t_o} \frac{dt}{a(t)} \quad (1.2)$$

The next wavefront must satisfy:

$$r = c \int_{t_e + \lambda_e/c}^{t_o + \lambda_o/c} \frac{dt}{a(t)} \quad (1.3)$$

Assuming that the change in scale factor $a(t)$ is negligible in the time between two wave crests, then:

$$\frac{\lambda_e}{a(t_e)} = \frac{\lambda_o}{a(t_o)} \quad (1.4)$$

Introducing the redshift z defined as:

$$z := \frac{\lambda_o - \lambda_e}{\lambda_e} \quad (1.5)$$

It follows that, fixing $a(t_o) = 1$:

$$z = \frac{1}{a(t_e)} - 1 \quad (1.6)$$

We now can relate a measured quantity z to the scale factor $a(t_e)$. However, because the emission time t_e cannot be directly measured, we must go beyond this and try to relate the scale factor to a measurable quantity.

For nearby sources, we can expand in series $a(t)$

$$a(t) \approx a(t_o) + \dot{a}(t_o)(t - t_o) \quad (1.7)$$

Defining the Hubble parameter $H(t)$ as

$$H(t) := \frac{\dot{a}(t)}{a(t)} \quad (1.8)$$

Being $H_0 := H(t_o)$ the Hubble constant, putting again $a(t_o) = 1$ we get:

$$a(t) \approx 1 + H_0(t - t_0) \quad (1.9)$$

The proper distance¹ of an object in the FLWR metric is:

$$d_p(t) := \int a(t) dr = a(t)r \quad (1.10)$$

Recalling Eq. 1.6 and putting $d := d_p(t_o)$ we obtain:

$$z \approx \frac{H_0 d}{c} \quad (1.11)$$

This equation is known as Hubble's law. It is particularly relevant because, from measurements of distances and redshift, it is possible to infer a cosmological parameter (H_0). The delicate point is to measure distances accurately even far enough for the cosmological principle to hold.

This relationship played a crucial role in establishing the expanding nature of the Universe and has contributed significantly to our understanding of cosmology.

¹Distance measured at a fixed time. From the FLWR metric $dt = 0 \implies ds = a(t)dr$

1.2.2 Cosmological distances

When measuring the luminosities and angular sizes of objects in the Universe, it is important to consider the expansion of the Universe.

In cosmology, the common sense of distance is given by the proper distance $d_p(t)$. It is the spatial distance between two objects measured at a fixed time (Eq. 1.10). On cosmic scales, however, it is impossible to imagine making such a measurement and the proper distance is therefore never a direct measurement.

However, two other distances are defined in astrophysics.

The luminosity distance The luminosity distance d_L of an object is defined from:

$$F = \frac{L}{4\pi d_L^2} \quad (1.12)$$

where L is the luminosity of the source and F is the observed flux. Two effects make the luminosity distance different from the proper distance:

- Two photons emitted with a time difference δt_e will be observed with a time delay of $\delta t_o = \delta t_e(1 + z)$ (Eq. 1.2)
- The energy of each photon will be reduced by the cosmological redshift of another factor $1 + z$ (Eq. 1.4)

So that:

$$F = \frac{L}{4\pi r^2(1 + z)^2} \quad (1.13)$$

and finally:

$$d_L = r(1 + z) \quad (1.14)$$

The angular distance The angular distance d_A of an object is defined as²:

$$\delta\theta := \frac{l}{d_A} \quad (1.15)$$

where l is the component of the proper size of an object perpendicular to the line of sight and $\delta\theta$ is the subtended angle by the object in the sky. The distance l at t_e can be obtained from the FLWR metric setting $dr = dt = 0$:

$$l = a(t_e)r\delta\theta \quad (1.16)$$

Using Eq. 1.6, the angular distance can be expressed as:

$$d_A = \frac{r}{1 + z} \quad (1.17)$$

The comparison between the proper, the luminosity and the angular distances can be seen in Figure 1.1

²If $\delta\theta \ll 1$

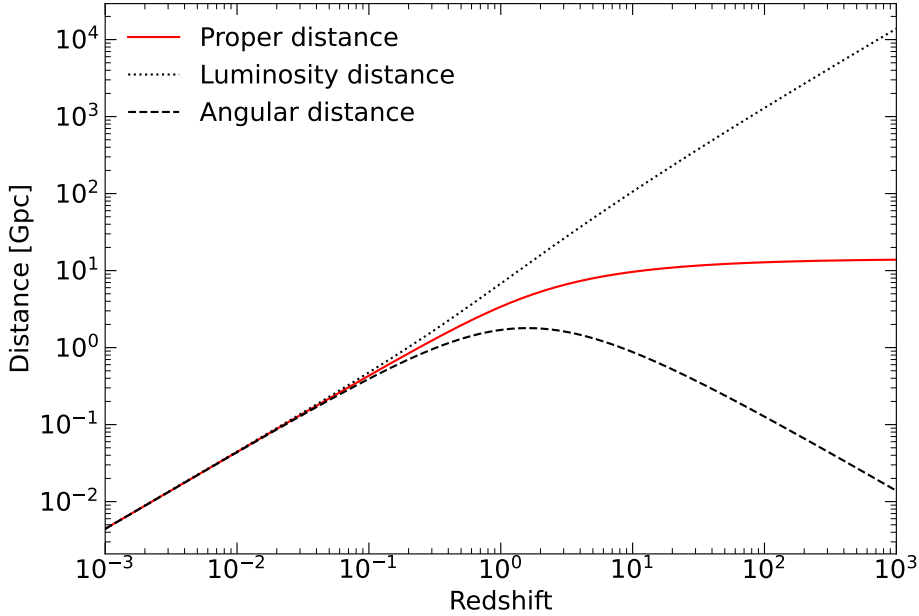


Figure 1.1: Proper, luminosity and angular distances as a function of redshift in a [Planck Collaboration et al. 2020a](#) cosmology

1.3 The evolution of the Universe

1.3.1 The Friedmann equations

The evolution of the scale parameter $a(t)$ in time is closely connected with the components of the Universe (matter, radiation and dark energy) and their energy.

To show this existing relationship we must recall the Einstein equation:

$$G_{\mu\nu} + \Lambda g_{\mu\nu} = \frac{8\pi G}{c^4} T_{\mu\nu} \quad (1.18)$$

where $G_{\mu\nu}$ is the Einstein tensor, Λ is the cosmological constant, $g_{\mu\nu}$ is the metric tensor, G is the gravitational constant and $T_{\mu\nu}$ is the stress-energy tensor.

For simplicity, from now on, we will incorporate the cosmological constant inside of the stress-energy tensor as a perfect fluid of energy density ρ_Λ and pressure $P_\Lambda = -\rho_\Lambda$.

If we consider the Universe permeated by a perfect fluid of energy density ρ and pressure³ P , then the stress-energy tensor has the form:

$$T_{\mu\nu} = (\rho + P)u_\mu u_\nu - g_{\mu\nu}P \quad (1.19)$$

The fluid must be at rest ($u_\nu = (\sqrt{g_{00}}, 0, 0, 0)$) to be consistent with the Universe's isotropy.

³That are global quantities thanks to homogeneity

Now, computing the Einstein tensor for a FLWR metric Eq. 1.1 and equating the terms:

$$G_{00} = \kappa T_{00} \quad (1.20)$$

$$G_{0i} = \kappa G_{i0} = 0 \quad (1.21)$$

$$G_{ij} = \kappa T_{ij} \quad (1.22)$$

with $\kappa = \frac{8\pi G}{c^4}$ we get two non-trivial equations⁴, which are known as Friedmann equations:

$$\begin{cases} H^2 + \frac{kc^2}{a^2} = \frac{8\pi G\rho}{3c^2} \\ \frac{\ddot{a}}{a} = -\frac{4\pi G}{3c^2}(\rho + 3P) \end{cases} \quad (1.23)$$

1.3.2 The cosmological parameters

To describe the total behavior of the Universe, the energy density can be expressed as the sum of different components:

$$\rho = \rho_{\text{mat}} + \rho_{\text{rad}} + \rho_{\Lambda} \quad (1.24)$$

where $\rho_{\Lambda} = \Lambda c^2 / 8\pi G$, while ρ_{mat} and ρ_{rad} are respectively the energy density of matter (ordinary matter and dark matter) and radiation (relativistic matter). The pressure of these components is different but easy to write down. If $P = w\rho$ than:

$$w = \begin{cases} 1/3 & \text{for relativistic matter} \\ 0 & \text{for nonrelativistic matter (Pressure is negligible)} \\ -1 & \text{for the cosmological constant} \end{cases} \quad (1.25)$$

The evolution of these densities with the scale factor can be obtained by exploiting the fact that the stress-energy tensor is the conserved Noether current associated with spacetime translations so that $D_\mu T^{\mu\nu} = 0$. This equation is automatically satisfied by the Friedmann equation, however, $D_\mu T^{\mu 0} = 0$ is the easiest way to compute $\rho(a)$. In fact, in a FLWR metric and with a perfect fluid, this equation reduces to:

$$\dot{\rho} + 3\frac{\dot{a}}{a}(P + \rho) = 0 \quad (1.26)$$

From which:

$$\rho \propto \begin{cases} a^{-4} & \text{if } w = 1/3 \\ a^{-3} & \text{if } w = 0 \\ \text{const} & \text{if } w = -1 \end{cases} \quad (1.27)$$

⁴here we are assuming a generalized Universe in which the curvature k does not have to be null

Relative densities The first Friedmann equation, Eq. 1.23, tells us that the curvature of space-time is directly set by the total density in the Universe. Moreover, a critical density ρ_c exists for which $k = 0$:

$$\rho_c(t) = \frac{3H^2(t)}{8\pi G} \quad (1.28)$$

Using the relative densities, which are defined as follows:

$$\Omega_i(t) = \rho_i/\rho_c \quad (1.29)$$

it is possible to express the Friedmann equations Eq. 1.23 as a single equation:

$$H^2(t) = H_0^2 \left(\Omega_{\text{rad},0}(1+z)^4 + \Omega_{\text{mat},0}(1+z)^3 + \Omega_{\Lambda,0} \right) \quad (1.30)$$

where the Universe is assumed to be flat $k = 0$, as prescribed by the Λ CDM paradigm. The subscript 0 means that these quantities are evaluated at present.

Measured cosmological parameters According to Planck Collaboration et al. 2020b the measured cosmological parameters are:

- $H_0 = (64.7 \pm 0.5) \text{ km s}^{-1}\text{Mpc}^{-1}$
- $\Omega_{\text{mat},0} = (0.315 \pm 0.007)$
- $\Omega_{\Lambda,0} = (0.6847 \pm 0.0073)$
- $\Omega_{k,0} < 0.005$

The baryonic relative density is:

- $\Omega_{\text{b},0} = (0.049 \pm 0.007)$

In the present epoch, the dominant energy source of the energy density of the Universe is the Cosmological Constant Λ , but it was not the same in the past. In fact Eq. 1.27 implies that there was a redshift ($z \approx 0.31$) at which matter and dark energy were energetically equivalent and another⁵ ($z \approx 3340$) when the radiation-matter equivalence held.

1.4 Key moments in the history of the Universe

In the previous sections, we have seen how the composition of the Universe changes over time. Now, to analyze the formation of the structures of our Universe, we highlight the moments in its history that were key points in the formation of what we observe today.

Big bang The observed composition of the Universe enables us to retrace its history. Tracing the evolution of the Universe backward in time, we find that the Friedmann equations (Eq. 1.23) predict a singularity in the past. This implies that the initial state of the Universe was a singularity with infinite energy, commonly referred to as the *Big bang*

⁵Using $T_{\text{CMB},0} \approx 2.726 \text{ K}$

The inflation Immediately after the Big Bang the Universe went through a period of exponential growth governed by dark energy that lasted only until 10^{-32} s. This era is particularly relevant to our current understanding of the Universe. Firstly, this is when the first density perturbations arise, which will later be the seeds for the formation of large-scale structures. This phase of the Universe also helps solve some problems in the Universe we observe: the flatness problem and the horizon problem. The first highlights how, without inflation, the fact that the curvature of our Universe is close to zero would be a large coincidence. Furthermore, without inflation, it would be difficult to explain the almost perfect homogeneity of regions of space that would never have been causally connected: this is the horizon problem.

Primordial nucleosynthesis The first nuclei began to form as soon as the Universe had cooled sufficiently to inhibit deuterium photodisintegration by high-energy photons. During this period, the Universe started the production of deuterium, then helium and traces of lithium and beryllium. When the temperature of the Universe dropped even more, the primordial nucleosynthesis stopped and the composition of the Universe remained unchanged until the formation of the first stars. This phase lasted for about 20 minutes.

The matter-radiation equivalence A turning point in the history of the Universe is the radiation-matter equivalence at redshift $z \approx 3340$. This is when the average energetic density of matter and radiation were the same. This is an important epoch because the behavior of the Universe when dominated by matter is different from that in the age dominated by radiation. The difference has an impact on how the primordial fluctuations grew as it is shown in Sec. 1.5.1.

The decoupling Another important epoch in the History of the Universe is the *decoupling time*. From the formation of the first particles, radiation and baryons in the Universe were deeply coupled. During the expansion, the average temperature dropped. When the temperature was of the order of $T \approx 3000$ K the plasma recombined and the first hydrogen atoms formed. At this time the Universe was practically homogeneous: assuming a strong radiation-matter coupling then the energy density is $\propto T^4$, so the typical relative fluctuations in density are about $\frac{\delta\rho}{\rho} \approx 4\frac{\delta T}{T} \sim 10^{-4}$. Soon after the recombination ($z \approx 1100$) the radiation and matter decoupled and the photons experienced a last scattering on matter. The cosmic microwave background (Figure 1.2) is the residual of this last scattering as observed nowadays. As we see in Sec. 1.5.1, the decoupling allowed the baryon overdensities to finally begin to collapse.

1.5 Linear structure growth

To obtain the Friedmann equations we assumed a homogeneous and isotropic Universe on a large scale.

However, the cosmological principle is no longer valid on smaller scales ($\lesssim 100$ Mpc). The generally accepted picture is that the Universe started from an extremely

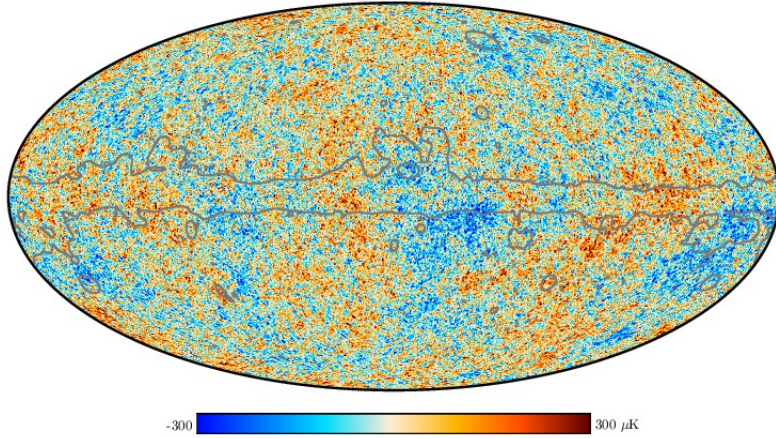


Figure 1.2: The anisotropies of the Cosmic microwave background (CMB) as observed by Planck. It shows temperature fluctuations that correspond to regions of slightly different densities ([Planck Collaboration et al. 2020a](#)). The region where residuals from foreground emission are expected to be substantial has gray contours.

homogeneous and isotropic state, with initial conditions provided by an era of accelerated expansion called inflation. The tiny primordial density fluctuations, generated during inflation from quantum fluctuations of the vacuum, would later grow under the influence of gravity and eventually collapse to form the structures we observe today, like galaxies, clusters and super-clusters.

In the next paragraphs, a view of how these small anisotropies grew over time will be shown.

1.5.1 Subhorizon linearized fluid equations

We need to solve the perturbed Friedmann equations to understand the evolution of the density fluctuations in the expanding Universe. However, when the scale of the perturbations is small compared to the horizon ($\ell \ll ct_0$) and the flow is non-relativistic ($v \ll c$), a Newtonian derivation can be used. Furthermore, when the perturbations are still small, as happens in the early stages of structure formation, the equations that govern their evolution can be linearized ([Silk et al. 2014](#)).

What we need is the mass-conservation equation, the Euler equation, the Poisson equation and an equation of state:

$$\begin{cases} \dot{\rho} + \nabla \cdot (\rho \mathbf{u}) = 0 \\ \frac{D\mathbf{u}}{Dt} = -\nabla\phi - \frac{1}{\rho}\nabla P \\ \nabla^2\phi = 4\pi G\rho \\ P = P(\rho) \end{cases} \quad (1.31)$$

where $\frac{D}{Dt}$ is the material derivative⁶ and ϕ is the gravitational potential.

⁶ $\frac{D}{Dt} = \frac{\partial}{\partial t} + \mathbf{v} \cdot \nabla$

We now want to perturb the solution for a homogeneous fluid. For this purpose, we introduce the overdensity δ defined as:

$$\delta(\mathbf{x}, t) := \frac{\rho(\mathbf{x}, t)}{\bar{\rho}} - 1 \quad (1.32)$$

where $\bar{\rho}$ is the average energy density used in the Friedmann equations. Using $\rho = \bar{\rho}(1 + \delta)$ and $\mathbf{v} = \mathbf{u} - H\mathbf{r}$, for an adiabatic evolution the lead term must follow:

$$\ddot{\delta} + 2H\dot{\delta} = 4\pi G\bar{\rho}\delta + c_s^2\nabla^2\delta \quad (1.33)$$

where the second term on the left is the cosmological damping due to the expansion of the Universe, while the second term on the right is the pressure term.

Now, it is necessary to distinguish the different behavior of baryonic matter and dark matter. The dark matter does not interact with photons and by Λ CDM prescription we can completely neglect the pressure term. On the other hand, baryonic matter has a negligible pressure nowadays but when it was still coupled with radiation, the pressure was relevant.

The dark matter perturbations in this way, can grow earlier than the matter ones, becoming gravitational wells for baryons, and promoting their collapse afterward.

Dark Matter For dark matter, we can write:

$$\ddot{\delta}_m + 2H\dot{\delta}_m = 4\pi G\bar{\rho}_m\delta_m \quad (1.34)$$

here $_m$ is used for dark matter quantities. Using Eq. 1.28 we can rewrite the equation as:

$$\frac{\ddot{\delta}_m}{H^2} + 2\frac{\dot{\delta}_m}{H} = \frac{3\bar{\rho}_m\delta_m}{2\bar{\rho}} \quad (1.35)$$

and because deep in the radiation-dominated era $\bar{\rho} \sim \rho_r \gg \rho_m$, while in the matter-dominated era $\bar{\rho} \sim \rho_m$ we obtain two classes of solutions:

$$\delta_m(t) = \begin{cases} B_1 + B_2 \ln t & \text{in radiation-dominated era} \\ A a(t) & \text{in matter-dominated era} \end{cases} \quad (1.36)$$

So, dark matter overdensities could have grown linearly in a only from the matter-radiation energetic equivalence ($z \approx 3340$)

Baryonic Matter Before decoupling, photons and baryons were coupled. Moreover, in terms of energy density, radiation dominates over baryons. Therefore:

$$c_s = c \sqrt{\frac{\partial P}{\partial \rho}} \approx c \sqrt{\left. \frac{\partial P}{\partial \rho} \right|_{\text{rad}}} = \sqrt{\frac{1}{3}}c \quad (1.37)$$

Recalling Eq. 1.33 and using the Fourier space to look for the solutions, it immediately follows that only structures larger than the Jeans radius R_J can grow:

$$R_J = \sqrt{\frac{\pi}{3G\rho_0}}c \quad (1.38)$$

which at the decoupling epoch was a radius containing $\sim 10^{20} M_\odot$ orders of magnitude larger than the size of a supercluster of galaxies. So, the baryons could have started to collapse in the dark matter potential wells only after the decoupling era.

1.5.2 Superhorizon growth

Even if the Newtonian derivation says that dark matter structures began to grow in the matter-dominated era, there is a case in which a fluctuation can start to collapse even in the radiation-dominated phase. In fact, it can be shown (Mo et al. 2010) that during the radiation era structures larger than the horizon⁷ could collapse:

$$\delta_m(t) = \begin{cases} B_1 + B_2 \ln t & \text{subhorizon scales} \\ At & \text{superhorizon scales} \end{cases} \quad (1.39)$$

the subhorizon solution was already described in Eq. 1.36. Because in the radiation-dominated era $a \sim t^{1/2}$, as it can be derived from Eq. 1.23, while the horizon grows linearly in time than it exists an instant t^* in which a superhorizon perturbation becomes subhorizon (Meszaros 1975). There are two possibilities:

- If t^* happens after the matter-radiation equality t_{eq} the perturbation grow as t in the radiation era and as⁸ $t^{2/3}$ in the matter phase, independently if before or after t^*
- If t^* is reached in the radiation era, then the perturbation stops growing until t_{eq}

This well explain the observed power spectrum $P(k)$ of the structures in the Universe defined from⁹

$$\langle \delta^2 \rangle = \frac{1}{2\pi^2} \int dk k^2 P(k) \quad (1.40)$$

Yet, to understand the shape of the power spectrum we must briefly talk about how the fluctuations are thought to have arisen. In the inflationary paradigm, it is believed that quantum mechanical fluctuations in the very early Universe were stretched to macroscopic scales by the large expansion factor the Universe underwent during inflation. Since this type of fluctuation is random, the primordial density perturbations should be well described as a Gaussian random field.

⁷The particle horizon is the maximum distance from which light from particles could have traveled to the observer in the age of the Universe. Its value at an instant t is $d_H(t) = c \int_0^t \frac{dt'}{a(t')}$

⁸Linearly with a which means $\sim t^{2/3}$ in the matter era

⁹Here $\langle \delta^2 \rangle$ represent the autocorrelation function between any point and itself

The primordial power spectrum is parameterized as a power law $P_{HZ}(k) \propto k^n$, with $n = 1$ corresponding to scale-invariant spectrum proposed by Harrison and Zeldovich (Harrison 1970; Zeldovich 1972).

Calling k_{eq} the wave vector at which the perturbation of this size becomes subhorizon at the radiation-matter equality, then the observed power spectrum is the original inflation power spectrum only for $k \ll k_{eq}$.

If $k \gg k_{eq}$ the power spectrum observed after the decoupling will be different from the original one: the fluctuations are not-growing from t^* to t_{eq} , so respect to the always-growing overdensities¹⁰:

$$\frac{\delta_{k \gg k_{eq}}(t_{eq})}{\delta_{k \ll k_{eq}}(t_{eq})} = \frac{a^2(t^*(k))}{a^2(t_{eq})} \frac{\delta_{k \gg k_{eq}}(t_i)}{\delta_{k \ll k_{eq}}(t_i)} \quad (1.41)$$

where t_i is the time at the end of the inflation when the Harrison-Zeldovich power spectrum still holds.

If we now consider that the Horizon grows linearly with t while structures grow linearly with $a \sim t^{1/2}$ in the radiation-dominated phase, then $a(t^*) \sim \frac{1}{k}$. So, the power spectrum observed after the decoupling will be

$$P(k) = P_{HZ}(k) |T^2(k)| \quad (1.42)$$

where $T(k)$ is called transfer function. Using Eq. 1.41 and Eq. 1.40:

$$|T^2(k)| \propto \begin{cases} 1 & \text{if } k \ll k_{eq} \\ k^{-4} & \text{if } k \gg k_{eq} \end{cases} \quad (1.43)$$

which means that:

$$P(k) \propto \begin{cases} k & \text{if } k \ll k_{eq} \\ k^{-3} & \text{if } k \gg k_{eq} \end{cases} \quad (1.44)$$

1.6 Nonlinear structure growth

In Sec. 1.5 we have investigated the linear structure formation theory. However, the linear approximation of the perturbation theory can hold only if the perturbations are small ($\delta \ll 1$). Perturbations depart from the linear regime as they grow. The full description of the non-linear regime can only be numerically treated. A simplified model is considered here: the isolated spherical collapse (Dodelson 2021).

Let us consider a spherically symmetric density fluctuation. To describe the evolution of the overdensity over time we must use the Friedmann equation (Eq. 1.23). Noting that the dark matter density of the overdensity is

$$\rho(t) = \frac{M}{4\pi r(t)^3/3} \quad (1.45)$$

¹⁰In the radiation era a function linear in t is quadratic in a

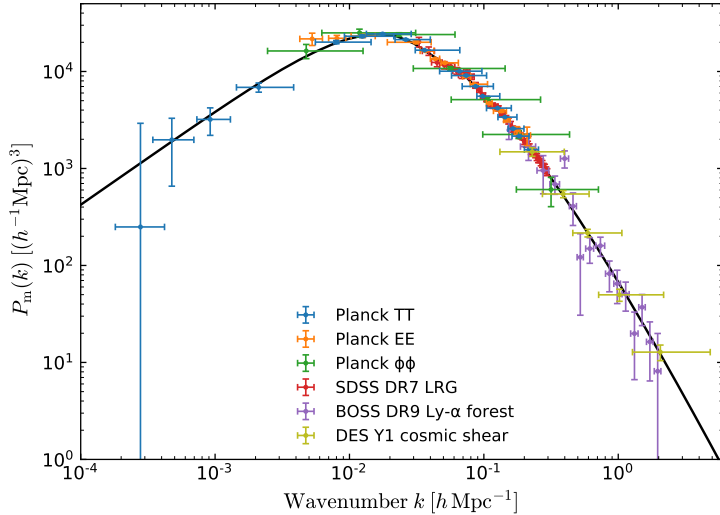


Figure 1.3: (Konrad & Bartelmann 2022) Linearly evolved, density-fluctuation power spectrum reconstructed from different classes of cosmological measurement. The line is the Λ CDM power spectrum. On the x -axis $h := \frac{H_0}{100 \text{ km s}^{-1} \text{ Mpc}}$

where M is the overdensity's mass and $r(t)$ its size, and that the only pressure term is the one from the cosmological constant for which $P_\Lambda = -\rho_\Lambda$ (Eq. 1.25), then the second Friedmann equation for the spherical overdensity can be written as:

$$\frac{\ddot{r}}{r} = -\frac{4\pi G}{3} \left[\frac{M}{4\pi r^3/3} - 2\rho_\Lambda \right] \quad (1.46)$$

Supposing the radius of the overdensity is small enough so that the dark energy term is negligible, then the Friedmann equation becomes equivalent to the Newtonian law:

$$\ddot{r} = -\frac{GM}{r^2} \quad (1.47)$$

Considering perturbations that are collapsing, the solution of this equation can be written parametrically:

$$r = \frac{r_{\text{ta}}}{2} (1 - \cos \theta) \quad (1.48)$$

$$t = \sqrt{\frac{r_{\text{ta}}}{8GM}} (\theta - \sin \theta) \quad (1.49)$$

where θ is the parameter, which is null for $t = 0$ and increases with time. r_{ta} is the radius the overdensity when $\theta = \pi$, which is called the turnaround point. Figure 1.4 depicts the evolution in time of the radius of the overdensity, comparing the prediction of the linear and non-linear theories. The expansion halts and the radius starts to decrease at the turnaround point. The collapse ends at $t = 2t_{\text{ta}}$.

The overdensity over time of the spherical region is:

$$\delta(t) = \frac{\rho_t(t)}{\rho_m(t)} - 1 \quad (1.50)$$

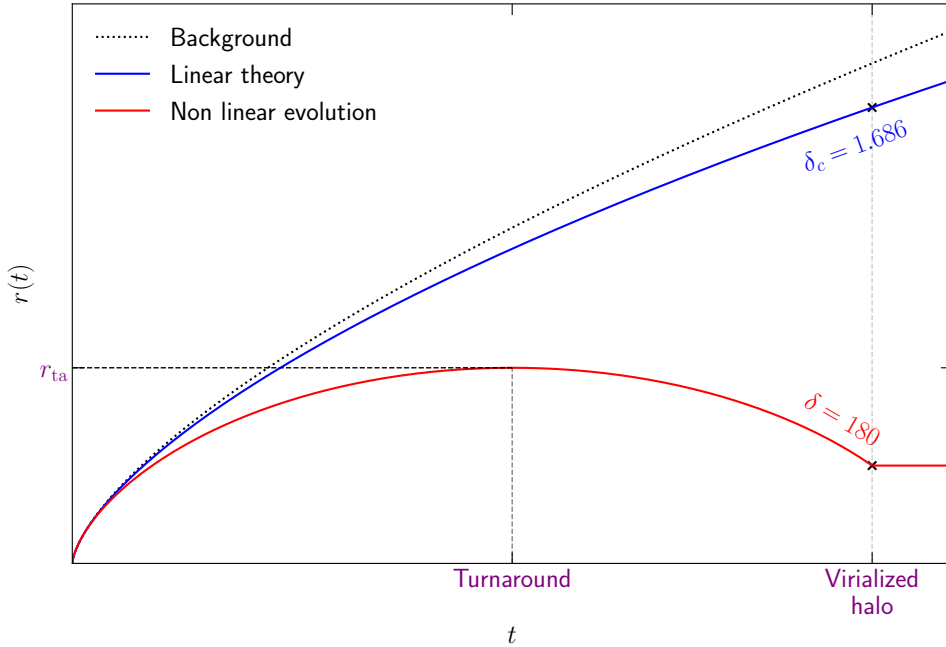


Figure 1.4: The evolution over time of the radius of a spherical overdensity, comparing the linear and non-linear theory. In the non-linear evolution, the overdense fluctuation reaches the maximum radius at the turnaround point. Then the overdensity starts to compress itself forming a fully-collapsed virialized ‘halo’ with a density 180 times greater than the background. In the linear evolution, the overdensity slowly grows over time. The halo is formed when in the linear theory the overdensity reaches the critical overdensity $\delta_c = 1.686$

where $\rho_t(t)$ is the density of the overdense region while $\rho_m(t)$ is the average density of the Universe. In a matter-dominated Universe $\rho(t) \propto a^{-3}$, using Eq. 1.23 it follows that $\rho(t) \propto t^{-2}$. So, using that

$$\lim_{\theta \rightarrow 0} \delta(t) = 0 \quad (1.51)$$

in the Eq. 1.50 to set the constants, than from Eq. 1.48 and Eq. 1.49:

$$\delta(t) = \frac{9}{2} \frac{(\theta - \sin \theta)^2}{(1 - \cos \theta)^3} - 1 \quad (1.52)$$

The theory just shown predicts that the fluctuation became a singularity at the time when $\theta = 2\pi$. However, here we are neglecting the violent relaxation¹¹ that ‘virialize’ the collapsing dark matter into an equilibrium configuration called ‘halo’ where the virial theorem holds. The theorem says that the average total kinetic energy $\langle T \rangle$ and the average total potential energy $\langle U \rangle$ must satisfy:

$$2 \langle T \rangle + \langle U \rangle = 0 \quad (1.53)$$

We can approximate the time of virialization as the time at which our model collapses into a singular density. Once the halo has virialized we can estimate its

¹¹Violent relaxation refers to the rapid evolution of a gravitational system that begins in a state far from equilibrium. During this process, the kinematics of individual particles change dramatically due to the rapidly evolving gravitational potential of the system.

radius. Assuming a homogeneous fluctuation at the turnaround, the total energy E of the matter inside the collapsing sphere is:

$$E = U_{\text{ta}} = -\frac{3}{5} \frac{GM^2}{r_{\text{ta}}} \quad (1.54)$$

where U_{ta} is the potential energy of the sphere at the turnaround point. Here, we are assuming that the kinetic energy at the turnaround point is null, hence all dark matter in the sphere reaches the turnaround point at the same instant.

When the virialization is completed the potential energy of the halo is $U_{\text{vir}} = \frac{1}{2}E = \frac{1}{2}U_{\text{ta}}$ from which the halo radius is:

$$r_{\text{vir}} = \frac{1}{2}r_{\text{ta}} \implies \theta = \frac{3}{2}\pi \quad (1.55)$$

Using Eq. 1.52 the overdensity of the virialized halo is $\delta_{\text{vir}} = 145$. $\delta_{\text{vir}} = 180$ is the value generally adopted [Dodelson 2021](#). A region with a density that is a few hundred times greater than the background density should form a halo.

If we only used the linear theory at the collapse time $\delta(2t_{TA}) := \delta_c \approx 1.686$. So it's widely used that a collapsed object can be found using only the linearized arguments of the previous section and looking for regions where $\delta \geq \delta_c$, where δ_c is called critical density.

1.7 Press-Schechter theory

One of the most fundamental predictions of hierarchical structure formation is the mass function: the density of objects as a function of their mass. A complete treatment of the problem can only be solved numerically. Here it is presented the Press-Schechter ([Press & Schechter 1974](#)) model which provides a relatively good fit to the results of numerical simulations. Although we know that some of the assumptions of these models are wrong, the result is surprisingly accurate and is presented here.

Some topics must be presented before the discussion of the theory itself.

Smoothing and mass fluctuations We can define a R-averaged (radius-averaged) overdensity function $\delta(\mathbf{x}, R)$ as:

$$\delta(\mathbf{x}, R) = \int d^3\mathbf{x}' \delta(\mathbf{x}') W(\mathbf{x}' - \mathbf{x}; R) \quad (1.56)$$

where $W(\mathbf{d}, R)$ is a proper window function of size R . In the original article, a box-like function uniform for $|\mathbf{x}' - \mathbf{x}| < R$ and null outside has been used.

Similarly to Eq. 1.40 an R-dependent variance can be defined as:

$$\sigma^2(R) = \langle \delta^2(\mathbf{x}, R) \rangle = \frac{1}{2\pi^2} \int dk k^2 P(k) \tilde{W}^2(k; R) \quad (1.57)$$

where $\tilde{W}(k; R)$ is the fourier transform of $W(\mathbf{x}; R)$ in which we made explicit that it depends only on $k = |\mathbf{k}|$

We want now to express these quantities in terms of the mass $M(\mathbf{x}; R) = \int d^3\mathbf{x}' \rho(\mathbf{x}') W(\mathbf{x}' - \mathbf{x}; R)$. If $\hat{M}(R) = \langle M(\mathbf{x}; R) \rangle$, than:

$$\sigma_M := \sigma^2(M) = \left\langle \left(\frac{M(\mathbf{x}; R) - \hat{M}(R)}{\hat{M}(R)} \right)^2 \right\rangle \quad (1.58)$$

If $\delta(\mathbf{x})$ is a gaussian random field, than so $\delta(\mathbf{x}, M)$ is.

Linear growth Fixing $\delta_0(\mathbf{x}) := \delta(\mathbf{x}, t_0)$ the overdensities at a starting point t_0 (which can be for example the matter-radiation equality time t_{eq}), from linear theory it is possible to extrapolate this value forward in time:

$$\delta(\mathbf{x}, t) = D(t)\delta_0(\mathbf{x}) \quad (1.59)$$

where $D(t)$ is the function that includes how structures grow in linear theory.

Using the spherical collapse model, we'll consider collapsed at time t the zones for which:

$$\delta_0(\mathbf{x}) \geq \frac{\delta_c}{D(t)} := \delta_c(t) \quad (1.60)$$

A one-dimensional example is shown in Figure 1.5

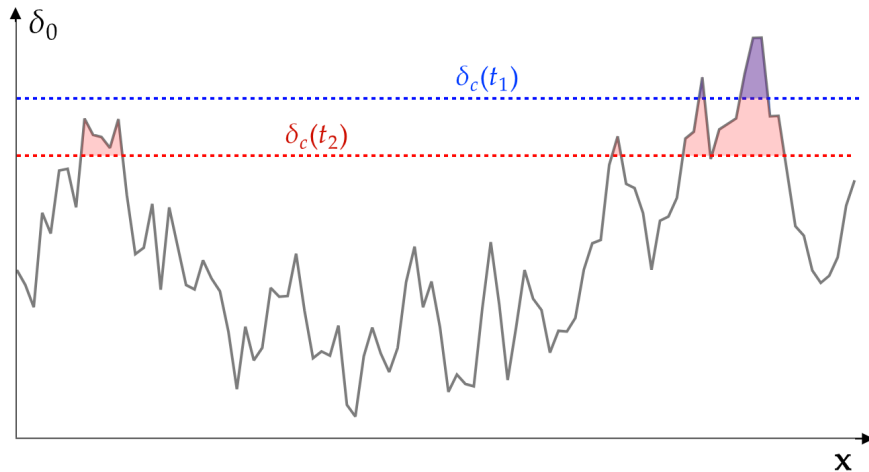


Figure 1.5: In the Press-Schechter view, overdensities (black line) are considered frozen at time t_0 and the effective critical overdensity $\delta_c(t)$ (blue and red dashed lines) diminish over time. At the time t_1 only the blue-colored regions are collapsed, at t_2 the red regions (which contain the blue ones) are collapsed

The Press-Schechter postulate At this point, it could seem clear that the number density of peaks of δ_M may well represent the number density of haloes with mass M in the Universe.

However, there arises the problem that in some conditions for a fixed position \mathbf{x}_p we have that $\delta_{M_1}(\mathbf{x}_p) < \delta_{M_2}(\mathbf{x}_p)$ for $M_1 < M_2$ which means that the halo of mass M_1 would not form because it is already collapsed in a larger mass halo. If $M_1 > M_2$ then there would not be any problem: the smaller halo, already collapsed, will converge in a larger newly collapsed halo (which is the basis of the *bottom-up* formation of structures).

To overcome this problem Press and Schechter used the following postulate:

“The probability that $\delta_M > \delta_c(t)$ is the same as the mass fraction that at time t is contained in haloes with mass greater than M ”

which means that if $\delta_M > \delta_c(t)$ a halo with mass at least M exists.

For a Gaussian random field, we can directly write the probability

$$\mathcal{P}(\delta_M > \delta_c(t)) = \frac{1}{\sqrt{2\pi}\sigma_M} \int_{\delta_c(t)}^{\infty} d\delta_M e^{-\frac{\delta_M^2}{2\sigma_M^2}} = \frac{1}{2} \operatorname{erfc}\left(\frac{\delta_c(t)}{\sqrt{2}\sigma_M}\right) \quad (1.61)$$

where $\operatorname{erfc}(x) = 1 - \operatorname{erf}(x)$

Using the Press-Schechter postulate we get the mass-fraction F of the haloes more massive than M :

$$F(>M, t) = \frac{1}{2} \operatorname{erfc}\left(\frac{\delta_c(t)}{\sqrt{2}\sigma_M}\right) \quad (1.62)$$

We immediately see that $\lim_{M \rightarrow 0} F(>M, t) = \frac{1}{2} \neq 1$. The authors corrected *ad hoc* this problem by multiplying by 2. Then, it is possible to obtain the Press-Schechter mass function $n(M, t)$. In fact:

$$n(M, t) = \frac{\bar{\rho}}{M} \frac{\partial F(>M, t)}{\partial M} \quad (1.63)$$

where $\bar{\rho}$ is the average density of the Universe¹². So:

$$n(M, t) = \sqrt{\frac{2}{\pi}} \frac{\bar{\rho}}{M^2} \frac{\delta_c(t)}{\sigma_M} \exp\left(-\frac{\delta_c^2(t)}{2\sigma_M^2}\right) \left| \frac{d \ln \sigma_M}{d \ln M} \right| \quad (1.64)$$

If we put in a power spectrum of the form $P(k) = k^n$, using Eq. 1.57 we get:

$$\sigma_M \propto M^{-\frac{n+3}{6}} \quad (1.65)$$

which can be used to derive:

$$n(M, t) = \frac{1}{\sqrt{\pi}} \left(1 + \frac{n}{3}\right) \frac{\bar{\rho}}{M^2} \left(\frac{M}{M_*}\right)^{(n+3)/6} \exp\left(-\left(\frac{M}{M_*}\right)^{(n+3)/3}\right) \quad (1.66)$$

¹²In comoving distances is a constant quantity. If used in this way the halo mass function will be a numeric density in comoving coordinates

where M_* is a parameter which depends on time because it includes $\delta_c(t)$. If we go into detail, comparing Eq. 1.64 and Eq. 1.66, because $\delta_c(t)$ is a monotonically decreasing function of time, then M_* have to be monotonically increasing. This is the base of the *bottom-up* paradigm which says that smaller structures are formed earlier and then converge in greater structures.

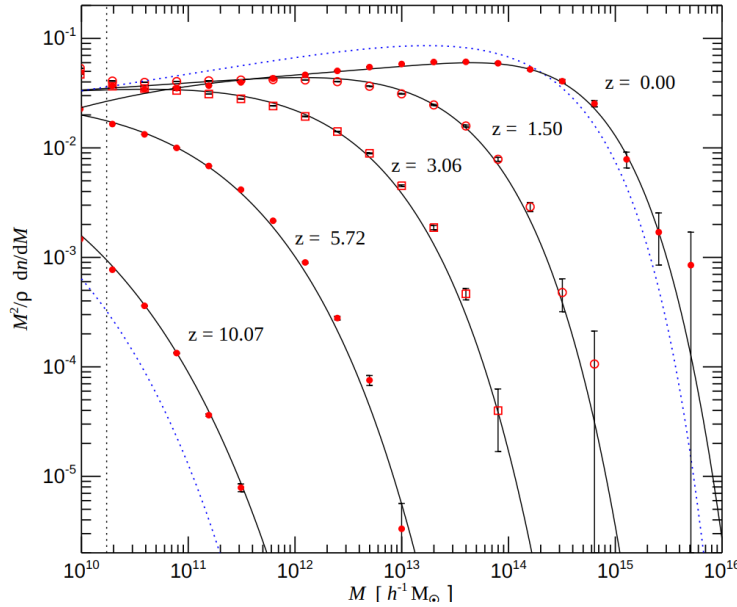


Figure 1.6: (Springel et al. 2005) Comparison between the GADGET2 simulation (red points) the Press-Schechter halo mass function (dotted lines) and Sheth & Tormen 1999 halo mass function (solid lines)

Among the various articles that subsequently looked for a solution to the less clear points of Press and Schechter's proof, the following two are worth mentioning: Bond et al. 1991 which formalized what is called the 'Extended Press-Schechter theory' and Sheth & Tormen 1999 which considered the possible ellipticity of the proto dark matter haloes.

1.8 The stellar mass function

While the prediction about the dark matter halo distribution is robust, our direct observations are limited to baryons. This is true although the baryonic component of the Universe is secondary in terms of mass, indeed, the baryonic fraction of the matter in the Universe is, according to Planck Collaboration et al. 2020b

$$f_b = \frac{\Omega_{b,0}}{\Omega_{\text{mat},0}} = (0.156 \pm 0.003) \quad (1.67)$$

Our limitation to detect the dark matter makes it crucial to study the baryonic counterpart of the halo mass function: the 'stellar mass function' which is the density of galaxies as a function of their stellar mass. Assuming we divide the stellar masses of galaxies into small intervals, the stellar mass function would be described as the number of galaxies that exist in each stellar mass interval. If the efficiency of

converting baryons into stars were 100% then the stellar mass M_\star in a galaxy would be, on average, directly related to the halo mass M_H by

$$M_\star = f_b M_H \quad (1.68)$$

If this relationship were true, the stellar mass function would have the same shape as the halo mass function but shifted to lower masses. However, this is not what is observed: the stellar mass function is always lower than the one expected if Eq. 1.68 held and the shape is different: the efficiency of converting baryons into stars is lower at low and high masses with a peak at $\approx 10^{11} M_\odot$ (for $z = 0$ galaxies). In Figure 1.7 is shown the behavior just described for local galaxies. The discrepancy observed can

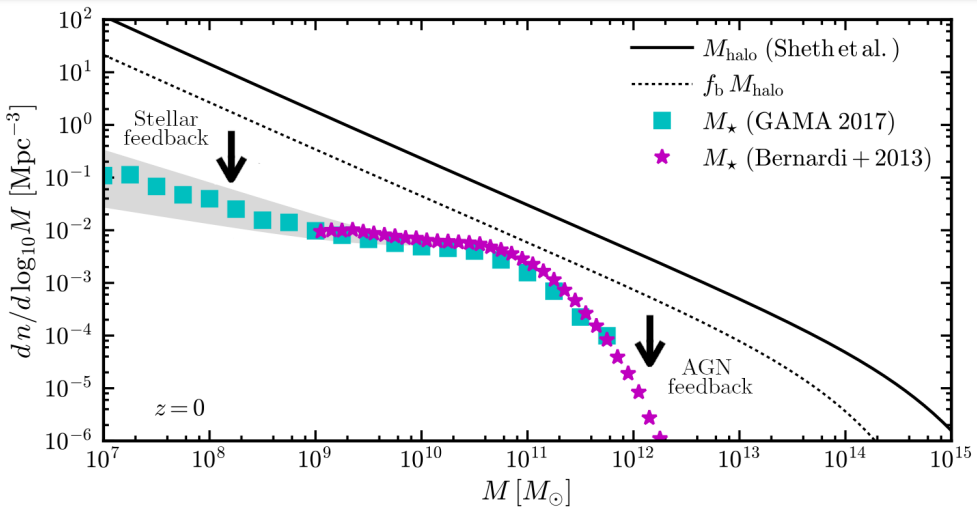


Figure 1.7: The number density of objects is shown as a function of their mass for local galaxies ($z = 0$). The colored points are galaxies. The solid line is the predicted number of dark matter halos. The dotted line is what one would expect for galaxies if all the normal matter associated with each dark matter halo turned into stars. Data from [Bernardi et al. 2013](#) and [Wright et al. 2017](#). Credits: [Bullock & Boylan-Kolchin 2017](#)

be explained by some mechanism that inhibits the conversion of gas into stars.

To form stars a cloud of gas must cool down. The cooling is crucial to allow a thermally-supported cloud to become cold enough to collapse under its gravitational potential. If no heating sources were present the baryons in the halo of mass lower than $10^{12} M_\odot$ would have enough time to cool down from the halo virialization to the present day and so the baryonic mass would be almost entirely converted into stars (this is known in the literature as the ‘overcooling problem’). However, if there are heating sources the baryonic gas may never become enough dense and cold to form stars.

The stellar feedback is the process by which stars influence the gas of the interstellar medium around themselves. This interaction happens through the release of energy and matter from the star through radiation pressure, stellar winds, or supernova explosions. The result of the stellar feedback is heating and injecting turbulence into the surrounding gas. The injection process is the one that regulates star formation. In galaxies exists another form of feedback: the Active Galactic Nucleus (AGN)

feedback. Analogously to its stellar counterpart just described, AGNs which are accreting supermassive black holes, inject energy and turbulence in the galaxy’s gas thanks to AGN’s winds, outflows and radiation. A deeper look at the feedback processes is presented in Sec. 1.9.

For now, we just say that, regarding the stellar mass function, the low-mass halos discrepancy can be explained by a combination of stellar wind and supernovae feedback. For the high-mass side difference, where more energy is necessary to impact the star formation efficiency of the galaxy, a viable candidate is Active Galactic Nucleus (AGN) feedback (Davé et al. 2016, Kim et al. 2013, Harrison et al. 2018, Mutch et al. 2013, Efstathiou 2000).

The measure of the stellar to halo mass ratio (SHMR: M_\star/M_H) as a function of the halo mass provides information about the star formation efficiency in galaxies (Figure 1.8). Indeed, the average star formation efficiency ϵ_\star in galaxies can be computed as:

$$\epsilon_\star = \frac{M_\star}{f_b M_H} \quad (1.69)$$

If the SHMR is measured over redshift, it is possible to model how the star formation efficiency varies over time and, in principle, extrapolate the expected stellar mass function at higher redshift. This concept will be key to understanding why the observation of high redshift galaxies ($z \gtrsim 10$) with JWST is puzzling astrophysicists around the world. The observation of these primordial galaxies will be presented in Chapter 2.

1.9 Stellar feedback

We have discussed in Sec. 1.8 how the feedback processes are crucial to explain the low star formation efficiency in galaxies. Without any feedback to suppress the gas cooling and consequently the star formation, most of the cosmic gas has to have cooled and formed stars by the present day. This problem known as the ‘overcooling problem’ was recognized since the first galactic evolution models. Feedback processes can both heat the gas and drive large-scale winds, blowing away a relevant fraction of the interstellar gas in the galaxy.

A galaxy is an open system with many interacting components: the processes that occur in a galaxy (e.g. star formation, supernova explosion, supermassive black holes accretion, gas radiative cooling) are strictly interconnected. The feedback is the way a process can inhibit (negative feedback) or boost (positive feedback) itself by interacting with the components of the galaxy. For example, an increased cooling of hot gas results in more cold gas, which subsequently boosts the star formation rate and, consequently, the rate of supernovae. The additional energy from supernovae can reheat the cold gas, thereby reducing further star formation (negative feedback). Conversely, supernova blast waves can also compress the surrounding cold gas, locally enhancing the star formation rate (positive feedback).

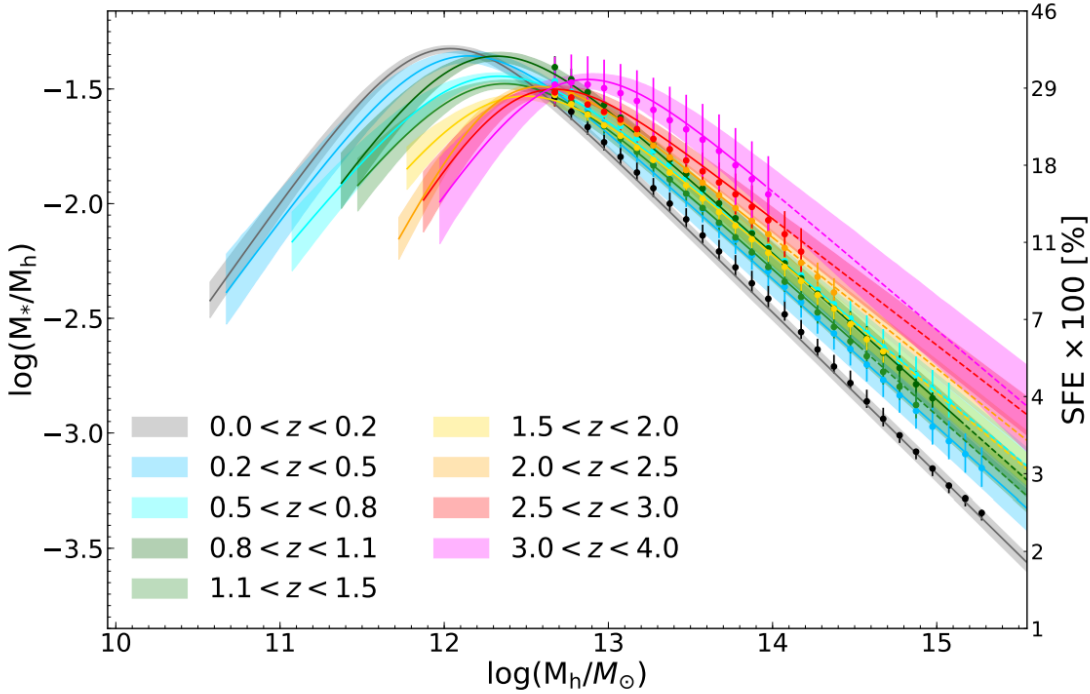


Figure 1.8: The stellar to halo mass ratio as a function of the halo mass. In this graph halo masses from the Λ CDM DUSTGRAIN-pathfinder simulation are plotted with observation of stellar mass data on the COSMOS field. The stellar-to-halo mass ratio is also a measure of the star formation efficiency, which is plotted on the secondary y -axis. Credits:[Girelli et al. 2020](#)

The most important physical processes related to star formation feedback and galaxy evolution are:

- **Stellar radiation** During their life cycle, stars emit up to $\sim 10^{53}$ erg of radiation. The impact of the stellar radiation on the interstellar medium is related to the UV photoheating and the production of HII regions¹³. Radiation feedback by UV photons emitted by OB stars plays an important role in regulating star formation in clouds. These photons heat the gas in clouds to around 10^4 K, preventing further star formation and driving thermal shocks that expel gas from the clouds ([Strömgren 1939](#), [Geen et al. 2015](#)).
- **Stellar winds**: Some massive stars can lose substantial amounts of mass via stellar winds during their late evolutionary stages. The expelled mass rate increases with mass and stellar radius ([Waldron 1984](#)). OB stars¹⁴ produce winds with a typical velocity of around 2000 km/s. The energy ejected is continuous and for OB stars is comparable to the kinetic energy output from a supernova for populations with solar metallicities([Mo et al. 2010](#)). The relative importance of stellar winds to supernovae explosion decreases with decreasing metallicities ([Leitherer et al. 1999](#)). Low mass stars mainly lose mass through

¹³HII regions are zones of ionized hydrogen gas found around young, hot stars. These regions are created when ultraviolet light from the stars ionizes the surrounding hydrogen gas. HII regions are sites of active star formation and are characterized by their bright emission line

¹⁴Massive stars with a surface temperature during the main sequence phase greater than 10^4 K

the stellar winds in their AGB phase¹⁵

- **Supernova explosions** Type-II supernovae (SNe), the core-collapse supernova explosions that mark the end of massive stars, eject roughly 10^{51} erg of energy. The ejected mass can change substantially from object to object, as their progenitors can cover a large mass range and the remnant mass depends on the details of the properties of the progenitor. Type Ia SNe¹⁶ roughly have the same luminosity but the mass ejected is always near the Chandrasekhar limit ($1.4 M_{\odot}$). Type Ia SNe occur on average at later times: indeed, they can happen only after white dwarfs are born. On average SNIa produce feedback with a time delay $t_{SNIa} \sim 1$ Gyr (Heringer et al. 2017). For this reason, SNIa feedback is negligible for galaxies at redshift $z > 6$ where the star formation history cannot be longer¹⁷ than 800 Myr.

The relative importance of stellar winds and supernova explosions depends on the metallicity of the stars. The feedback energy injection as a function of time produced by a simple stellar population is shown in Figure 1.9. Stellar winds are less important in a low metallicity environment. Type II supernovae explosions inject feedback with a time delay of about $t_{SNe} \approx 3$ Myr relative to the star formation time.

1.10 Dust

We have seen that stellar winds and supernova explosions not only inject energy and momentum into the interstellar medium but also pollute the galactic gas with stellar mass lost during these evolutionary phases. When metals ejected¹⁸ from stars cool down, become ‘dust’. Dust consists of tiny solid particles, typically composed of elements like carbon, silicon, oxygen, and iron. Dust plays a crucial role in galaxy dynamics by absorbing and scattering light, affecting the thermal balance of the interstellar medium, and serving as a catalyst for the formation of molecular hydrogen, which is essential for star formation.

The cross-section of the extinction by dust is:

$$\sigma_{ext}(\lambda) = S Q_{ext}(\lambda) \quad (1.70)$$

where S is the surface of the grain exposed to light and $Q_{ext}(\lambda)$ is the extinction efficiency, which is the sum of the absorption and scattering efficiency. Supposing the grain to have a characteristic size a ¹⁹, $Q_{ext}(\lambda)$ tends to 0 for $a \ll \lambda$ and to 2 in the limit $a \gg \lambda$. The dust is formed by a mixture of grains of different sizes. The dust produced in galaxies reduces the observed luminosity from the galaxies

¹⁵AGB: The asymptotic giant branch is the phase in which the helium fusion in the core of the star is completed and the star proceeds with fusing helium in a shell (Early-AGB) or hydrogen and helium in a shell (thermally pulsing AGB)

¹⁶Type Ia supernovae occur in binary star systems where one of the stars is a white dwarf. These supernovae happen when the white dwarf accretes enough matter from its companion star, reaching the Chandrasekhar mass limit and undergoing a runaway nuclear reaction

¹⁷Considering the first stars forming at redshift $z = 20$

¹⁸In astronomy metals are the elements heavier than helium

¹⁹ $a \sim \sqrt{S}$

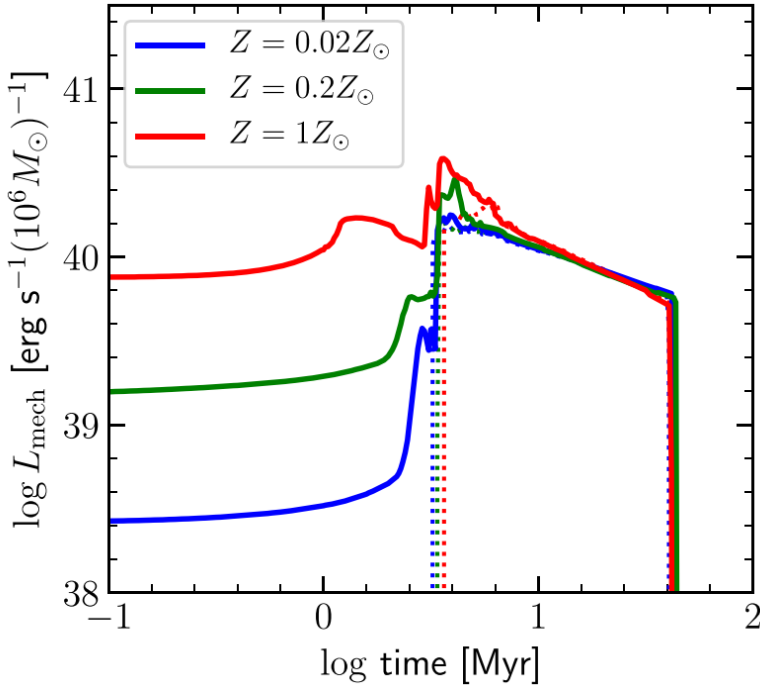


Figure 1.9: Feedback energy injection rate as computed by STARBURST99 (Leitherer et al. 1999) for an instantaneous starburst in a star cluster of $10^6 M_\odot$ as a function of time from the burst. The solid curve refers to the total energy of stellar wind and supernova and the dotted curve is the contribution of supernovae only. Credits: Dekel et al. 2023

themselves, absorbing short-wavelength radiation (in particular in the UV range) and re-emitting the same amount of energy at longer wavelength (infrared range) as black-body emission.

The dust extinction A_λ is wavelength-dependent and it is defined as follows:

$$A_\lambda = -2.5 \log \frac{f_{\text{obs}}(\lambda)}{f_{\text{em}}(\lambda)} \quad (1.71)$$

where $f_{\text{em}}(\lambda)$ is the emitted flux density at wavelength λ and $f_{\text{obs}}(\lambda)$ is the corresponding observed flux density.

Of particular relevance is the dust extinction in the visual band A_V :

$$A_V = -2.5 \log \frac{f_{\text{obs};V}}{f_{\text{em};V}} \quad (1.72)$$

where $f_{\text{em};V}$ is the emitted flux in the visual band and $f_{\text{obs};V}$ is the corresponding observed flux. A_V is the commonly used parameter to describe the dust column density N_d in front of the source. Indeed the dust optical depth is linked to the column density:

$$\tau_\lambda = \int n_d \sigma_{ext} ds \quad (1.73)$$

where n_d is the dust density and the integral is computed along the light path. For uniformly composed dust:

$$\tau_\lambda = N_d \sigma_{ext} \quad (1.74)$$

which means that:

$$\frac{f_{\text{obs};V}}{f_{\text{em};V}} = e^{-\tau_\lambda} = e^{-N_d \sigma_{ext}} \quad (1.75)$$

And finally:

$$A_V = 1.086 N_d \sigma_{ext} \quad (1.76)$$

The composition of dust grains determines the shape of the A_λ/A_V function. Many models are present in literature to describe this function based on the type of galaxies studied, and the composition of dust grains which is present.

For local galaxies the dust extinction can be well represented by the [Seaton 1979](#) model (Figure 1.10). The peculiarity of the dust absorption in local galaxies is the ‘220 nm bump’, which is a peaked extinction around this wavelength caused by polycyclic aromatic hydrocarbon in the interstellar medium. This wavelength dependence indicates that there must exist in the ISM a population of large grains ($a \gtrsim 100 \text{ nm}$) to account for the extinction at visible wavelengths, and a population of small grains ($a \lesssim 10 \text{ nm}$) to account for the far-UV extinction.

Another commonly used dust extinction model is the Calzetti model ([Calzetti et al. 2000](#)) which is computed by observing local starbursting galaxies. In the dust extinction curve of these galaxies, the UV bump is not present (Figure 1.10). The Calzetti law appears to agree with the dust extinction observed in high redshift galaxies ([Scoville et al. 2015](#)).

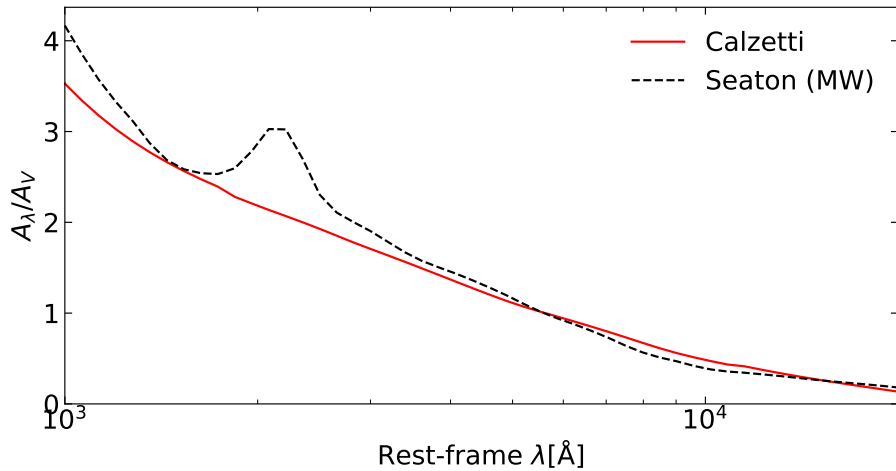


Figure 1.10: Extinction by the Calzetti model in comparison with the Seaton model for the Milky Way dust with the characteristic 220 nm bump. On the x -axis there is the rest frame wavelength, while on the y -axis there is the dust extinction compared to the visual one.

The formation of dust in galaxies is not an instantaneous process. Stellar winds, while continuous, produce small amounts of dust over time, requiring a long period to accumulate significant mass. Additionally, stars need time to evolve into phases that

generate these winds, such as AGB, Wolf-Rayet²⁰, and red supergiant²¹ phases. On the other hand, supernovae release all their dust at once when exploding, but there is a time delay for a burst of star formation to produce supernovae. Furthermore, the interaction of supernova ejecta with the interstellar medium creates a reverse shock that partially destroys the just-formed dust grains. The dust mass produced by Wolf-Rayet stars and red supergiants is relatively minor. The evolution of dust mass produced by a simple stellar population over time is shown in Figure 1.11. Supernovae, even accounting for the reverse shock, are the predominant dust source up to about ~ 1 Gyr, making them the main contributors of dust in galaxies at redshift $z > 6$.

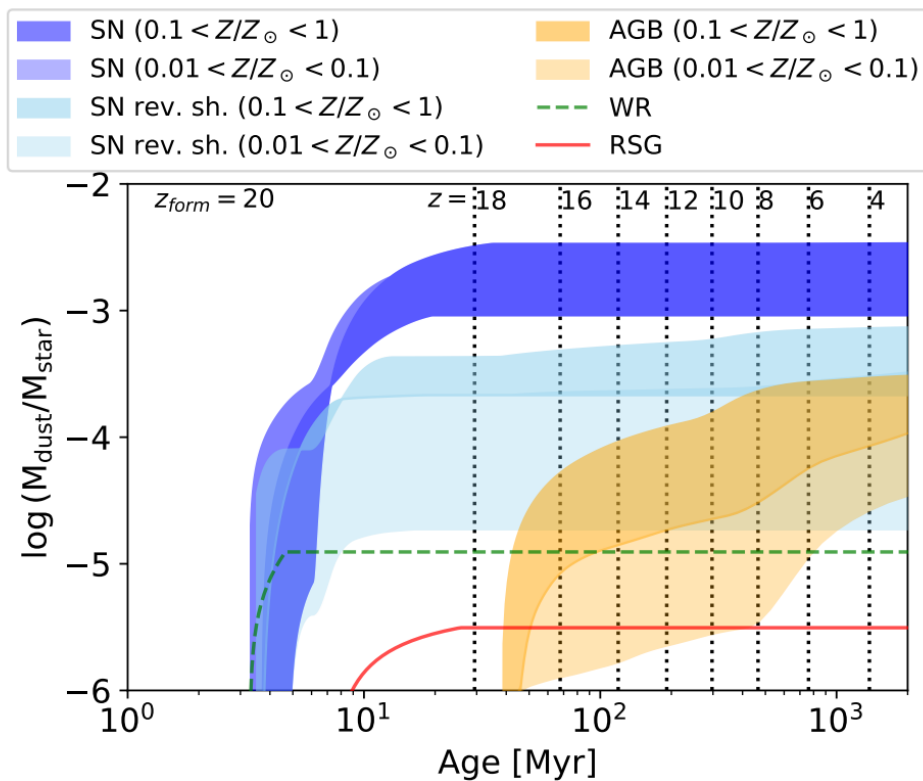


Figure 1.11: Typical time scale of dust formation. It is assumed that the stars formed as a burst at redshift $z = 20$. The dust produced is shown as a function of time and metallicity. In blue the contribution from SNe, in light blue the same contribution but considering the reverse shock. Yellow shows the dust produced by asymptotic giant branch stars (AGB). The green and red lines represent Wolf-Rayet (WR) stars and red supergiants (RSG), respectively. Credits: Schneider & Maiolino 2024

²⁰Wolf-Rayet stars are hot ($\gtrsim 25\,000$ K), massive stars ($\gtrsim 20 M_{\odot}$) with a high rate of mass loss. Strong, broad emission lines arise from the winds of material being blown off the stars.

²¹Red supergiants is a late stage of evolution massive stars ($\gtrsim 10 M_{\odot}$)

C H A P T E R



The *Blue monsters* problem

After the Big Bang, it is widely accepted that the Universe went to a rapidly increasing growth called *inflation*. During this period, the first density fluctuations formed and were later seeds for the formation of the first structures (Sec. 1.5). The dark matter component (having no pressure) started to collapse as soon as these fluctuations formed, while the baryonic matter was not able to collapse until the decoupling from radiation occurred (Sec. 1.5.1).

After the last scattering, the Universe continued to cool down, becoming a dark place without stars or galaxies. During this period, known as the *Dark Ages*, the hydrogen in the Universe remained mostly neutral. This made the Universe appear completely dark to human eyes, as no visible light was produced except for the faint glow of the Cosmic Microwave Background (CMB). The *Dark Ages* ended only when the first stars and galaxies formed, illuminating the cosmos for the first time since the CMB.

The formation of the first galaxies is a major transition in the evolution of the Universe. These first galaxies with the first low metallicity stars transformed the intergalactic medium from neutral to ionized. This period ending at redshift $z \approx 6$ is known as the Epoch of Reionization (EoR).

The study of the first galaxies is a key ingredient to understanding the evolution of the Universe in the first Gyr of its history.

Before the launch of the *James Webb Space Telescope* (JWST, described in Chapter 3), only a few dozen galaxies were identified within the first 700 Myr of the Universe using the Hubble Space Telescope. The farthest known galaxy was at a redshift $z \sim 11$ (Jiang et al. 2021). However, the early-Universe landscape changed with the advent of the JWST.

Even during its first program, the JWST has detected numerous super-early ($z \gtrsim 10$) galaxy photometric candidates (Adams et al. 2023, Naidu et al. 2022, Finkelstein et al. 2022, Castellano et al. 2022, Donnan et al. 2023). Some of these candidates were later confirmed by spectroscopic analysis, despite some discrepancies (Arrabal Haro

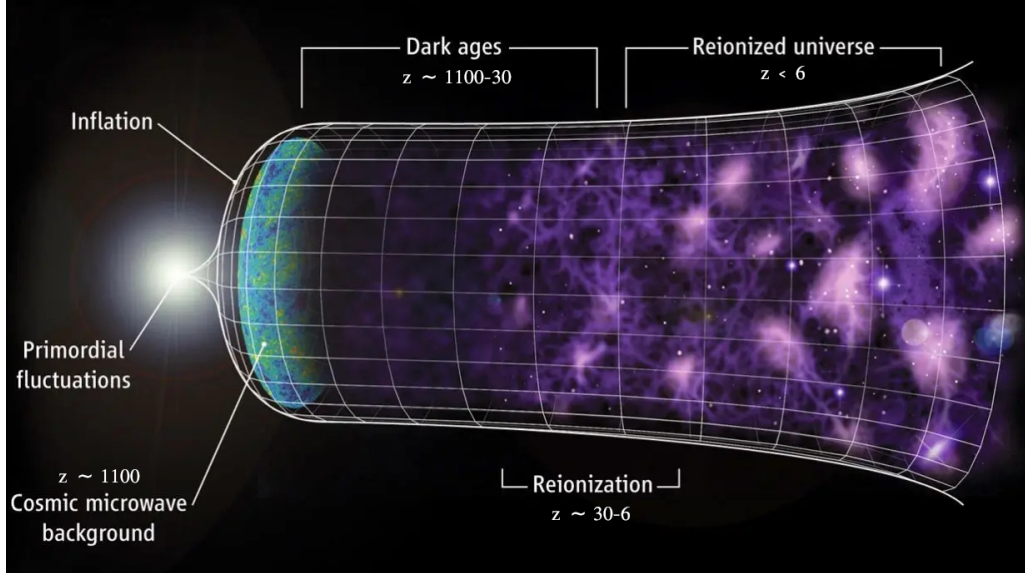


Figure 2.1: Picture of the evolution of the Universe from the first fluctuations to the present days. The various phases are discussed in the text. Credits: [Faucher-Giguère et al. 2008](#)

(et al. 2023). The observed galaxies were mostly bright and with a huge rest-frame UV emission (as described in Sec. 2.1). The bright end of the observed galaxies are being named *blue monsters* (Ziparo et al. 2023): they are termed "blue" because of their exceptionally bright UV luminosity and UV slope (Sec. 2.1.2), which indicate strong star formation and young stellar populations. The term "monsters" highlights their great brightness. The presented characteristics of these galaxies are extensively discussed in Arrabal Haro et al. 2023, Bunker et al. 2023a and will be presented in Sec. 2.1. The name *blue monsters* wants to underscore how these galaxies challenge conventional models of how galaxies formed in the Epoch of Reionization.

2.1 Evidences of super-early galaxies

2.1.1 The ultraviolet luminosity function

The exceptional brightness of the ‘blue monsters’ can be better understood by examining the ultraviolet (UV) luminosity function at redshifts $z \gtrsim 10$. The UV luminosity function is a measure of the density of galaxies relative to their luminosity at 1500 Å.

Supposing to divide the absolute magnitude (AB absolute magnitude at 1500 Å defined in Eq. 1) of galaxies in equal-sized bins, the UV luminosity function would be the number of observed galaxies in each bin. Given that the luminosity in the UV of a galaxy is mass-dependent, the UV luminosity function is related to the stellar mass function (Sec. 1.8) but it also depends on the dust extinction and the history of star formation of the galaxy.

The first studies based on JWST have revealed an overabundance of galaxies at the brightest end (at absolute UV magnitude $M_{\text{UV}} \approx -22$) of the UV luminosity function

at high redshift. This discovery has immediately excited the scientific community. In particular, the UV luminosity function of galaxies has been observed to vary slowly with redshift, ranging from $8 < z < 11$, and the bright end of this function is approximately ten times higher (Finkelstein et al. 2023, McLeod et al. 2024) than most theoretical galaxy evolution models (e.g. Behroozi et al. 2020) and empirical predictions based on studies at lower redshifts (e.g., Bouwens et al. 2021). The tension on the luminosity function can be seen in Figure 2.2.

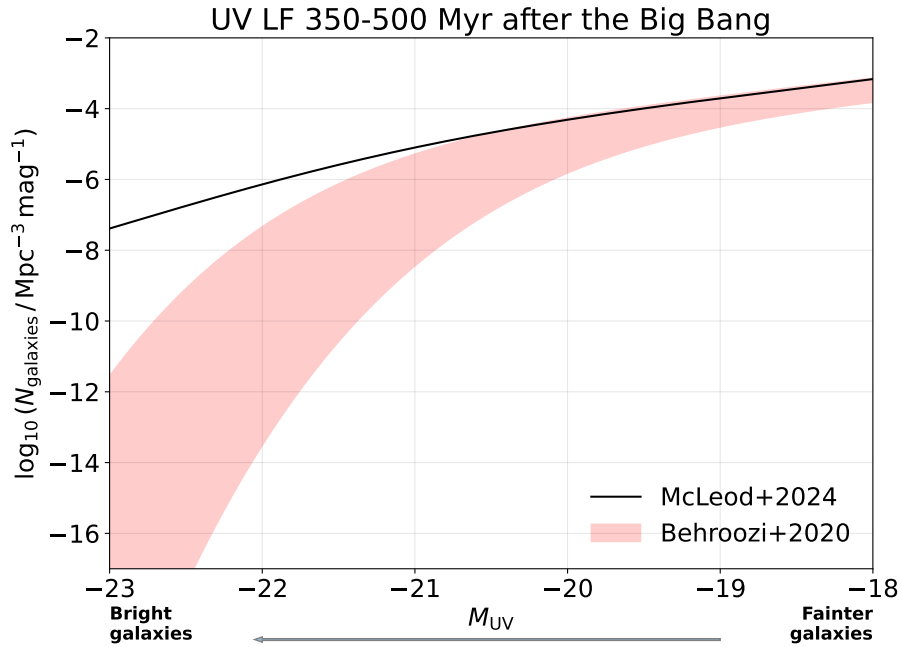


Figure 2.2: The UV luminosity function at redshift $z = 9.5 - 12.5$ (350 – 500 Myr after the Big Bang). The y -axis denotes the number of galaxies per mega-parsec cubed per unit of magnitude, while the x -axis represents the AB magnitude at 1500 Å. In the plot the currently available UV luminosity function from JWST data for the redshift range $z = 9.5 - 12.5$ (McLeod et al. 2024, represented by the black line) is compared with its expected values from Behroozi et al. 2020 (the pink region). According to the latter study, the UV luminosity function would rapidly decrease in this redshift range: the upper envelope of the pink region corresponds to $z = 9.5$, while the lower envelope corresponds to $z = 12.5$. This is not compatible with what has been observed.

2.1.2 The ultraviolet continuum slope

All these bright galaxies, as described by Arrabal Haro et al. 2023 and Bunker et al. 2023a, have another peculiar characteristic: the strong UV continuum slope. The spectrum of a galaxy in the rest-frame ultraviolet band ($150 \text{ nm} < \lambda_0 < 300 \text{ nm}$) can be well modeled by a power-law of the form $f_\lambda \propto \lambda^{-\beta}$, with β called the UV continuum slope.

The ‘blue monsters’ reveal a spectral ultraviolet emission with β values $\gtrsim 2$. Such values are higher than what is observed in the lower redshift galaxies. Such an high β suggest that:

- These galaxies formed recently as they are made of a young stellar population. In fact, the UV emission is strong for massive stars that have a short lifetime.

Spectra of simple stellar populations and their β values are visible in Figure 2.3

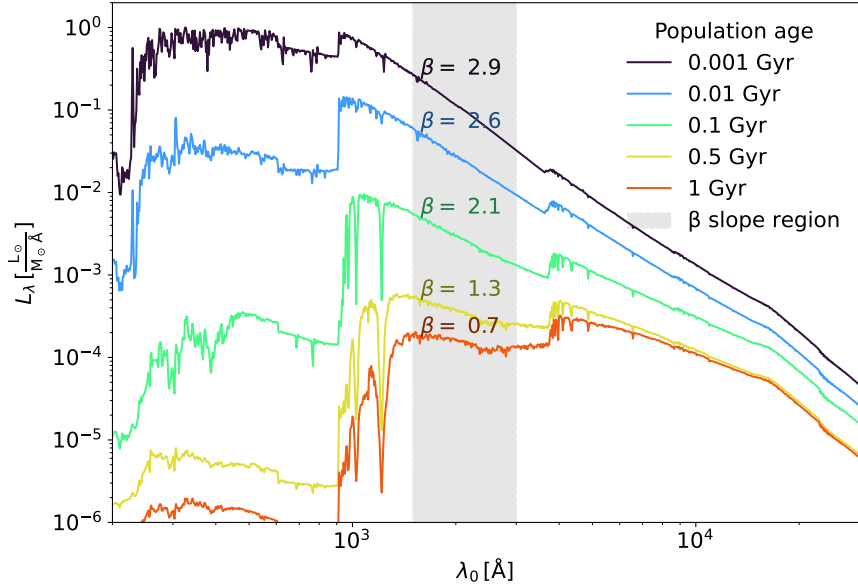


Figure 2.3: Simple stellar population spectra of different ages. The stellar models used to synthesize these spectra are taken from BPASS (Byrne et al. 2022, Eldridge et al. 2017a, see Sec. 4.1.1). The initial mass function, which is the density number of stars with a certain mass born for a gas cloud, is assumed to be the one from Kroupa 2001.

On the x -axis the rest-frame wavelength is present while the y -axis denotes the luminosity of the population in solar luminosities per Angstrom per solar mass. No dust absorption is present. The gray region is where the β slope is computed in literature. For each spectrum, the corresponding β slope is written on the graph itself.

- There is a low dust absorption from these galaxies. The presence of dust changes the slope of the continuum emission decreasing the emission at shorter (i.e. bluer) wavelength returning a galaxy relatively brighter at longer (i.e. redder) wavelength, consequently reducing the slope (Figure 2.4)

The high β value is still a debated topic. Observed high values of β are not compatible with strong dust extinction, which would lower the slope in the UV band (Sec. 2.4). However, such bright and massive galaxies should have produced large amounts of dust. This dust, combined with the observed compactness of these high-redshift galaxies (≈ 100 pc) Arrabal Haro et al. 2023, would result in significant dust extinction, leading to a β value smaller than 2.

2.2 The UV luminosity function issue: proposed theories

The observation of the anomalously high density of bright galaxies at redshift $z > 10$ (Sec. 2.1) has opened debated questions among the astronomical community, leading

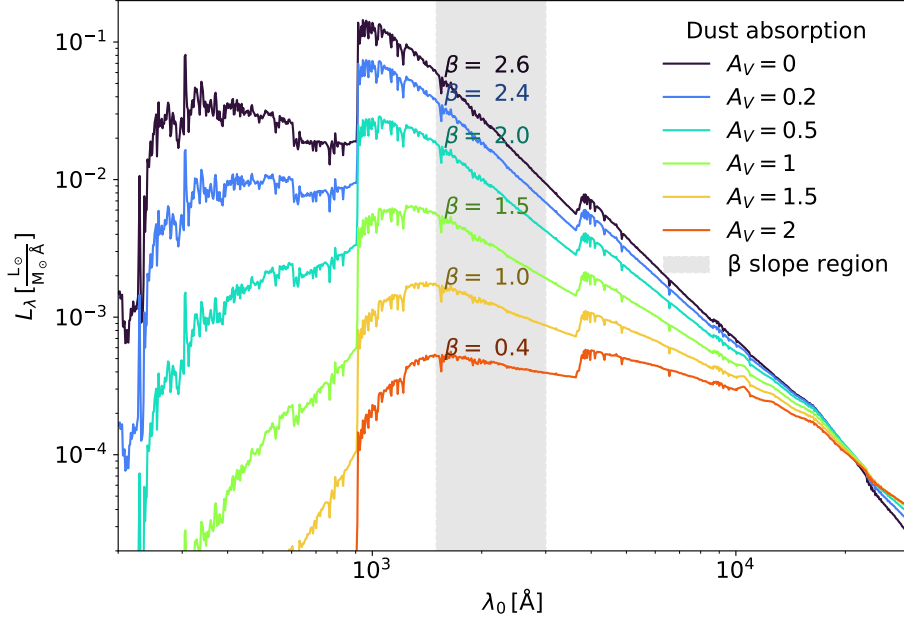


Figure 2.4: Simple stellar population spectra of age 0.01 Gyr with different dust absorptions. Details about the initial mass function, the stellar models, the axis, and the gray region are described in Figure 2.3. The dust model used is Calzetti et al. 2000 with varying A_V . A_V is the green extinction by dust defined as $A_V = -2.5 \log \frac{f_{\text{obs};V}}{f_{\text{em};V}}$ where $f_{\text{em};V}$ is the emitted flux in the visual band and $f_{\text{obs};V}$ is the corresponding observed flux.

to a range of possible explanations. Each explanation proposes a different mechanism that might account for the observed phenomena. In this section and the next one, we present an overview of some of these theories. We stress that these theories are not necessarily in contrast to one another, but the real explanation is probably a combination of more than one of the effects described here.

2.2.1 Changes to the cosmological framework

New cosmological theories (Boylan-Kolchin 2023, Lovell et al. 2023a, Steinhardt et al. 2023) suggest that the observed UV luminosity function can highlight some needed changes to the Λ CDM model. Instead of focusing on the galaxy and stars, these theories tweak (or add) the cosmological parameters to reproduce a different halo mass function. Because the dark matter haloes are potential well for baryons in the formation of galaxies (Sec. 1.8), a larger number of massive dark matter haloes may explain the overabundance of bright massive galaxies at high redshift. The main idea is to account for earlier structure formation and a higher abundance of haloes at fixed mass at high redshift. An example of a model that might provide such a deviation is the addition of *Early Dark Energy* to Λ CDM (Klypin et al. 2021), originally proposed as a solution to the *Hubble tension*, which is the incompatibility of the Hubble constants values (see Sec. 1.2) measured from the cosmic microwave background respect to the one measured with the distance ladder (measure of distances and

redshift of object - as supernovae Ia - on cosmological scales).

In this thesis, the cosmological perspective on the UV luminosity function issue will be excluded in favor of astrophysical theories that explain the *blue monsters* problem by focusing on the physics of stars and the baryonic matter of galaxies.

Fixing the cosmological framework to the Λ CDM one, the problem of the UV luminosity function may be resolved by identifying physical processes that enhance the ultraviolet light observed from galaxies beyond our current expectations. The UV light from a galaxy can be modeled as follows:

$$L_{UV} \propto \text{SFR} \kappa_{UV} e^{-\tau}$$

where SFR is the star formation rate¹ of the galaxy, κ_{UV} is the conversion factor from star formation rate to UV luminosity and τ is the UV dust optical depth. In the next subsection, different astrophysical models will be presented that may explain a change in these factors to reproduce the UV luminosity function observed:

- In Sec. 2.2.2 it is explored the possibility that massive stars would be more probable in high redshift galaxies, which would modify the κ_{UV} parameter.
- In Sec. 2.2.3 and Sec. 2.2.4 two different theories try to explain an enhanced SFR.
- In Sec. 2.2.5 the τ term is discussed.

2.2.2 Evolving initial mass function

The initial mass function (IMF) is the probability distribution of the mass of newborn stars from a molecular cloud.

Some studies suggest that the IMF of super-early galaxies differs from that of local galaxies (e.g., Finkelstein et al. 2023, Trinca et al. 2024). In particular, they propose an IMF that slightly favors higher-mass stars at higher redshifts. Since UV light is produced by massive stars, such an initial mass function would result in brighter UV galaxies, all else being equal.

The first stars born from the primordial gas (Population III stars) were predicted to have a top-heavy IMF (e.g., Bromm et al. 2001, Clarke & Bromm 2003), due to both the extremely low metallicity and the cosmic background radiation (e.g., Larson 1998). Authors supporting the hypothesis that the UV luminosity function issue can be explained by a top-heavy IMF, argue that some stars in these primordial galaxies may have intermediate conditions between Pop III stars and the stars we observe in the local Universe. For this reason, they expect these stars to still have an intermediate top-heavy IMF. To boost the expected luminosity function to the observed one, a contribution from almost metal-free stars with an IMF peaking at

¹Rate of production of star expressed as mass over time. The UV emission is sensitive to the last ~ 100 Myr of star formation (see Figure 2.3)

$10 - 40 M_{\odot}$, as proposed by [Tumlinson 2006](#), is required if the average metallicity in the galaxy of $Z = 0.02 Z_{\odot}$, according to [Finkelstein et al. 2023](#).

Instead, [Trinca et al. 2024](#) proposes an IMF that is a combination of a [Kroupa 2001](#) IMF:

$$\Phi(m_{\star})dm_{\star} \propto \begin{cases} m_{\star}^{-1.3} & \text{for } 0.08 M_{\odot} \leq m_{\star} < 0.5 M_{\odot} \\ m_{\star}^{-2.3} & \text{for } 0.5 M_{\odot} \leq m_{\star} < 300 M_{\odot} \end{cases} \quad (2.1)$$

and a logarithmic flat IMF for $10 M_{\odot} \leq m_{\star} < 300 M_{\odot}$:

$$\Phi(m_{\star})dm_{\star} \propto m_{\star}^{-1} \quad (2.2)$$

with the relative weight of the Log-flat IMF being redshift-dependent: $w_{LF} = 0.04(z - 5)$. This weight correctly reproduces the Kroupa IMF for low-redshift galaxies. However, even this composite IMF cannot completely explain the observed UV luminosity function ([Trinca et al. 2024](#)).

The transition between the top-heavy IMF of PopIII stars and the present-day IMF is expected to be at metallicities not higher than $Z \sim 10^{-3} Z_{\odot}$ (see [Venditti et al. 2023](#) for a detailed discussion) and even if PopIII stars were present until $z \sim 6$ their contribution to the total luminosity of the first galaxies cannot be enough to solve the UV luminosity function tension. Even in the case other studies, that hypothesize a more gradual transition between the two IMF at $Z \sim 10^{-2} Z_{\odot}$ like [Chon et al. 2021](#), was proven to be right, then the theoretical UV luminosity function would be more similar to the observed one, however without being compatible with it ([Trinca et al. 2024](#)).

In conclusion, it seems that an evolving initial mass function might mitigate the problem without solving it.

2.2.3 Stochastic star formation rates

In high redshift galaxies, the star formation is much more bursty than what we observe in the local Universe ([Looser et al. 2023a,b](#)). It seems plausible that the bright end of the UV luminosity function may be populated by starbursting lower mass haloes resulting in an overpopulation of bright galaxies ([Mirocha & Furlanetto 2023](#), [Pallottini & Ferrara 2023](#)). The scatter in the star formation rate of these galaxies at fixed halo mass can indeed boost the abundance of bright galaxies. However, this solution introduces tension elsewhere: in particular typical ages and masses would be expected to be much lower than what is observed. The strong β slope resulting from this theory may be alleviated if non-negligible reddening from dust would be present, suggesting that both star formation and dust production would be more efficient than expected in galaxies at $z \gtrsim 10$ ([Mirocha & Furlanetto 2023](#)).

The stochastic star formation is a key process in the evolution of the first galaxies, but the observed scattering in the star formation rate is too low to explain alone the UV luminosity function observed ([Ciesla et al. 2023](#)).

Finally, the necessity to have an efficient dust absorption in these galaxies is disfavored by far-infrared dust continuum non-detections ([Ziparo et al. 2023](#)) and dust-free

galaxies observations at this early epochs (Nath et al. 2023, Looser et al. 2023a). It should be noted, however, that a population of candidate dust-obscured galaxies has been detected even at $z > 10$ (Rodighiero et al. 2023)

2.2.4 Almost feedback-free star-formation

The star formation in the local Universe is known to be largely inefficient (Moster et al. 2018, Rodríguez-Puebla et al. 2017): only a small fraction of the gas present in molecular clouds is converted into stars in a free-fall time².

Some authors (Li et al. 2023, Dekel et al. 2023, Renzini 2023) consider the possibility that early star formation might proceed so fast that minimal feedback effects (Sec. 1.9), such as winds and supernovae, would be present. From energy considerations (Dekel & Silk 1986), supernovae efficiently suppress the star formation in haloes with a mass lower than $10^{10} M_{\odot}$ at redshift $z \sim 10$. The observed galaxies have estimated halo masses of the order of the threshold found and, in principle, they would be susceptible to supernovae feedback (Dekel et al. 2023).

The feedback-free theories assert that because the feedback from winds³ and supernovae explosions has a delay of about $\gtrsim 1$ Myr (Dekel et al. 2023), then if the free-fall time of molecular clouds is lower than this threshold, it could be converted into stars with efficiencies as high as 100%. The free-fall time t_{ff} is :

$$t_{\text{ff}} = \sqrt{\frac{3\pi}{32G\rho}} \quad (2.3)$$

then, a critical density of $n \approx 2 \times 10^3 \text{ cm}^{-3}$ is required for the feedback-free star formation to be plausible. Indeed, with this density, the free fall time becomes lower than 1 Myr, and minimal feedback effects would act during the collapse of the cloud. At high redshift, the feedback-free process may be relevant due to the average higher density of galaxies. A large number of bursts of this type might lead to an efficient conversion of gas into stars and brighter galaxies at early time (Figure 2.5).

2.2.5 Brightening due to low dust attenuation

When a galaxy experiences a high star formation rate relative to its mass, its radiation field can be strong enough to disperse the dust it produces. This process results in reduced attenuation of starlight in the UV band, causing these galaxies to appear brighter than anticipated in the UV band and accounting for the steep UV slope.

This theory proposed by Ferrara et al. 2023 and Tsuna et al. 2023 shows that the UV luminosity function can be perfectly reproduced at any redshift, provided that the dust attenuation is negligible at redshifts $z \gtrsim 10$.

²This is the time in which the gas in molecular cloud of size larger than the Jeans radius - Eq. 1.38 - would collapse if no heating processes would be present

³Stellar winds generate as soon as massive stars formed but have a low impact at metallicities $Z < 0.2 Z_{\odot}$ in the first 2 Myr (Dekel et al. 2023)

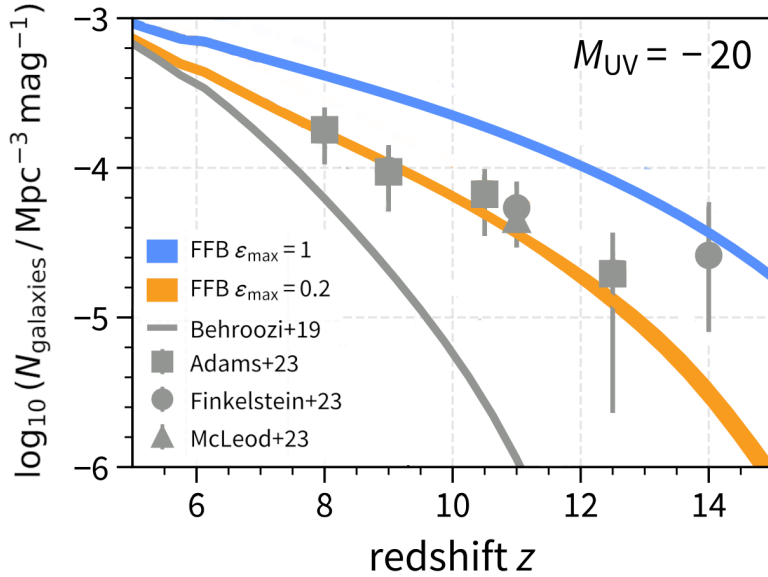


Figure 2.5: Feedback free luminosity function at $M_{UV} = -20$ as a function of redshift. In gray observational points from [Adams et al. 2023](#), [Finkelstein et al. 2023](#), [McLeod et al. 2024](#). The gray line is the [Behroozi et al. 2020](#) model, while the orange and blue lines are data extracted using an almost feedback-free model with different maximum efficiency. Credits: [Li et al. 2023](#)

As explained by [Ferrara 2024](#) the lack of dust absorption in these high-redshift galaxies may be explained by a strong star formation able to produce radiation-driven outflows and disperse the dust. In fact, the minimum luminosity a galaxy should have to produce such a phenomenon is the galactic Eddington luminosity L_E . The force from the radiative field on dust at distance r from the emitting source of luminosity L is

$$F_r = \frac{L}{4\pi r^2} \frac{\sigma}{c} \quad (2.4)$$

where σ is the cross-section of radiation-matter interaction. According to [Fiore et al. 2023](#), $\sigma = A\sigma_T = 100 - 600\sigma_T$ with σ_T the Thomson scattering cross-section. So, supposing that the radiation pressure from the stars acts on dust bonded to the gas by Coulomb and viscous forces ([Fabian et al. 2006](#)), and because the gravitational force on ionized Hydrogen from the galaxy of mass M is

$$F_g = G \frac{M m_p}{r^2} \quad (2.5)$$

therefore the Eddington luminosity is

$$L_E = \frac{4\pi G M m_p c}{A\sigma_T} \quad (2.6)$$

where m_p is the proton mass.

It can be shown ([Ferrara 2024](#)) that the galaxies with enough star formation to exceed the Eddington luminosity are the ones with a specific star formation rate

sSFR := $\frac{\text{SFR}}{M}$ greater than

$$\text{sSFR} > 25 \left(\frac{100}{A} \right) \text{Gyr}^{-1}$$

In a simplified model we can express the SFR and the stellar mass M_\star of a galaxy as follows:

$$\text{SFR} = \epsilon f_b \frac{M}{t_{\text{ff}}} \quad (2.7)$$

$$M_\star = \langle \epsilon \rangle f_b M \quad (2.8)$$

where ϵ is the gas-to-star efficiency factor, $\langle \epsilon \rangle$ is its average on the history of the galaxy, f_b is the baryon-to-dark matter ratio, t_{ff} is the free-fall time of the filamentary gas into the halo and M is the dark matter halo mass.

From Eq. 2.3 $t_{\text{ff}} \propto \rho^{-1/2}$. Using Eq. 2.8 and Eq. 1.27 the specific star formation rate is:

$$\text{sSFR} \propto \frac{\epsilon}{\langle \epsilon \rangle} (1+z)^{3/2} \quad (2.9)$$

Since the specific star formation rate is expected to increase as a power law of $(1+z)$, where z is the redshift, it is natural that at some point, going back in time, most galaxies were super-Eddington (Figure 2.6), produced outflows, thus being dust-free and increasing the luminosity function (Figure 2.7).

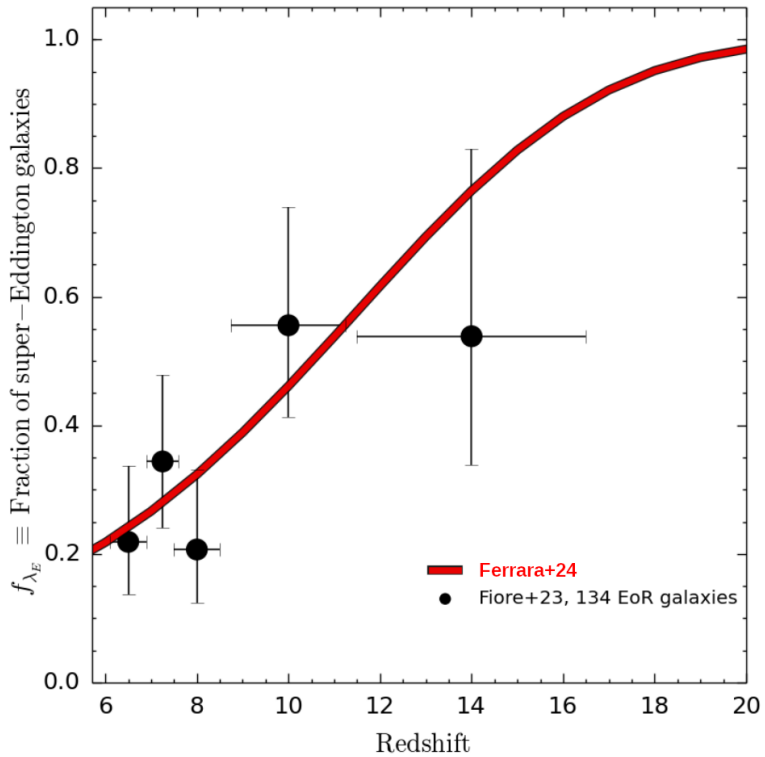


Figure 2.6: Fraction of super-Eddington galaxies (red curve) in a model for which sSFR $\propto (1 + z)^{3/2}$, compared with available data from [Fiore et al. 2023](#). Credits: [Ferrara 2024](#)

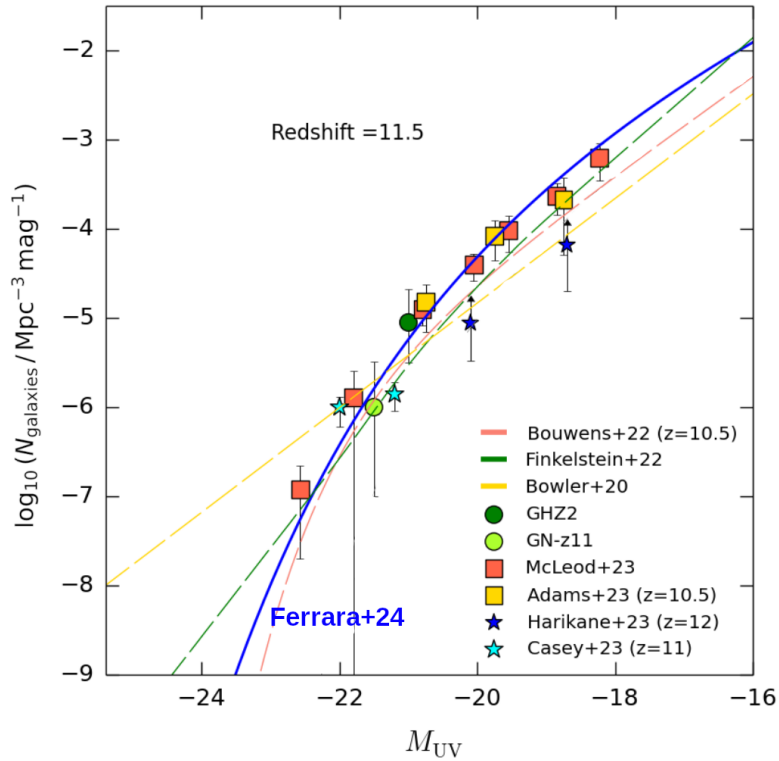


Figure 2.7: Almost dust-free luminosity function at redshift $z = 11.5$ (blue line) compared to other UV luminosity functions and the available observation data. Credits: [Ferrara 2024](#)

CHAPTER



The James Webb Space Telescope and JADES data

The James Webb Space Telescope (JWST) is an infrared-optimized telescope. Launched in December 2021, the JWST, with its 6.6m wide hexagonal primary mirror was conceived to study the formation and evolution of galaxies in the first Gyr of the history of the Universe as one of its main goals.

Sec. 3.1 briefly discuss the characteristics of this telescope, in Sec. 3.2 we will present the Near InfRared Spectrograph (NIRSpec), one of the scientific instruments onboard of JWST. In Sec. 3.3 we will show the extraction Pipeline for JWST NIRSpec spectra. Sec. 3.4, 3.5 and 3.6 are dedicated to the JWST Advanced Deep Extragalactic Survey (JADES), the data selection and the resolving power to use in our analysis.

3.1 JWST

The James Webb Space Telescope (JWST) represents a transformative advancement in space-based astronomy, offering unprecedented capabilities in the observation of the mid-infrared to near-infrared wavelengths. JWST offers angular resolutions up to 0.1 arcsec, comparable to and even surpassing the capabilities of the Hubble Space Telescope (HST). In this section, we will present JWST properties following Gardner et al. 2006.

JWST consists of a primary mirror array of 18 hexagonal segments made from beryllium and coated with gold, forming a total diameter of 6.5 meters. This large mirror size is critical for capturing high-resolution images and spectra. Remembering that the angular resolution of a telescope is:

$$\theta \propto \frac{\lambda}{D} \tag{3.1}$$

where λ is the wavelength and D the size of the primary mirror. Using $D = 6.5\text{ m}$ and $\lambda = 3\text{ }\mu\text{m}$ (which is in the middle of the wavelengths covered by the near-infrared

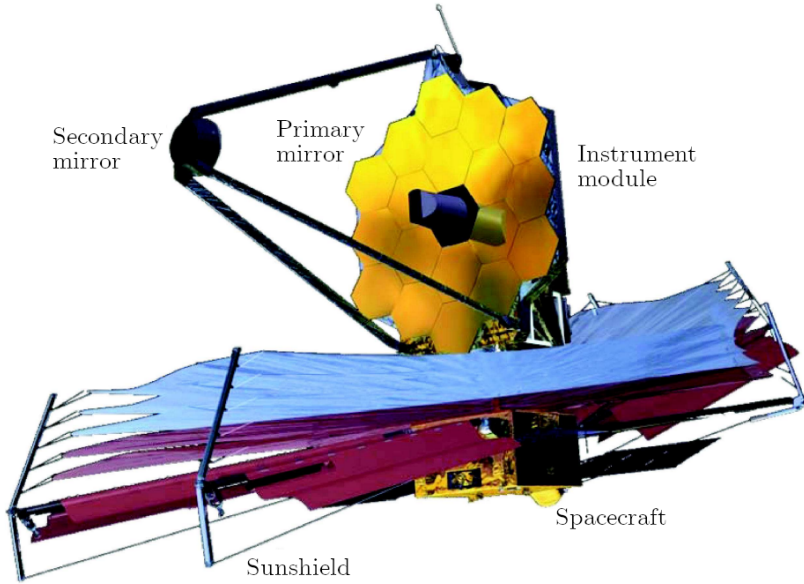


Figure 3.1: A drawing of the principal components of the James Webb Space Telescope once it has been unfolded in space. Credits: [Gardner et al. 2006](#)

spectrograph prism: Sec. 3.2) it follows that:

$$\theta \approx 0.1 \text{ arcsec} \quad (3.2)$$

The telescope is equipped with four primary scientific instruments: the Near Infrared Camera (NIRCam), the Near Infrared Spectrograph (NIRSpec), the Mid-Infrared Instrument (MIRI), and the Fine Guidance Sensor/Near InfraRed Imager and Slitless Spectrograph (FGS/NIRISS).

The telescope is situated at the second Lagrange point (L2) of the Sun-Earth system, approximately 1.5 million kilometers from Earth. This location allows JWST to maintain a stable environment shielded from the Sun's heat. Indeed, because JWST is an infrared-dedicated telescope it must be cold ($T \lesssim 50 \text{ K}$): the thermal emission is one of the main background sources at the wavelengths JWST works on (Sec. 3.3). JWST is capable of covering a wavelength range from 0.6 to 28 micrometers. Due to its position in space, it avoids the atmospheric absorption that impacts ground-based telescopes and is particularly relevant at infrared wavelengths where many molecular telluric absorption bands are present, as shown in Figure 3.2.

Using its characteristics, the major goals of the JWST can be summarized as:

- **Early Universe Observations:** Identifying the first luminous sources to form and determining the ionization history of the early Universe.
- **Galaxy Formation and Evolution:** Investigating the assembly and growth of galaxies over cosmic time: the morphological evolution, the metal enrichment process, and the coevolution of supermassive black holes.
- **The Birth of Stars and Protoplanetary Systems:** Studying the early evolution of the stars and the formation of planetary systems

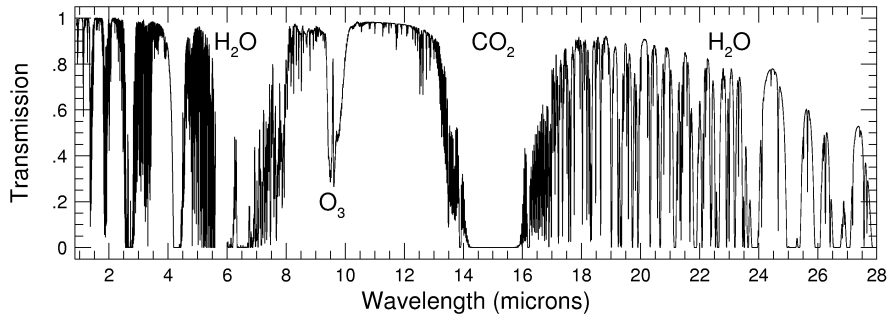


Figure 3.2: Earth’s atmospheric transmission at JWST wavelengths. If JWST was on Earth, many wavelength bands would not be accessible. Credits: Data calculated by Steven Lord and provided by the [Gemini observatory](#)

- **Planetary Systems and the Origins of Life:** Determining the physical and chemical properties of planetary systems including our own, and investigating the potential for the origins of life in those systems.

3.2 NIRSpec

One of the four instruments with which the JWST is equipped is the Near InfraRed Spectrograph ([Jakobsen et al. 2022](#), [Böker et al. 2023](#)) which provides spectroscopy from 0.6μ to $5.3\mu\text{m}$ on a sensor spanning a $3.4'\times 3.6'$ field of view. The spectrograph can be used in three different modes:

- **Fixed slit spectroscopy:** This is the classic spectroscopic mode: the target is centered on the slit and the dispersed light is collected on the sensor. Each source that fits in the slit will be dispersed.
- **Multi object spectroscopy:** This mode uses tiny configurable shutters which compose a micro-shutter array. Different sources within the field of view can be exposed simultaneously by opening the shutters centered on the selected targets.
- **Integral field spectroscopy:** It provides spatially resolved imaging spectroscopy over a $3''\times 3''$ square region.

In the following sections, we will focus on the multi-object spectroscopy (MOS).

3.2.1 The multi-object spectroscopy mode

The possibility to choose the targets and expose multiple objects at a time makes the MOS the preferred mode to be used for high-redshift galaxies. Each shutter of the micro-shutter array (MSA) has a size of $0.20''\times 0.46''$ and so, using Eq. 3.1 and Eq. 3.2, it is clear that it operates in the diffraction-limited mode over a large wavelength range, i.e. the shutter has a width greater than the full width at half maximum of the JWST point spread function (PSF). Indeed, the choice to use slightly

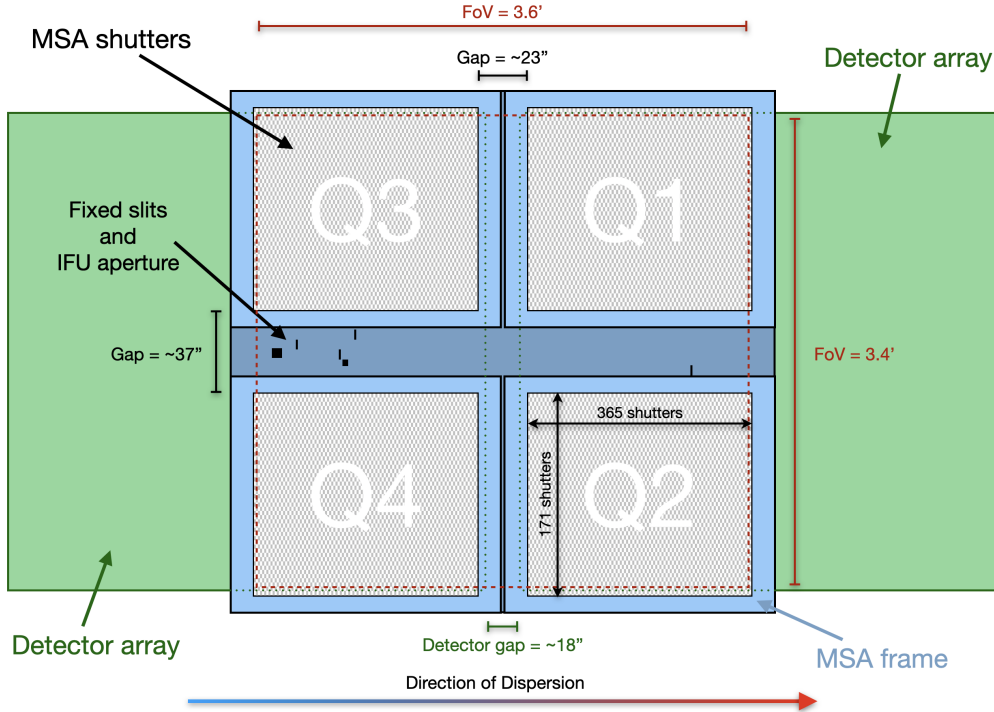


Figure 3.3: A view on NIRSpec: The four micro-shutters array (MSA) are separated by a gap corresponding to the zone where the fixed slits or the integral field (IFU) modes can be used. Each shutter can be opened independently from each other.

oversized¹ shutters were made to maximize the sensitivity, because NIRSpec was optimized for observations of faint objects. As a consequence, NIRSpec is susceptible to the slit effect where an imprint of the intensity distribution of the object across the slit is present in the spectral PSF (This important issue will be discussed and partially solved in Sec. 3.6 and Sec. 4.2).

As we will describe in Sec. 3.3, to remove the background from the target exposures, the MOS is used by opening two or more (generally 3 or 5) shutters, adjacent in the cross-dispersion (spatial) direction, that form a longer ‘slitlet’. After one exposure of the source is completed, the telescope is slightly moved to center the target in each of the shutters of the slitlet. Many exposures with the target in each shutter of the slitlet are then executed. An example of the opened shutters superimposed to the sky is visible in Figure 3.4.

3.2.2 NIRSpec dispersers

The disperser (or dispersing element) is the key element of a spectrograph: it is the part of the spectrograph that disperses incoming light by wavelength. One of the most important characteristics of a disperser is the resolving power R which measures the ability to distinguish closely adjacent features on the spectrum, and which is defined as the ratio between the wavelength of the light λ and the closest

¹Respect to the full width at half maximum of the PSF.

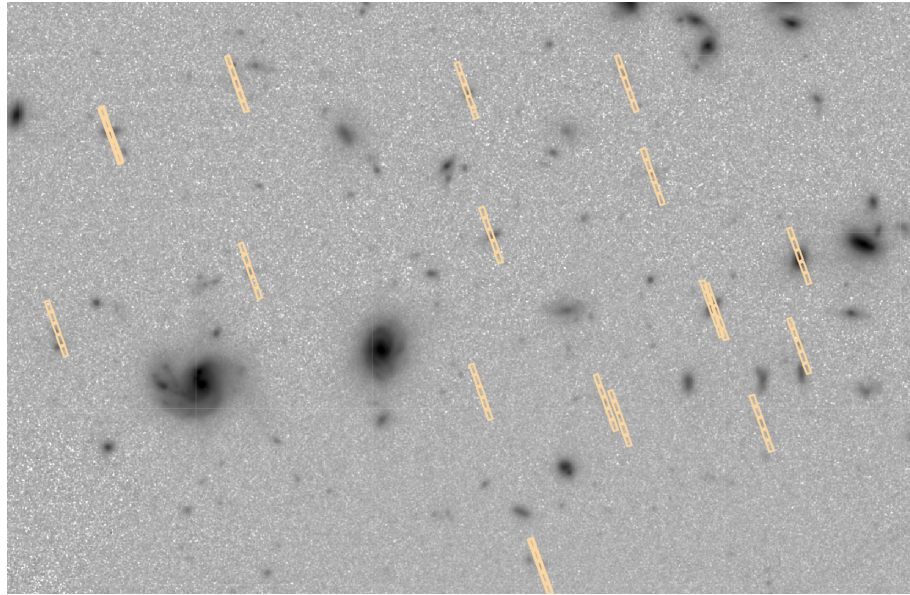


Figure 3.4: An example of the opened shutters in a MOS pointing of the GOODS-N field in the JADES (Sec. 3.4) survey. The grayscale image in the background is a composition of NIRCam exposures at $\approx 4 \mu\text{m}$, while the yellow borders represent the MSA opened shutters. In this case, the slitlets are 5 shutters long.

discernable wavelengths $\Delta\lambda$:

$$R := \frac{\lambda}{\Delta\lambda} \quad (3.3)$$

In general, R is a wavelength-dependent quantity.

The JWST's NIRSpec can be used in combination with 7 dispersers, that cover the wavelength range $0.6 - 5.3 \mu\text{m}$:

- Three high resolution gratings (G140H, G235H, G395H) with $R \approx 2700$
- Three medium resolution gratings (G140M, G235M, G395M) with $R \approx 1000$
- One low-resolution prism $R \approx 100$

Figure 3.5 presents the resolving power and wavelength coverage of each disperser.

Each diffraction grating can only provide clean spectra over a factor of 2 in wavelength due to order contamination: the different orders of the spectrograph overlap on the sensor. For this reason, each disperser has its filter to be used with, to limit the bandwidth and avoid order contamination.

Another important feature of the NIRSpec instrument is its limiting sensitivity. The limiting sensitivity of NIRSpec defines the faintest flux density that can be detected and accurately measured within a given exposure time. This parameter measures the capability of the instrument to observe faint astronomical sources, such as early galaxies. The sensitivity is influenced by several factors, including the instrument's wavelength range, detector efficiency, and the background light from both the instrument and the sky. In this thesis, the NIRSpec sensitivity will be used

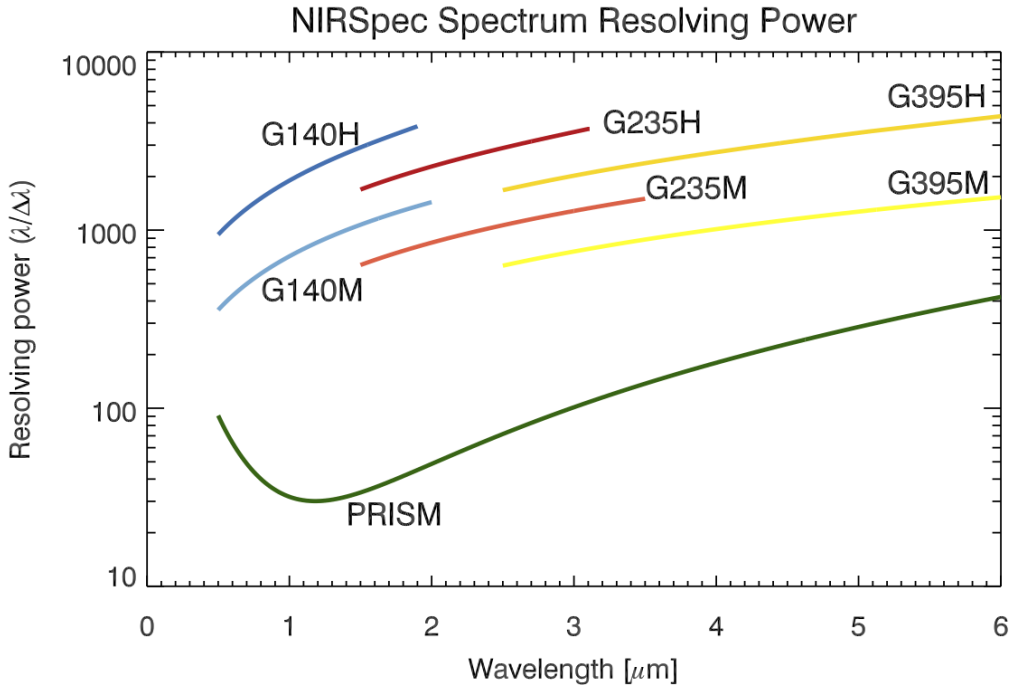


Figure 3.5: The resolving power of the seven NIRSpec’s dispersers as a function of wavelength considering a fully illuminated slit aperture. Credits: [Jakobsen et al. 2022](#), [JWST User Documentation 2016](#)

to generate realistic mock observations of high-redshift galaxies. In Figure 3.6 the sensitivity curves of the dispersers relative to a signal-to-noise ratio of 10 with 10^4 s of integration time are visible. The prism can achieve much higher sensitivity thanks to its lowest dispersion D :

$$D := \frac{\delta\theta}{\delta\lambda}$$

where $\delta\theta$ is the difference in angle dispersion of two wavelengths separated by $\delta\lambda$. Less dispersion means more light is concentrated on each pixel, which boosts the signal and increases the sensitivity of the instrument.

3.3 Data reduction

The result of a MOS observation is a series of spectra on the sensor. An example of such an image is visible in Figure 3.7. The procedure to extract the spectrum of each target from the raw image is performed by the MOS pipeline ([Ferruit et al. 2022](#), [Alves de Oliveira et al. 2018](#)). The main stages of the NIRSpec MOS pipeline to reduce data from the raw image to the 1D spectrum are described in the following paragraphs.

Bias and dark subtraction The process of reading the signal on the sensor generates some noise known as readout noise. Dark current, on the other hand, is the signal generated within the detector even in the absence of light. It is produced

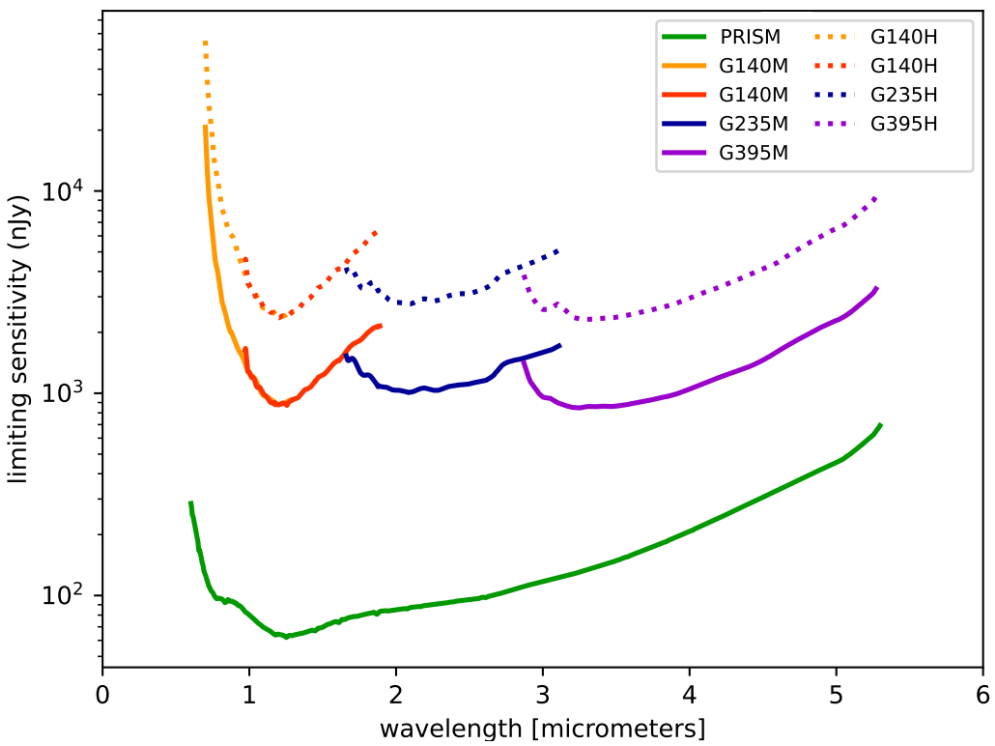


Figure 3.6: NIRSpec sensitivity for a point source centered in an MSA shutter. The plots show for each disperser the continuum sensitivity as a function of wavelength required to reach SNR = 10 per spectral pixel with an integration time of 10067 s. Credits: [JWST User Documentation 2016](#)

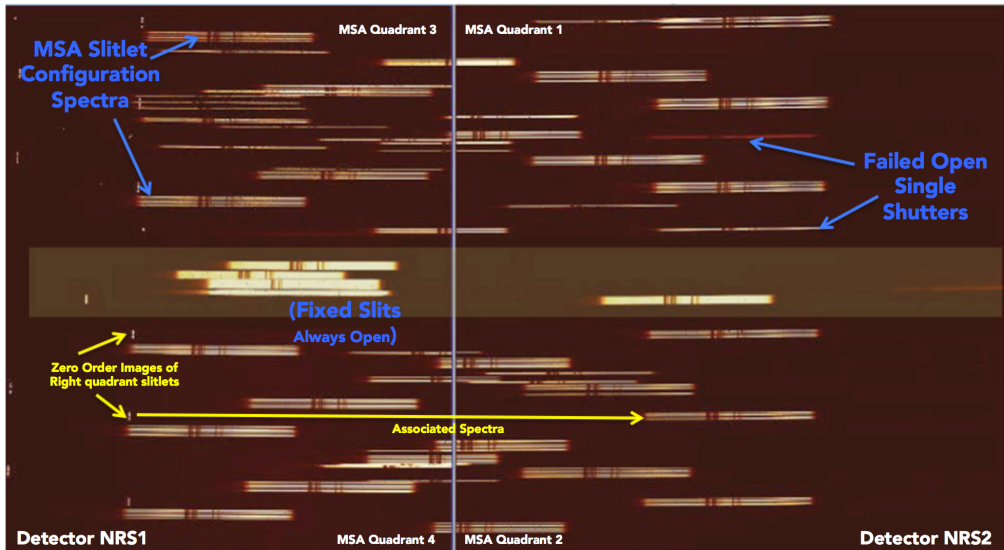


Figure 3.7: An example of NIRSpec MOS mode spectra taken with a calibration flat field lamp and the medium resolution disperser G140M. The MSA is arranged in multiple slitlets. In the figure are visible also some defects of the MSA with some opened single shutters. Credits: [JWST User Documentation 2016](#)

by the random generation of electrons and holes within the depletion region of the electrodes forming the pixels of the sensor. To correct for these effects, dedicated bias frames (zero-exposure images for the readout-noise) and dark frames (images taken with the detector shielded from light for the dark current) are acquired. The average bias and dark frames are then subtracted from the raw science images. This subtraction process removes these unwanted signals generated on the sensor. The dark frames are different from each other due to the random nature of the noise, however, the aim of the dark and bias frames correct the mean fixed-pattern noise. This is the reason for taking an average of multiple exposures.

Flat corrections The flatfield correction is designed to address variations in the signal recorded based on the source location within the field of view (FOV) and the wavelength. Flatfield correction for a spectrograph is more complex than for imaging because each part of the optical path introduces a unique wavelength dependence on the efficiency of transmission and detection. In NIRSpec MOS mode, the challenge is greater because a single detector pixel can be illuminated by different wavelengths depending on which shutter is open. Consequently, the flat correction can only occur after the specific wavelength hitting each pixel is determined. The NIRSpec flatfield correction is divided into three components of the optical path: detectors, spectrograph, and optics.

The detector flatfield (D-flat) corrects for the quantum efficiency² of each pixel of the sensor. The D-flat was measured with 39 monochromatic sources before the sensor was integrated into the instrument.

The spectrograph flatfield (S-flat) corrects for variations in light response between the spectrograph and the sensor. This correction is made with internal lamps of calibration. In the MOS mode, there are too many possibilities for all shutters to have their flatfield measured with all nine standard instrument configurations. This flat is then interpolated from the flatfields taken with a subset of the shutters.

The optics flatfield (F-flat) corrects for losses in transmission and reflections in the instrument's optics. The entire optical path must be used to measure it, so it is measured directly in space. Observations of a spectrophotometric standard star are used to measure this flatfield.

Background subtraction By working in space, JWST does not suffer from the atmospheric background as ground-based observatories, however, there are multiple sources of background signal in the image:

- Emission from the zodiacal light³.
- Parasitic light from zodiacal and Milky Way light which reflects on the instrument optics.

²Quantum efficiency is the measure of the effectiveness of the sensor to convert incident photons into electrons

³The zodiacal light is solar light scattered by dust particles in the solar system which mainly orbits along the ecliptic and so along the zodiacal constellations.

- Thermal emission from the telescope. Due to the low temperature of JWST $T \lesssim 50$ K, this background source is more dominant at mid-infrared than near-infrared wavelengths.
- Parasitic light coming from individual shutters, e.g. the ones that are defective and cannot be closed.
- Cumulative background resulting from the incomplete opacity of the MSA shutters (MSA leakage): the closed shutters still let some light filter from the edge which produces a background on the sensor.

To correctly subtract the background one of the commonly used techniques is ‘nodding’. In this method, the telescope alternates between the target object and adjacent blank sky positions. By comparing the images from these positions, the background noise can be measured and subtracted from the target image.

In NIRSpec MOS mode, nods are defined as offsets of the telescope that move each target source into a new shutter of the same MSA configuration. This is the reason for arranging the MSA in ‘slitlet’. An example of how nodding works is visible in Figure 3.8: in a 3-shutter slitlet configuration three exposures are made centering the physical source in each shutter. For each of the images thus taken, an average of the signals recorded in the other two exposures is subtracted. The advantage of this technique is that each shutter subtracts another exposure of the same shutter meaning that the background is measured with the same local stray light and the same pixels on the detector. This can help, for example, to subtract stray light arriving from other open shutters. In a 3-shutters long slitlet naming A , B and C the exposures taken with the target in the three different shutters, the slitlet image A is corrected with the mean of the B and C exposures. Analogously this holds for the other two exposures. The subtraction operation generates a negative spectrum of the source in the shutters of each slitlet in which the source was not present: indeed one of the averaged exposures used to correct for the background contains the target in that shutter (see Figure 3.8). The results of the background extraction are again the three original exposures but with the background subtracted. The slitlets will be later combined.

Path losses correction Path losses in NIRSpec arise primarily from geometric and diffraction losses. Geometric losses, also known as slit losses, occur when the reduced aperture size limits the incoming flux collected from a target. These losses increase at longer wavelengths due to the broadening of the point spread function (Eq. 3.1) caused by diffraction within the optical system. We want to stress that the impact of geometric losses varies with the source position within the aperture. Diffraction losses occur when the light on the wings of the point spread function exceeds the disperser’s surface area, resulting in partial light loss. Path loss correction in NIRSpec addresses both geometric and diffraction losses together. The modeled aperture loss map for a 3-shutters long slitlet at $2.5\mu\text{m}$ is shown in Figure 3.9 resulting from optical simulations. The path losses are intuitively greater towards the edges of the shutters. Thanks to the point spread function, objects behind the MSA frame are also partially detected, even if with large losses.

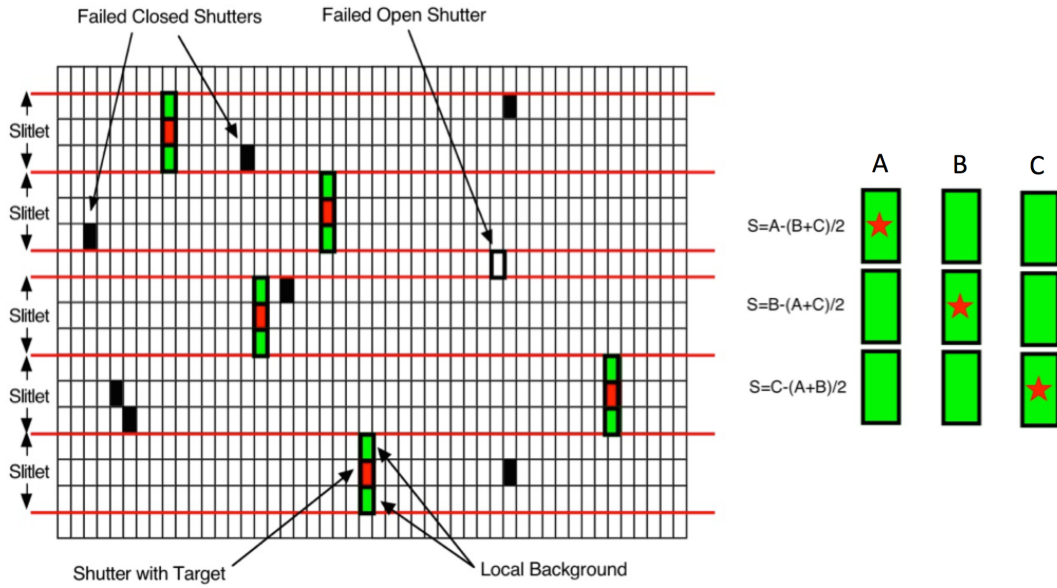


Figure 3.8: An illustration of the methodology of using MSA shutter slitlet nods to subtract background flux. In this case, each slitlet is 3 shutters long. The average between B and C exposures is subtracted from the A slitlet. Similar subtractions are made for B and C slitlets. By not modifying the MSA configuration it is also possible to correct for the parasitic light deriving from other shutters. Credits: [JWST User Documentation 2016](#)

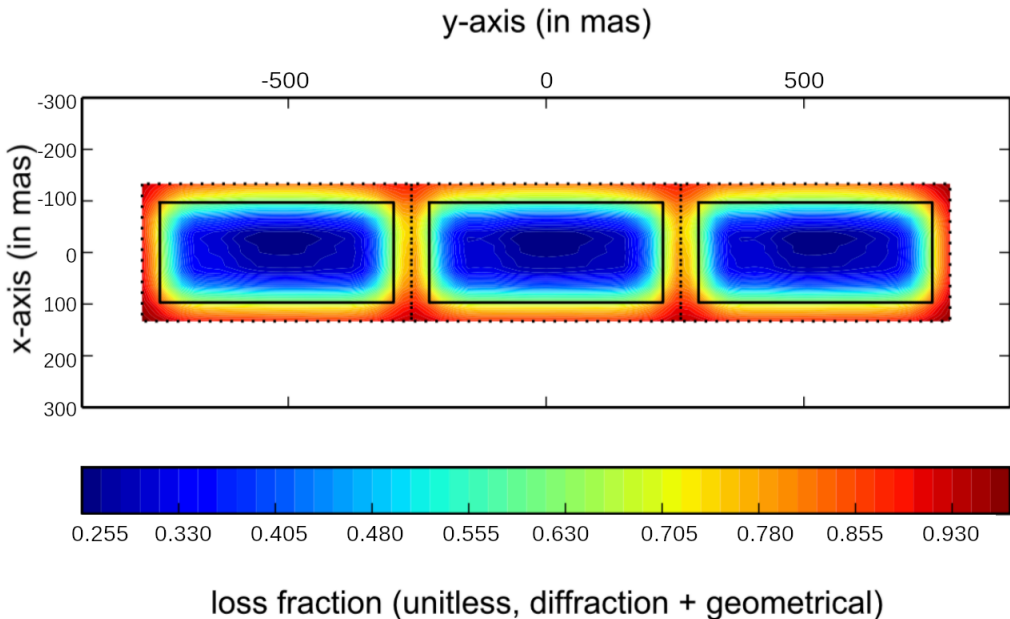


Figure 3.9: Modelled path losses at $2.5 \mu\text{m}$ for a 3-shutters long slitlet. Solid lines show the aperture size, while dashed lines represent the frame size of the MSA shutters

Rectification and integration The image of the spectra on the sensor is distorted. Rectification is the procedure of aligning the spectral data on a 2D-grid to correct for these distortions. The resulting grid has the wavelength on one axis and the spatial information on the other.

The nodding exposures are then combined overlapping the source in each exposure. The result is a rectified 2D spectrum with negative copies of the spectrum alongside. The negative signal comes from the subtraction operation performed during the background correction. An example of the result of the rectification and integration is visible in Figure 3.10. To obtain the 1D spectrum the 2D counterpart is integrated along the spatial direction.

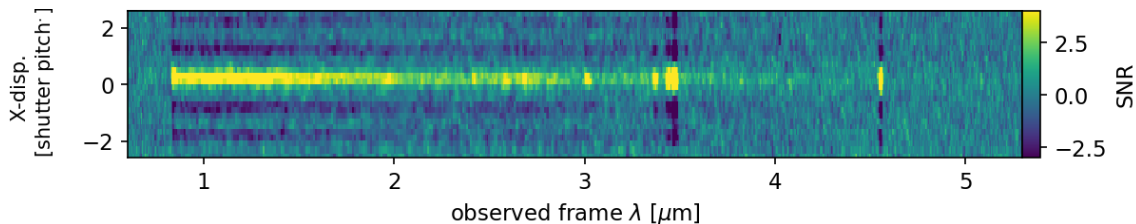


Figure 3.10: Example of a 2D spectrum of a galaxy. The wavelength dispersion is along the x -axis, while the spatial direction along the y -axis is measured in terms of number of MSA shutters. Alongside the spectrum negative copies are present ($\text{SNR} < 0$). Four negative spectra are present, indeed the exposure was taken using a 5-shutters long slitlet

3.4 JADES

The availability of large samples of spectroscopically analyzed galaxies is key to characterizing the relationships between their physical properties and studying their cosmic evolution. Large samples enable the identification of trends and correlations between properties of galaxies, such as their star formation history, metallicity, and dust extinction. These relationships are often not evident in smaller samples and would provide insights into the underlying physical processes that drive galaxy evolution.

At redshifts $z \gtrsim 4$, nothing other than the JWST NIRSpec instrument will be capable of obtaining deep rest-frame optical spectroscopy for large samples of galaxies in the next decades. These redshifts correspond to the early phases of galaxy formation, where galaxies were forming their first stars and assembling their initial structures.

To provide such a sample, the JWST Advanced Deep Extragalactic Survey (JADES) was created (D’Eugenio et al. 2024, Bunker et al. 2023b, Eisenstein et al. 2023). JADES is a collaboration between the JWST NIRCam and NIRSpec Guaranteed Time Observation (GTO) teams, designed to exploit both photometry and spectroscopy advantages. By combining the strengths of NIRCam’s deep, high-resolution imaging with NIRSpec’s powerful spectroscopic capabilities, JADES aims to provide a complete view of early galaxy populations.

The locations for the JADES survey were chosen based on the availability of deep legacy multi-wavelength imaging and spectroscopy. For this reason the GOODS-South and GOODS-North fields (GOODS: The Great Observatories Origins Deep Survey, Giavalisco et al. 2004), which were deeply observed over the past 25 years were chosen. GOODS-South, which includes the Chandra Deep Field South and the Hubble Ultra Deep Field, along with deep ALMA and JVLA data, is the best deep field in the sky. It was chosen as the primary field for JADES, receiving the most observing time. GOODS-North, which includes the Hubble Deep Field and deep Chandra data, was selected as the secondary field. Two different fields were chosen to ensure the reliability and robustness of the survey results: the large angular separation between them also ensures that any unusual result is not due to peculiarities in one specific area.

Thanks to the near-infrared capability of the NIRSpec instrument, we have the unique ability to measure the rest-frame optical strong lines to very high redshifts $z \sim 10$ (e.g. [O II], H β , [O III], and even H α at $z < 7$). JADES provides calibrated 2D and 1D spectra of the target acquired.

The data used in this thesis come from the 3rd release of JADES (D'Eugenio et al. 2024). Since the goal of this thesis is to infer the star formation history, along with other physical properties, of galaxies, we used PRISM data from the JADES release. This data allows observing both the continuum and lines from rest-frame UV and optical wavelengths.

With the aim of studying the star formation histories of early galaxies, each galaxy in the release with redshift $z > 6$ has been selected. This criterion automatically rejects the galaxies for which the redshift was not provided, because it was impossible to measure with high confidence levels, by the JADES release.

A selection of the selected galaxies is visible in Figure 3.11. It is very unlikely for these galaxies to show a clear morphological shape. From the images is possible to see that JADES spectroscopy uses 5-shutter long slitlets.

3.5 Data selection

Not all galaxies available in the third release of JADES present a spectrum with a high signal-to-noise ratio. For this reason, a selection was performed on the galaxies and only those that presented at least one of the following criteria were kept for subsequent analysis:

- The signal-to-noise ratio at $\lambda_{\text{SNR}} = 200$ nm rest frame is $\text{SNR}(\lambda_{\text{SNR}}) \geq 3$. The choice for λ_{SNR} has two reasons: firstly it is a portion of the spectrum visible for each galaxy in the sample from redshift $z = 6$ to redshift $z = 13$. Furthermore, it is located in the part of the spectrum where the expected signal from the starlight is expected to be stronger (As you can see from Figure 2.3, considering that for galaxies at redshifts $z > 6$ the star formation history cannot be longer than $t_{\text{max}} \approx 700$ Myr and at wavelengths shorter than the Ly α the observed spectrum is deeply attenuated by neutral hydrogen clouds).

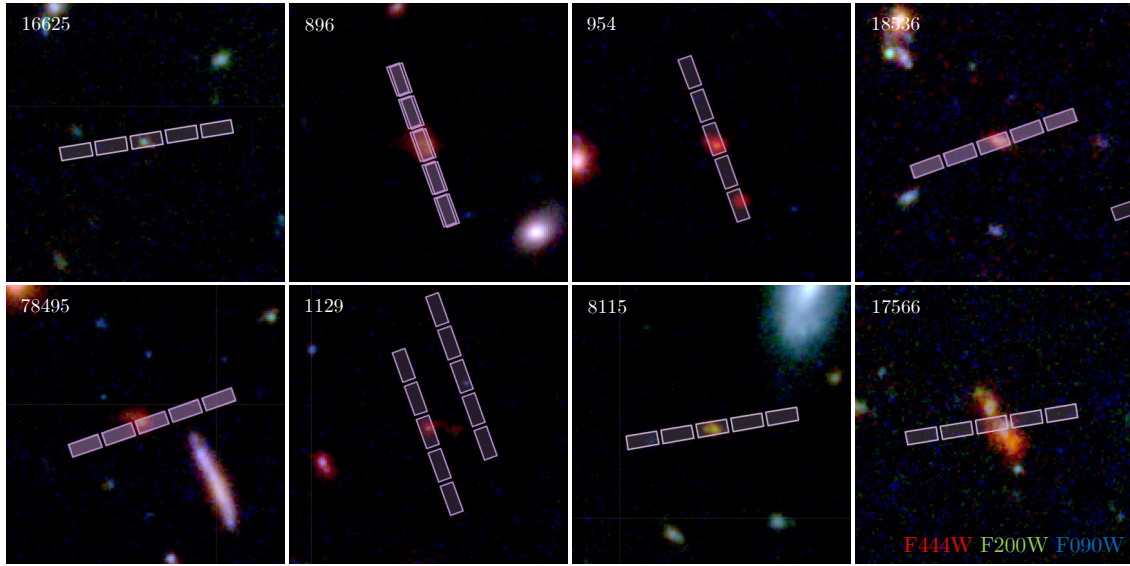


Figure 3.11: A subset of $z > 6$ galaxies from NIRCam with the MOS slitlets overimposed. The colors are generated from wide bandwidth filters F090W (centered at $0.9 \mu\text{m}$ for the blue channel), F200W (centered at $2.0 \mu\text{m}$ for the green channel) and F444W (centered at $4.4 \mu\text{m}$ for the red channel). The NIRSpec ID of these galaxies is written on the top left corner of each image.

The galaxy passes this selection if at least one of the forty nearest channels to λ_{SNR} has a $\text{SNR} > 3$.

- The spectrum near the $[\text{O III}]\lambda 5007$ line has a signal-to-noise ratio $\text{SNR}([\text{O III}]) \geq 7$. This second prescription has been used to keep a small number of galaxies with low UV slope but prominent lines. The galaxy passes this selection if at least one of the forty nearest channels to the $[\text{O III}]\lambda 5007$ line has a $\text{SNR} \geq 7$.

3.6 Resolving power

In Sec. 3.2 we have discussed that the NIRSpec PRISM has a resolution power R_0 which is wavelength-dependent and visible in Figure 3.5.

Although the provided resolving power in JWST User Documentation 2016 is relative to MOS shutters uniformly illuminated by a source of light, the analyzed galaxies, as you can see from Figure 3.11, generally do not completely fill the slitlet. On the other hand, the galaxies cannot be considered point sources either, meaning that the effective resolving power is galaxy-to-galaxy dependent and related to the morphological structure of the galaxy and its centering on the slit.

To resolve this issue, I calculated the resolving power using the spectra of all galaxies from JADES release number 2 (Eisenstein et al. 2023). The idea is to find a resolving power that, on average, better represents the spectral PSF of the galaxies at my disposal.

The newly obtained resolving power curve is denoted as $R_f(\lambda)$, to distinguish it from the official one, $R_0(\lambda)$ visible in Figure 3.5. The procedure to obtain $R_f(\lambda)$ is as follows:

- I performed a simultaneous fit of the lines [O III], H α , H β , and H γ using LMFIT⁴. An example of the result of this procedure is shown in Figure 3.12. The fitting prescriptions are:

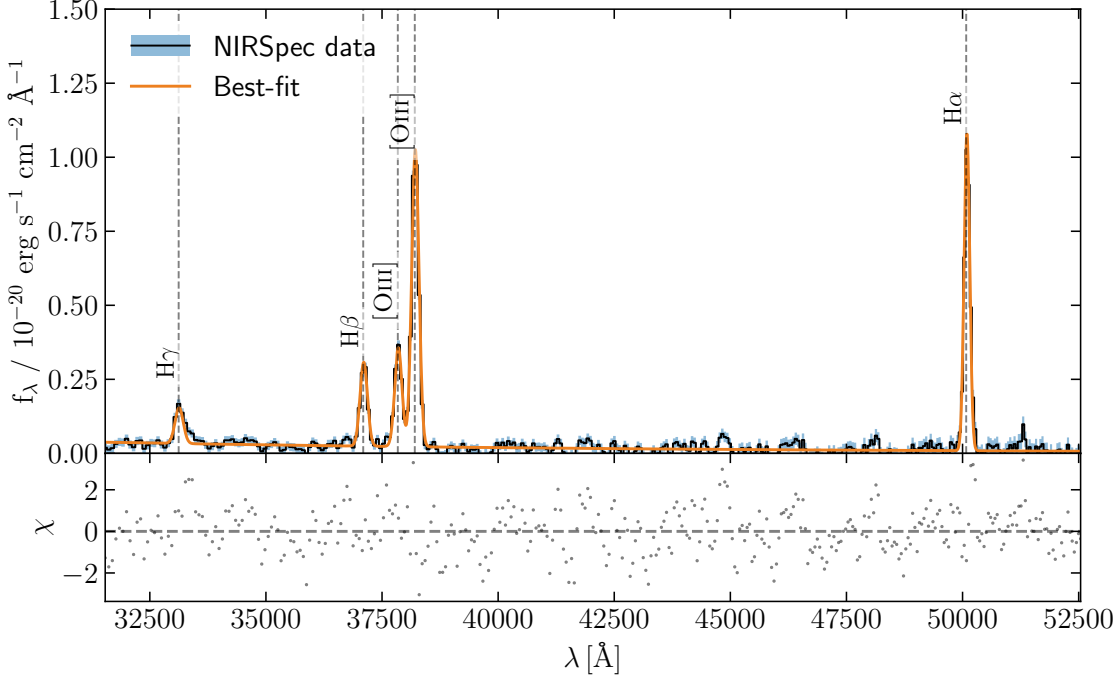


Figure 3.12: The result of the line fitting described in the text on a JADES galaxy (NIRSpec ID 16625).

- Each line is fitted with a Gaussian profile, the centroids are fixed one to the other using the rest-frame wavelengths of these lines. Still, the redshift is not fixed and is a free parameter in the fitting.
- The continuum in the rest-frame optical band (In this analysis the spectra are cropped from 400 to 700 nm, rest frame) is modeled with an exponential function.
- The standard deviations of each line are independent (except for the [O III] lines, see next item) but their initial values are set to be

$$\sigma_\lambda = k_\sigma \frac{\lambda}{R_0(\lambda)} \quad (3.4)$$

where $k_\sigma \approx 2.355$ is the ratio between the FWHM and the standard deviation of a Gaussian profile, while λ is the observed wavelength of the line.

- The standard deviation of the two lines of the [O III] doublet are linked one to the other by the R_0 resolving power ratio. Given the galaxy being at redshift z , than the observed wavelength of the [O III] $\lambda 5007$ line is

⁴<https://github.com/lmfit/lmfit-py>

$\lambda_{5007} = (1 + z)5007 \text{ \AA}$ and the second line of the doublet is observed at $\lambda_{4959} = (1 + z)4959 \text{ \AA}$. Being σ_{5007} the standard deviation of the strongest of the two oxygen lines than, using Eq. 3.3:

$$\sigma_{4959} = \frac{\lambda_{4959}}{R_0(\lambda_{4959})} \frac{R_0(\lambda_{5007})}{\lambda_{5007}} \sigma_{5007}$$

- The intensity ratio of the lines of the [O III] doublet is set to be $\frac{[\text{O III}]_{5007}}{[\text{O III}]_{4959}} = 2.98$ by statistical weights in the atom (Storey & Zeippen 2000).
- Only the fitted lines with an amplitude signal-to-noise ratio $\text{SNR} > 3$ are kept in the following analysis.
- I used the measured standard deviation σ of the [O III] lines and H α of every fitted spectrum to sample the resolving power of the NIRSpec prism $\sigma(\lambda)$.
- Being $R_0(\lambda)$ the aperture limited resolving power, I fitted the data $\sigma(\lambda)$ with the function $\sigma(\lambda) = k_\sigma \frac{\lambda}{R_f}$ where R_f is

$$R_f = mR_0 + a\lambda^2 + b\lambda + c \quad (3.5)$$

with a, b, c and m free parameters. Figure 3.13 shows the result of this fit.

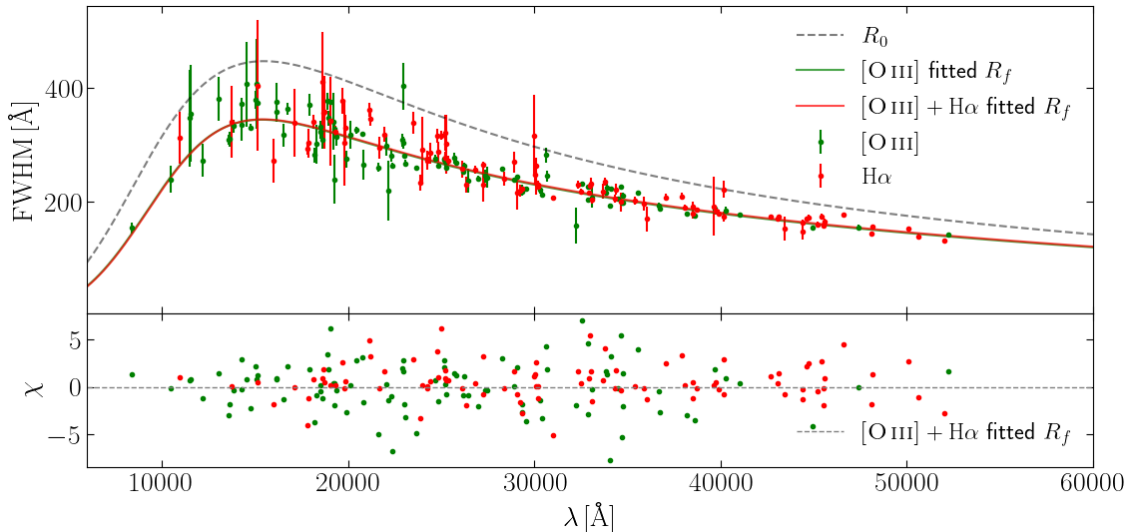


Figure 3.13: The fitted resolving power for the galaxies. The data contain [O III] $\lambda 5007$ (green markers) and H α (red markers) values extracted from line fitting for the galaxies in the second JADES release with the prescriptions described in the text. You can see that the result using only the oxygen line is almost coincident with the fit using both oxygen and hydrogen lines. The result is very different from the slit-limited R_0 curve (orange dashed line). The fit function is of the form $R = mR_0 + a\lambda^2 + b\lambda + c$. The bottom graph shows the normalized residuals. The scatter of the points is big ($\chi^2/\text{ndof} = 1044/188$) but this behavior was expected because the line widths depend on the morphology of the galaxy. The resolving power thus obtained is a function that on average describes the width of the lines of the observed galaxies much better than the limited slit R_0 . However, it may not be optimal on a case-by-case basis.

The difference between the use of the uniformly illuminated resolving power R_0 in comparison to the newly fitted resolving power R_f can be seen in Figure 3.14. The

two images show a SED fitting using BAGPIPES (which will be introduced in Sec. 4.1) with the same parameters but different resolving power. When using R_0 the H α and the [O III] lines are not fitted well with $\chi = \frac{\text{data} - \text{fit}}{\sigma}$ as high as 10 at the peak of these emission lines. The plot is limited to the H β and [O III] region for better visibility of the lines.

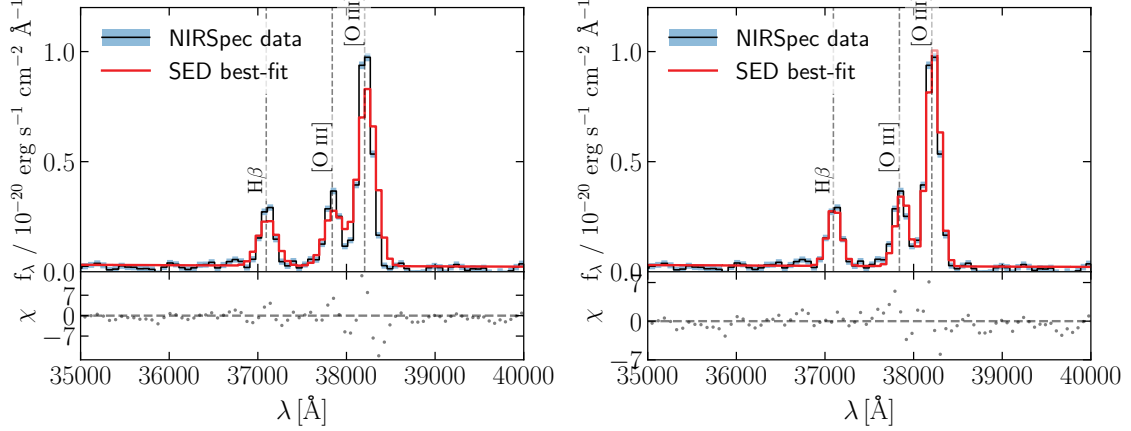


Figure 3.14: Comparison between the SED fitting with the official slit-limited resolving power R_0 (on the left) and the fitted resolving power R_f (on the right) of the JADES galaxy NIRSpec ID 16625. The difference is noticeable and improves the reliability of the physical parameters obtained from the emission lines by SED fitting (Sec. 4.1).

C H A P T E R



Data analysis

This thesis aims to study the physical properties and the star formation history of galaxies at redshift $z > 6$. For non-local galaxies it is impossible to directly study the light coming from single stars, instead, we can analyze the spectrum of the integrated light coming from the entire galaxy, or a portion of it.

When analyzing the light coming from an entire galaxy a SED fitting ([Walcher et al. 2011](#), [Conroy 2013](#)) can be performed. This methodology consists of comparing the observed SEDs (in this thesis NIRSpec spectrophotometric measures) of the observed galaxies to existing galactic templates based on various models (stellar population models, dust models, nebular emission, etc.) to ultimately estimate the physical properties of such galaxies. Indeed, every physical process occurring in the galaxy has its signature visible on the spectrum. After having modeled the effects of each process involved in recreating the observed spectrum, the free parameters of the fitting are tuned to obtain the best fit. In SED fitting, like any other fit, some parameters are fixed by the physics, while others are left as free parameters and returned by the fit. Among the others, one of the results a SED fitting can retrieve is the star formation history (SFH) of the observed object. The package used to perform SED fitting in this work is BAGPIPES.

This chapter presents an overview of the use I made of this tool with the data at my disposal (Sec. 4.1). Moreover, Sec. 4.1.5, Sec. 3.6 and Sec. 4.4 describe some improvements to the BAGPIPES code I have performed. Sec. 4.4.1, Sec. 4.5 describe other independent methods used for the data analysis and to validate the results of the SED fitting.

4.1 Bagpipes

BAGPIPES, which stands for ‘Bayesian Analysis of Galaxies for Physical Inference and Parameter EStimation’ is a state-of-the-art Python code for modeling galaxy spectra and fitting both spectroscopic and photometric observations with synthetic

spectral models (Carnall et al. 2018, 2019). In this thesis BAGPIPES has been used for modeling and fitting spectroscopy data to infer physical properties of the galaxies such as dust extinction, star formation history, ionization parameter and electronic density. In the next subsections the models and parameters used in BAGPIPES are described in detail, Table 4.1 shows the parameters used in SED fitting.

Parameter	Quantity	Prior ^(a)	Relevant sections
Redshift z	varied	Gaussian prior $z \sim \mathcal{N}(\mu, \sigma)$ centered on JADES redshift $z_{\text{spec}}^{(b)}$ $\mu = z_{\text{spec}}, \sigma = 0.02$	
Initial mass function	fixed	Kroupa 2001	Sec. 4.1.1
Stellar population	fixed	BPASS	Sec. 4.1.1
Metallicity Z	varied	$[0.02; 0.5] \text{ Z}_{\odot}$	Sec. 4.3.1
Nebular emission			
Ionization parameter $\log \mathcal{U}$	varied	$[-3.5; 0.5]$	Sec. 4.1.3
Electronic density n_e	fixed	100 cm^{-3}	
	varied	Log prior $[10^2; 10^5] \text{ cm}^{-3}$	Sec. 4.4 Sec. 4.4.1
Dust extinction A_V	varied	Calzetti et al. 2000 Log prior $[10^{-3}; 2]$	Sec. 4.1.2 Sec. 4.5
Step-like SFH			
Bin edges	fixed	Smallest bin 5 Myr Star formation begins at $z = 20$	
Bin's SFR	varying	Log prior $[5 \times 10^{-5}, 400] \text{ M}_{\odot}/\text{yr}$	Sec. 4.1.4
Mass formed	inferred	From the integral of the SFH	
Growing exponential SFH^(c)			
SFH starting time	fixed	$z = 20$	
Characteristic time τ	varied	log prior $[0.5 \text{ Myr}, 0.6 \text{ Gyr}]$	Sec. 5.2.3
Mass formed	varied	log prior $[10^5; 10^{10}] \text{ M}_{\odot}/\text{yr}$	
Age of birth clouds ^(d) t_{bc}	fixed	0.01 Gyr	
Resolving power $R(\lambda)$	fixed	Measured resolving power	Sec. 3.6

^(a) Uniform distribution if not differently specified ^(b) Redshift provided by the JADES release analyzing the galaxy NIRSpec/PRISM spectrum ^(c) Used as an alternative to the step SFH ^(d) Stars older than t_{bc} are assumed to not be inside a gas cloud and nebular emission is not produced.

Table 4.1: The parameters used in this thesis for the SED fitting with BAGPIPES

4.1.1 Stellar population models

One of the fundamental light sources in SED fitting is the starlight. Modeling the starlight involves simulating the light emitted by stars in various evolutionary stages, accounting for factors such as ages, and metallicities. Stellar population models combine the physics of stellar interiors and atmospheres to provide the Spectral

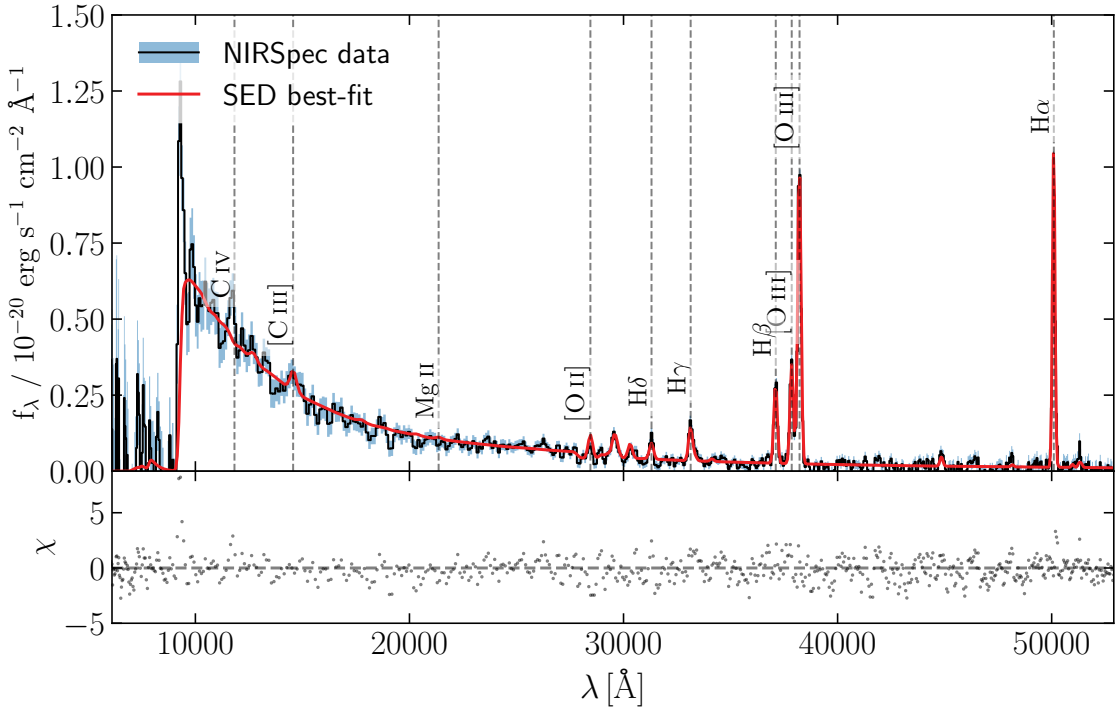


Figure 4.1: Example of a SED fitting from bagpipes of a JADES galaxy (NIRSpec ID 16625) at redshift $z = 6.6$. The x -axis reports the observed wavelength. In black the spectrum observed, in red the fitted one. The light blue shaded region is the 1σ uncertainty on the observed spectrum. The strongest emission lines are labeled. The fitted spectrum uses models to reproduce the observed one. In the next sections, the chosen models are described.

Energy Distribution (SED) of model galaxies as a function of physical parameters, e.g. time, star formation and metallicity.

To model the starlight from a galaxy, the starting point is the simple stellar population modeling, which describes the evolution in time of the SED of a single, coeval stellar population at a single metallicity. Three ingredients are necessary to build the SED of a single stellar population: stellar evolution theory, stellar spectral libraries, and an initial mass function (IMF).

Stellar population models aim to generate the wavelength-dependent luminosity per unit stellar mass of stars of a coeval stellar population $l_\lambda^{\text{ssp}}(\tau)$:

$$l_\lambda^{\text{ssp}}(\tau) = \int dm \mathcal{L}_\lambda(m, \tau) \frac{\phi(m)}{M_\odot} \quad (4.1)$$

where $\phi(m)$ is the IMF and $\mathcal{L}_\lambda(m, \tau)$ is the stellar spectrum of a star of mass m and age τ . The integral is computed over stellar masses.

By default, BAGPIPES uses the stellar population models from [Bruzual & Charlot 2003](#) (BC03). However, during some preliminary tests with JADES data, we observed that many galaxies exhibited strong $[\text{O III}]\lambda\lambda 5007, 4959$ emission lines which were not well-fitted by BAGPIPES (Figure 4.9). In other cases, these lines were fitted only if the galaxy was assumed to have extreme physical characteristics, a behavior

that will be detailed in Sec. 4.3. To investigate whether more up-to-date stellar population models could better explain these intense lines, and to ensure our study was as contemporary as possible, we decided to utilize the BPASS stellar population models (Byrne et al. 2022, Eldridge et al. 2017b, Stanway & Eldridge 2018).

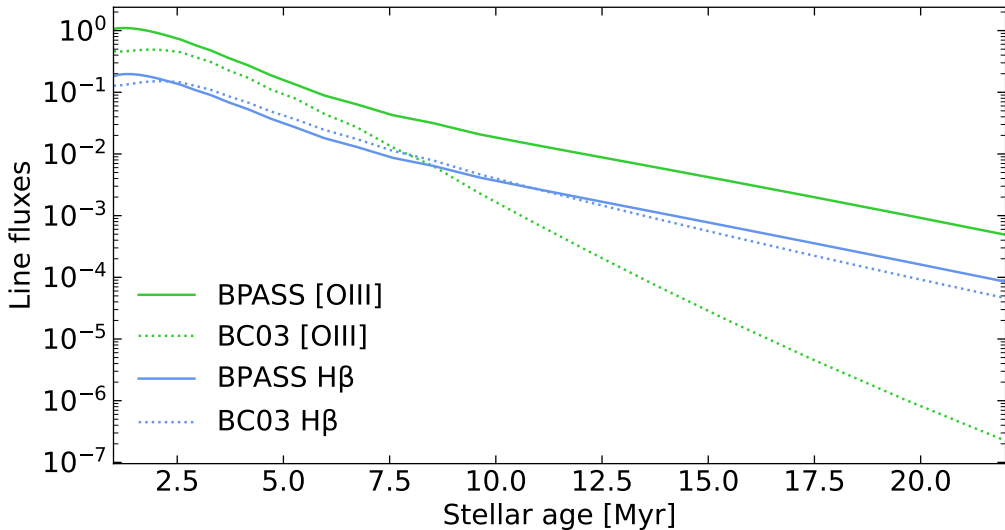


Figure 4.2: The [O III] and H β fluxes for a simple stellar population as a function of time. Comparison between BC03 and BPASS model for metallicity $Z = 0.1Z_{\odot}$, ionization parameter $\log \mathcal{U} = -0.5$ and electronic density $n_e = 100 \text{ cm}^{-3}$. The fluxes are normalized to the BPASS [O III] flux emitted by a stellar population 1 Myr old. The inclusion of stellar binary populations allows stronger and longer in-time [O III] emission.

The BPASS stellar models were built with a focus on best reproducing the emission from young and massive stars that are dominant in many galaxies we have. The most important feature of BPASS is the inclusion of binary stars' evolution in modeling the stellar populations. The general effect of binaries is to cause a population of stars to look bluer at an older age than predicted by single-star models. Moreover, detailed stellar evolution models are used rather than an approximate rapid population synthesis method. One key aspect of the BPASS models is that the emission from 10 Myr old populations is more than ten times stronger compared to the BC03 models. This suggests that these populations of binary stars can excite the lines of doubly ionized oxygen more strongly and further back in time (Figure 4.2).

Unfortunately, BPASS is not enough to explain the observed strong emission lines. Additional information about this issue will be discussed in Sec. 4.3.

For further studies, it would be of interest to use even more updated models that could account for other processes not treated in BPASS such as the X-ray binaries (e.g. Lecroq et al. 2024)

Initial mass function As we have discussed in Sec. 2.2.2 one of the proposed theories to explain the UV luminosity function problem and the high UV slopes of the ultra-early galaxies is an evolving initial mass function. But, in this thesis, this possibility is not explored. In each analysis, the initial mass function is assumed to be the one of Kroupa 2001.

4.1.2 Dust extinction

In Sec. 2.1.2 we have seen the role of the dust on the UV slope of the spectra.

The dust extinguishes the light coming from the galaxy and re-emits it in the far-infrared rest-frame wavelengths. The dust emission for galaxies at redshifts $z > 6$ is negligible at the NIRSpec wavelengths.

In this work, the dust is described by the [Calzetti et al. 2000](#) (Sec. 1.10) model which is a model based on starbursting galaxies in the local Universe and which is seen to be a good model for dust in high redshift galaxies ([Scoville et al. 2015](#)).

4.1.3 Nebular emission

The nebular emission (continuum and lines) are computed using the software **CLOUDY C23** ([Chatzikos et al. 2023](#)) which is a spectral synthesis code for astrophysical plasmas. CLOUDY computes the nebular continuum and lines emission using radiative transfer in a gas structure of fixed geometry. To model H II¹ emission in BAGPIPES the radiative transfer computation is done with a spherical shell geometry of fixed inner radius $R_i = 10^{19}$ cm and assume that the nebular emission from a galaxy is the sum of emission from H II regions of different ages, as in [Charlot & Longhetti 2001](#). The emission source is located in the center of this spherical shell and the input spectrum is the starlight emission computed in Sec. 4.1.1. The geometry used is visible in Figure 4.3. The metallicity of the ionized gas is assumed to be the same as the stars that produce the ionizing photons. We use the solar abundances of [Anders & Grevesse 1989](#).

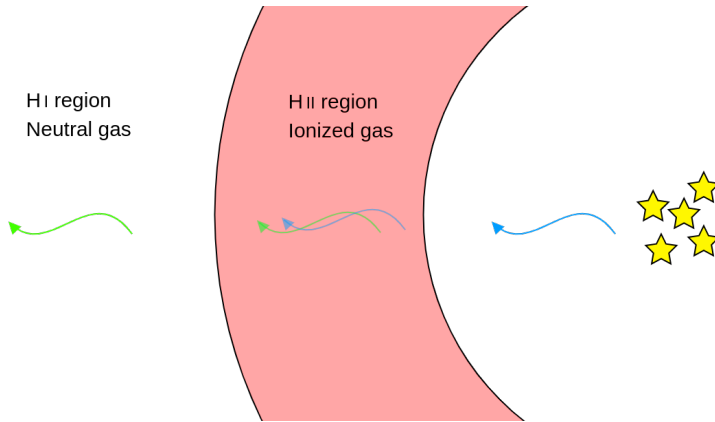


Figure 4.3: The geometry used in CLOUDY by BAGPIPES to model nebular continuum and lines. The galactic emission is located in the center of a spherical shell of inner radius $R_i = 10^{19}$ cm and inner electronic density $n_e = 100 \text{ cm}^{-3}$. The radiative transfer computes the existing spectrum. The shape of the region is in between a spherical and a plane parallel geometry.

BAGPIPES uses the logarithm of the ionization parameter $\log \mathcal{U}$ as the parameter to

¹H II regions are regions where hydrogen is mainly ionized around massive stars which emit ionizing photons.

fit the nebular emission. The ionization parameter is defined as follows:

$$\mathcal{U} = \frac{\dot{N}_\gamma}{4\pi R_i^2 n_e} = \frac{n_{\gamma,i}}{n_e} \quad (4.2)$$

where \dot{N}_γ is the number of ionizing photons emitted by the central source per second, n_e is the electron density, and $n_{\gamma,i}$ is the ionizing photons density at the inner radius of the modeled H II region.

By default, BAGPIPES sets the electron density to $n_e = 100 \text{ cm}^{-3}$ which is a good value for local galaxies, however, the possibility to relax this constrain is explored in Sec. 4.4.

The default grids provided with BAGPIPES have been recomputed using BPASS stellar models (Sec. 4.1.1) and with a larger range of ionizing parameters:

$$-4 \leq \log \mathcal{U} < 0.5$$

High values of the ionizing parameter are required when fitting galaxies at high redshift as the ones we have. To estimate the strength of nebular emission, the code computes the stellar emission at wavelengths shorter than the Lyman break². From that, it computes the total ionizing energy and redistributes it in the nebular emission.

4.1.4 Star formation history shapes

The star formation history (SFH) describes the rate at which a galaxy forms stars over time. Various shapes are commonly assumed for SFHs. BAGPIPES offers some pre-built star formation history (SFH) shapes, which include:

- Constant SFH, where the star formation rate remains unchanged over time starting from the time t_0 :

$$\text{SFR}(t > t_0) = \text{SFR}(t_0)$$

- Exponentially declining SFH, where the rate decreases exponentially with a time constant τ starting from an initial time t_0 :

$$\text{SFR}(t > t_0) \propto e^{-(t-t_0)/\tau}$$

- Delayed SFH, where the star formation rate rises to a peak and then declines exponentially:

$$\text{SFR}(t > t_0) \propto (t - t_0)e^{-(t-t_0)/\tau}$$

- Burst of star formation, where the totality of the stars were born at a time t_m

$$\text{SFR}(t) \propto \delta(t - t_m)$$

²The Lyman break at 911.8 nm is the wavelength threshold for radiation to ionize hydrogen (13.6 eV)

- A non-parametric SFH, called ‘continuity’(Figure 4.4), which follows the results from [Leja et al. 2019](#) for which the SFH is a step function with fixed edges:

$$\text{SFR}(t) = \sum_{i=0}^N \text{SFR}_i \chi_i(t)$$

where N is the number of bins, SFR_i is the star formation rate of the i -th bin and χ_i is the indicator function of that bin.

The star formation history shape is fundamental in reproducing the observed spectra from the galaxy: the stellar population models (Sec. 4.1.1) provide the luminosity density $l_\lambda(t)$ for a simple stellar population of age t per unit mass. Therefore, the total luminosity density L_λ of the galaxy is:

$$L_\lambda = \int_0^{t_{20}} d\tau \text{SFR}(\tau) l_\lambda^{\text{ssp}}(\tau) \quad (4.3)$$

where $t = 0$ is the galaxy time while t_{20} is the age relative to the time of the galaxy when the redshift was $z = 20$. $l_\lambda^{\text{ssp}}(\tau)$ is the spectrum of a simple stellar population of age τ per unit mass defined in Eq. 4.1. In this thesis, the SFHs are always cropped at redshift higher than $z = 20$.

One of the goals of this thesis is to see if there is any evidence about a very bursty star formation and more than one population of stars. To have the possibility to see such features in the star formation history of the analyzed galaxies, we have to use a model with a lot of freedom. The non-parametric SFH provided by BAGPIPES, called ‘continuity’ (Figure 4.4), which follows the results from [Leja et al. 2019](#), is the shape more similar to what we need, but it is not a good choice. in fact, this model has been proposed for low redshift galaxies where the SFH is expected to be an almost smooth function over time. The parameters of this model are:

- The stellar mass of the galaxy
- The ratios of star formation between adjacent bins. The bin edges are fixed by the users and, in the original prescription by Leja, the logarithm of the ratios between the star formation rate of adjacent bins have a student-t prior distribution that increases the posterior of smooth SFHs.

To allow for bursty SFHs I have seen that it not not enough to use a wider prior on the ratio between adjacent bins. Sec. 4.1.5 shows some examples of this behavior. For this reason, I included a new model in BAGPIPES, which I called ‘step’. This new shape of star formation requires the user to choose the bin edges (as it happens for the ‘continuity’ model) while the parameters are directly the star formation rates of each bin. Note that in this model the total mass of the galaxy is a derived quantity.

Bin edges Both the ‘continuity’ and the ‘step’ model of SFH, require the user to choose the edges of each bin of star formation.

The choice is particularly delicate, as fixing different bins can highlight different characteristics in the resulting star formation history. The option selected here is

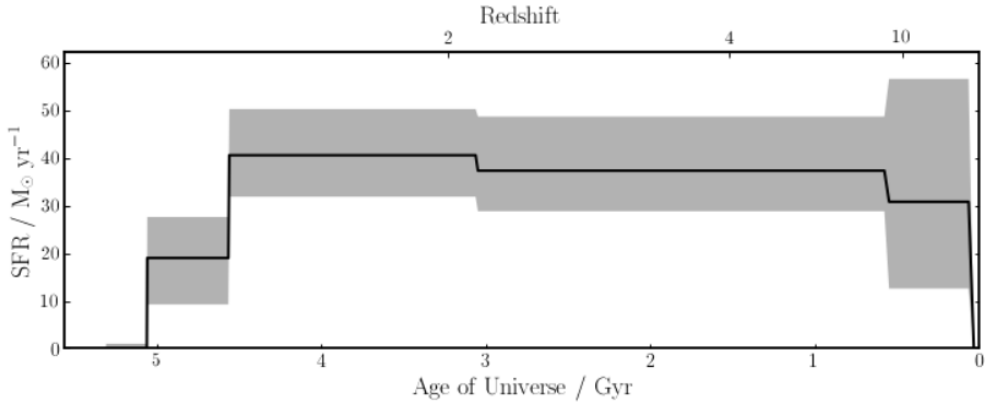


Figure 4.4: Example of SFHs extracted from a galaxy at redshift $z \approx 1$ using Leja's model. In black is the SFH, and in gray is the uncertainty. Credits: Carnall et al. 2019

the following: first of all, we selected a minimum time interval that to consider reliable. In this thesis 5 Myr is chosen, so each bin will never be shorter than this time interval.

The other bins are selected so that, in the case of a constant star formation rate over time, the contribution of each bin to the integrated flux observed by the NIRSpec PRISM is at least 1/3 of the contribution of the first bin. In this way, bins with the same SFR have similar flux contributions in the spectrum.

Figure 4.5 shows the integrated flux from $0.6 \mu\text{m}$ to $5.3 \mu\text{m}$ of a constant star formation history from the galaxy time to the stop time \tilde{t} for a galaxy at redshift $z = 6$.

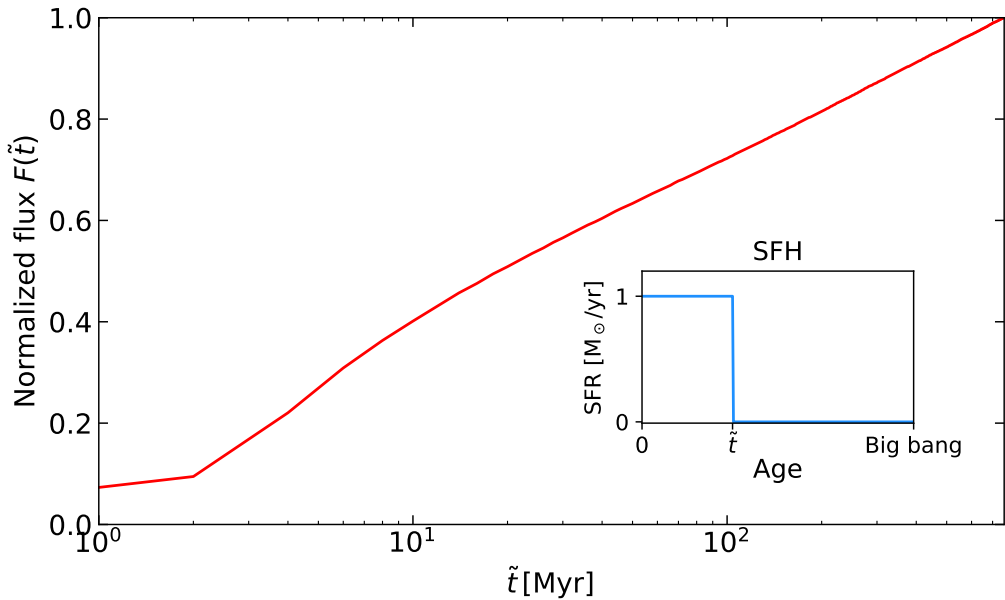


Figure 4.5: Normalized integrated flux in the NIRSpec PRISM wavelengths range of a galaxy at redshift $z = 6$ with a constant star formation rate from the galaxy time looking back to the time \tilde{t} (as it has been drawn in the small graph). The normalization is relative to the flux of a constant star formation history which begins at $z = 20$. Note that the x -axis is log-scaled. Indeed, old populations are exponentially dimmer than newer ones.

Given the monotonically increasing function $F(\tilde{t})$, as shown in Figure 4.5, computed at the galaxy's redshift and representing the integrated flux of a square-box star formation history normalized to the flux of constant star formation from redshift $z = 20$, the bin creation method proceeds as follows:

1. The first bin is always 5 Myr wide. This bin corresponds to a flux of $F_0 := F(5 \text{ Myr})$ from the function $F(\tilde{t})$.
2. The last bin ends at redshift $z = 20$, which corresponds to $F(\tilde{t}_{z=20}) = 1$. In this thesis, it is assumed that there is no star formation at higher redshifts.
3. The flux $1 - F_0$ must be equally distributed among all the bins except the first one, which is already set. Each subsequent bin should have a flux equal to one-third of the first bin ($\frac{1}{3}F_0$). Therefore, the interval $1 - F_0$ is divided into regions of size $\frac{1}{3}F_0$. The resulting N bin edges have fluxes $\{F_i\}_{i \leq N}$.
4. The ages $\{t_i\}_{i \leq N}$ of the bin edges are then computed using the numerically inverted function $\tilde{t}(F)$:

$$t_i = \tilde{t}(F_i)$$

In this way, the bins are larger at greater ages, but the flux of each bin is the same (except for the first one).

5. Any bins smaller than 5 Myr are merged together until each bin is larger than 5 Myr.

The result for a galaxy at redshift $z = 6$ can be seen in Figure 4.6. The first bins are shorter, while at greater ages they are longer. The luminosity of older populations is, in fact, much lower than newborn populations and the expected age sensitivity is lower.

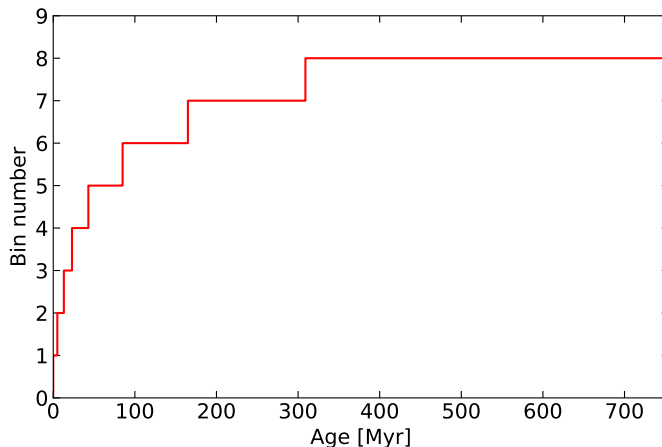


Figure 4.6: The bins created using the prescriptions of the text for a galaxy at redshift $z = 6$. These are the bins used in this thesis when fitting with ‘continuity’ and ‘step’ star formation history models.

4.1.5 Fitting bursty star

Correctly fitting a bursty star formation history is essential for understanding the history of high-redshift galaxies, where such burstiness is expected to be significant. In this section, I show a set of mock observations that are generated and fitted with both ‘continuity’ and ‘step’ functions. This is the procedure followed to perform the test:

- Mock observations of a galaxy at redshift $z = 7$ are generated with two stellar populations with different ages: the SFH modeled have a constant star formation rate of $10 \text{ M}_\odot/\text{yr}$ in the last 5 Myr and a second instant of star formation 20 to 40 Myr in the past. The youngest population has a mass $M_1 = 10 \text{ M}_\odot/\text{yr} \cdot 5 \text{ Myr} = 5 \times 10^7 \text{ M}_\odot$. Various mock observations are generated varying the mass of the older population M_2 .
- The mock observations try to reproduce as closely as possible a NIRSpec prism observation both in terms of the wavelengths observed and the resolving power and sensitivity of the instrument. All observations were produced by simulating an observation time of 10 000 s.
- The bin edges of the ‘step’ and ‘continuity’ fitting models are the same and are the ones built with the specifications described in Sec. 4.1.4.
- Each variable of the fit is fixed with those used to generate the model, except for what concerns star formation. For the ‘step’ model each star formation bin has a logarithmic prior with minimum at $10^{-5} \text{ M}_\odot/\text{yr}$ and maximum at $40 \text{ M}_\odot/\text{yr}$. Instead, as regards the ‘continuity’ model, the logarithm of the ratios of the star formation rate of adjacent bins have a uniform prior from -6 to 6 and the total mass of the galaxy has a logarithmic prior from 10^7 M_\odot to $10^{9.5} \text{ M}_\odot$.

The results, illustrated in Figure 4.7, clearly show the difficulty of the continuity model in correctly fitting a bimodal star formation history. The resulting star formation history is often a continuous function, except in the third test where a very old stellar population is fitted. In contrast, the ‘step’ model, which is compared to the continuity model, more accurately represents the burstiness of star formation. We emphasize that the 1σ uncertainty on adjacent bins in the fitted SFH is often strongly anti-correlated. This indicates that while the total mass of the galaxy is generally well-determined by the fit, the individual star formation rates of each bin are less certain.

4.2 Fine adjustments to the resolving power

The measured resolving power of the MOS instrument (Sec. 3.6) is object-to-object dependent because of the size and morphology of the galaxies. The fitted resolving power (Figure 3.13) is good enough for most of the galaxies to be well fitted and it is the way all the objects are fitted in this thesis.

Still, if a detailed analysis would be required for some galaxies it could be useful to

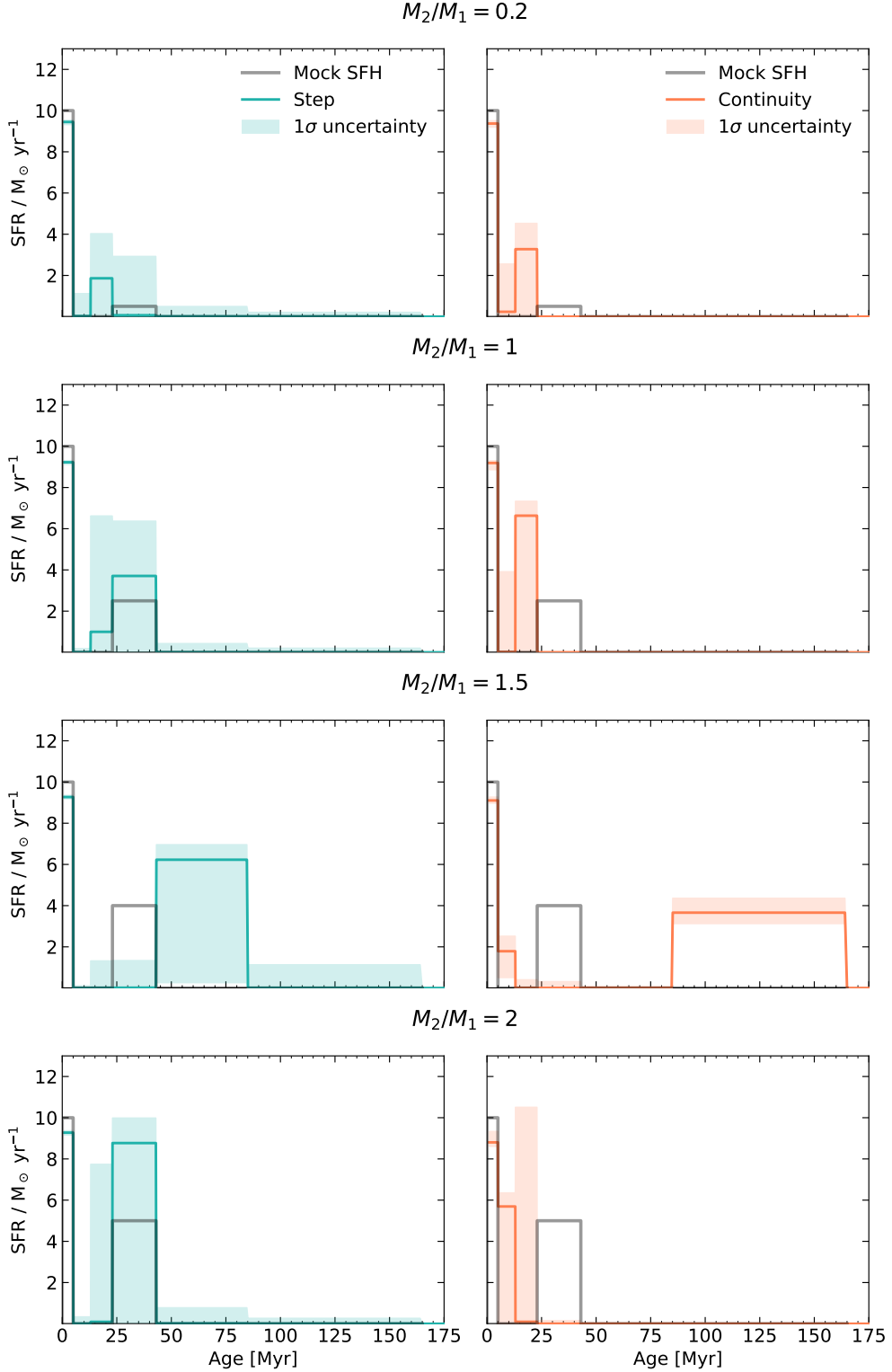


Figure 4.7: Comparison between ‘step’ and ‘continuity’ fitting of a bursty star formation history. The details about the model and the fit can be found in the text. From top to bottom, the mass M_2 of the older population increases relative to the mass of the young population M_1 . You can see how the ‘continuity’ model often fails to reproduce the burstiness of the star formation. The fit often converges to a more continuous star formation history. For this reason, I do not use the ‘continuity’ model to fit the SFH of the JADES galaxy at high redshift where burstiness is expected.

properly adapt the resolving power to the one that better fit for that one.

For this reason, I introduced a new variable in the BAGPIPES code to allow a fine-tuning of the resolving power. This variable called ‘R_mult’ can tune the fitted resolving power R_f (Eq. 3.5) to the best fitting R' as follows:

$$R' = R_{\text{mult}} R_f \quad (4.4)$$

The reason for not always using this variable is that it can slow down a lot the

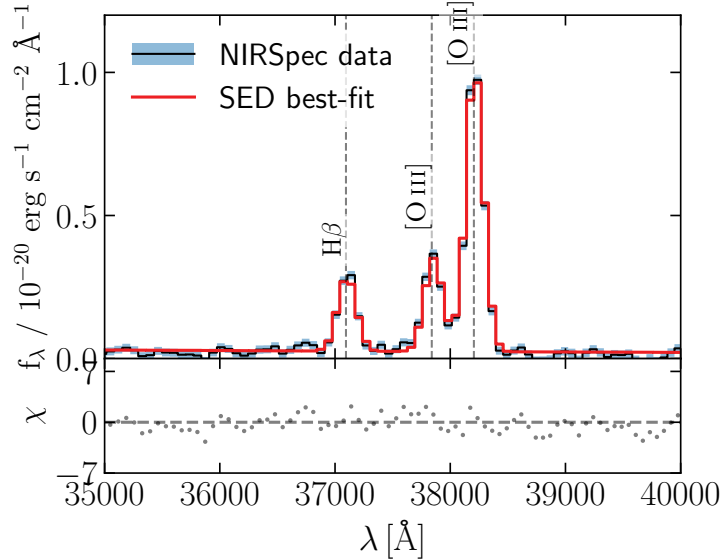


Figure 4.8: The same galaxy of Figure 3.14 fitted with ‘R_mult’ as a free parameter. The fit is very good in this case but the computational time increases too much to keep this free parameter in the fitting of the entire fitting. For this galaxy the fit reports $R_{\text{mult}} = 0.938^{+0.001}_{-0.001}$

convergence of the fit and it is necessary to carefully evaluate how important the perfect adaptation of the lines is with respect to the computational time.

4.3 Oxygen lines issue

The initial problem of fitting the emission lines of the NIRSpec spectra through SED fitting was addressed by both correcting the resolving power of the NIRSpec prism (Sec. 3.6) and using updated star models (Sec. 4.1.1).

However, some issues still arise in fitting the emission lines of certain galaxies with BAGPIPES. The main problems encountered are summarized as follows:

- A group of galaxies, comprising approximately 10% of the JADES 3rd release, present extreme values of specific star formation rate ($\text{sSFR} \gtrsim 500 \text{ Gyr}^{-1}$) and ionization parameters ($\log U \gtrsim -0.5$) when fitted with the [O III] lines. All these galaxies have a metallicity around one-tenth that of the Sun.
- When a SED fitting is performed on the spectra of these galaxies while masking the 500 nm oxygen doublet and keeping the same metallicity found with

the unmasked fit, the values of specific star formation rates and ionization parameters are less extreme.

- If the metallicity is also left as a free parameter and the oxygen lines are masked, the resulting metallicity is generally very low but the specific star formation rate is compatible with the fit with fixed metallicity.

Table 4.2 illustrates this behavior for the galaxy NIRSpec ID 4297, which is one of the galaxies exhibiting this pattern. The fit rules for the three fittings are the same except for what concerns the metallicity and the the [O III] masking.

Best-fit	$\log_{10} M [\text{M}_\odot]$	$Z [\text{Z}_\odot]$	sSFR [M_\odot/yr]	$\log \mathcal{U}$	A_V
Unmasked	$7.14^{+0.05}_{-0.04}$	$0.14^{+0.01}_{-0.01}$	$\gtrsim 1100^{(a)}$	$-0.37^{+0.18}_{-0.13}$	$0.20^{+0.05}_{-0.04}$
Masked fixed Z	$7.07^{+0.08}_{-0.06}$	$0.14^{(b)}$	190^{+70}_{-50}	$-1.22^{+0.15}_{-0.15}$	< 0.1
Masked free Z	$7.02^{+0.13}_{-0.08}$	$\lesssim 0.02^{(a)}$	170^{+130}_{-75}	$-(c)$	< 0.1

(a) The posterior is converging towards the edge of the prior (b) Fixed by the unmasked best-fit (c) Value unconstrained by the fitting

Table 4.2: The physical parameters of the galaxy NIRSpec ID 4297 when fitted with or without the [O III] LINES

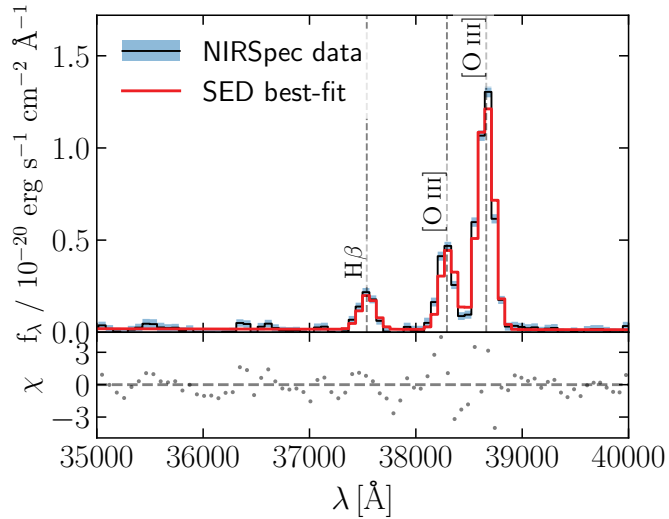


Figure 4.9: The oxygen line issue in this galaxy (JADES NIRSpec ID 4297 at redshift $z \approx 6.7$) arises because the double ionized oxygen lines are only fitted if extreme physical properties are assumed for the galaxy: $\text{sSFR} = 1100 \text{ Gyr}^{-1}$ and $\log \mathcal{U} = -0.3$. The metallicity is found to be 0.14 times the solar metallicity. The fit is performed using BPASS with an electron density of $n_e = 100 \text{ cm}^{-3}$

The huge difference in the fit results, if the double ionized oxygen lines are excluded, suggests that some physical process is not well described by the models used. This is why I called this phenomenon the ‘oxygen lines issue’. To try to find what caused these strong emission lines we used up-to-date stellar models (Sec. 4.1.1) and introduced the possibility of higher electron density (this topic will be described in Sec. 4.4). Both these changes improve a little bit the description of these lines but they are far from solving the issue.

For this reason in this thesis we decided to measure the star formation history of the galaxy by masking these lines (they are excluded from the spectra passed to BAGPIPES). The search for the physical reason why these lines cannot be described well will be the subject of a possible continuation of this thesis work.

The big problem that arises from cutting out these lines is the measure of the metallicity of the galaxy that is poorly determined without the [O III] lines³. To solve this issue I performed a first SED fitting of the entire catalog with a ‘step’ star formation history (Sec. 4.1.4) without cutting [O III] lines to obtain the metallicity of the galaxies which I will use in the new fits where the oxygen lines are cut. A statistical visualization of the metallicities obtained is visible in Figure 4.10.

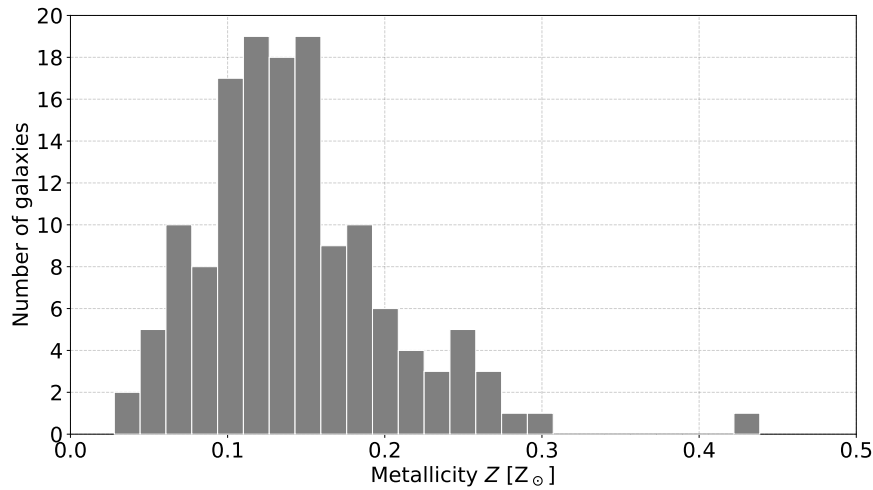


Figure 4.10: Metallicities (respect to solar metallicity) of the galaxies in the JADES third release with redshift $z > 6$ and high enough SNR. The exact date selection is described in Sec. 3.5

4.3.1 Reliability of metallicity measurements

Measuring the metallicity of galaxies is not the objective of this thesis. However, it is interesting to understand whether the measurements obtained can be truthful or not and in particular if the ‘[O III] issue’ could impact these values.

To answer this question I generated a plot of line strengths in function of metallicity and ionization parameter (Figure 4.11).

From the figures, it can be seen that the metallicity values obtained are those compatible with a small [S II] flux (about 10^{-2} the $H\alpha$ flux as on average in the analyzed galaxies showing these lines) and with the particularly intense doubly ionized oxygen lines. Moreover, strong [O III] lines mean extreme $\log \mathcal{U}$ values as I obtained, indeed.

If, as we said, these lines could hide some physical processes not well explained by the models we are using, we should also not fully trust the metallicity results obtained.

³The [S II] lines are dim due to low metallicity of these galaxies

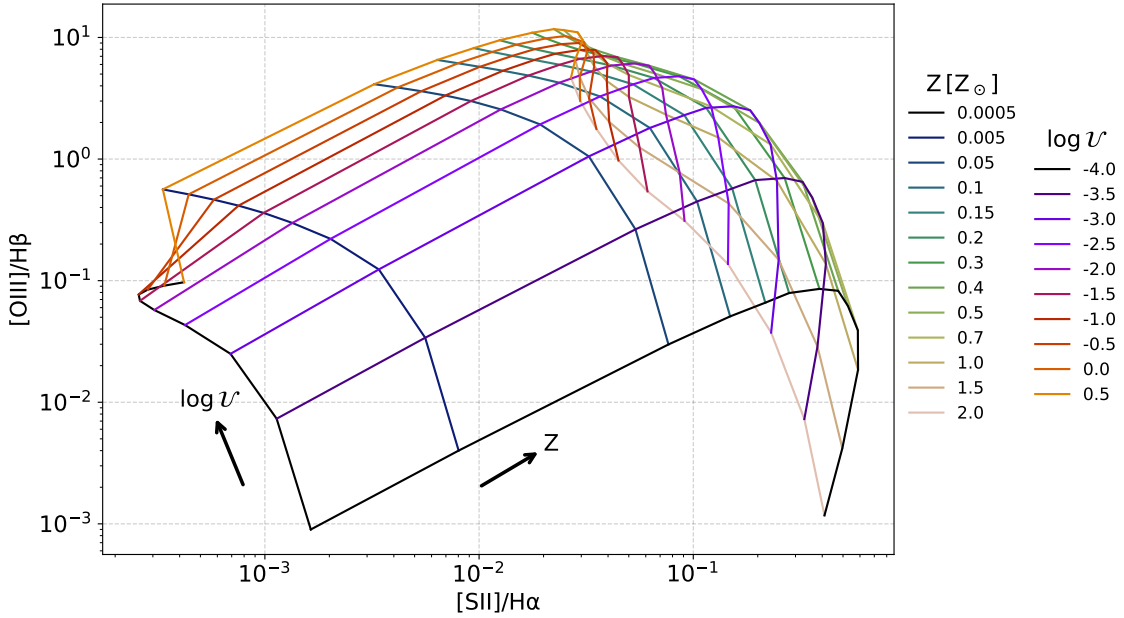


Figure 4.11: Ratio of [O III] over H β fluxes vs ratio of [S II] over H α as a function of metallicity Z and ionization parameter \mathcal{U} . The grid has been built with BPASS stellar models with a burst of age 2.5 Myr and CLOUDY (As described in Sec. 4.1.3). The part of the grid with small [S II] fluxes respect to H α ($\approx 10^{-2}$) and huge [O III] fluxes is located at very high ionization parameter and metallicity of the order $Z = 0.1 - 0.3Z_{\odot}$ which are exactly the results obtained for the majority of the galaxies (Figure 4.10)

In particular, assuming that in the observed galaxies if our models were realistic we would observe lines of less intense oxygen (as explained in Sec. 4.3), then we should expect that the observed metallicities are an overestimate of the real values (see Figure 4.11 again: with the same sulfur and hydrogen fluxes, lower oxygen fluxes would correspond to lower metallicities).

4.4 Electron density

By default, BAGPIPES has the nebular grids built with $n_e = 100 \text{ cm}^{-3}$ which is a good value for local H II regions. However, in high redshift galaxies, the ISM is more dense, probably because of the compactness of these objects (Arrabal Haro et al. 2023). Isobe et al. 2023 found, using the [O II] line ratio, that the electron densities of $z = 4 - 9$ galaxies are $n_e \gtrsim 300 \text{ cm}^{-3}$, while Senchyna et al. 2023, from the analysis of the line N IV] in the galaxy GN-z11 (redshift $z = 10.6$), obtained $n_e \gtrsim 10^5 \text{ cm}^{-3}$.

A different electron density will also modify the strength of the emission lines. To address the double ionized oxygen line issue (Sec. 4.3), I modified the BAGPIPES code and rebuilt the nebular grids to allow for a varying electron density. However, as we will see, this change does not solve the [O III] problem, for this reason, I want to emphasize that this change to the code is temporary, valid only for this section, and it will not be used later.

Fixing the same amount of ionizing radiation produced by the galaxy, higher electron densities mean higher nebular fluxes. An example can be seen in Figure 4.12. The result obtained with this improvement to the BAGPIPES code will certainly be

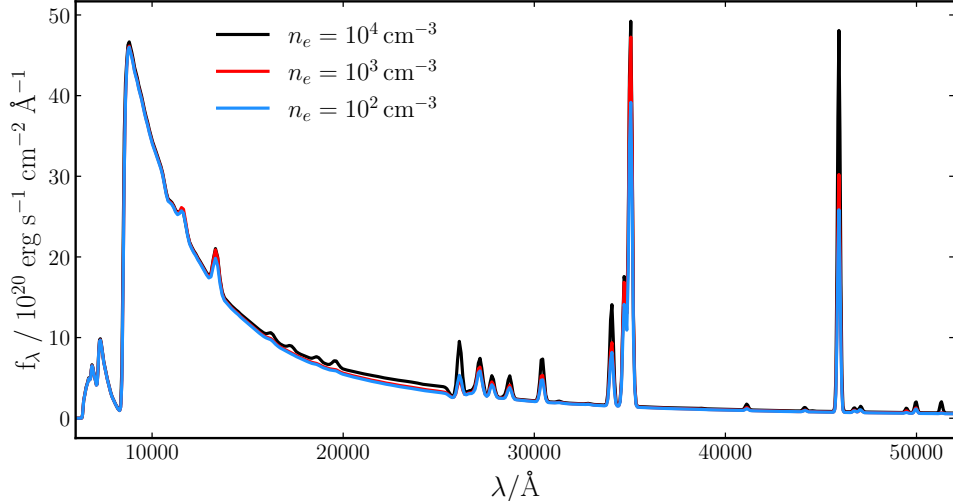


Figure 4.12: Mock spectrum of a dust-free galaxy at redshift $z = 6$ with a growing exponential SFH of characteristic time $\tau = 10$ Myr and mass $M = 10^9 M_\odot$ as a function of the electron density of H II regions. BPASS and CLOUDY as described in the chapter. $\log \mathcal{U}(n_e = 100 \text{ cm}^{-3}) = -0.5$. The radiation field is assumed to be constant in the three graphs so the ionization parameter decreases by 1 dex from 10^2 to 10^3 electrons per centimeter cubed and similarly from 10^3 to 10^4 .

useful on other occasions, managing to better model what happens at high redshift. However, in the objective of this thesis, this improvement did not obtain the desired results: if the electron density is a free parameter in the fit, without cutting out the [O III] lines, the fit (for a large number of galaxies) converges to the highest possible densities present in the grids I have made $n_e = 10^5 \text{ cm}^{-3}$. This is because, at such high density, the oxygen lines are more intense with all other variables being equal. Even if what is obtained could be evidence of particular dense H II regions, such high densities at redshift $z \approx 6$ are unlikely given what is obtained from direct [O II] lines measures at these redshifts (Isobe et al. 2023). It therefore seems that although the density parameter is fundamental, it is not yet sufficient to explain the very intense [O III] lines. As already said in Sec. 4.3 we will therefore proceed to exclude these lines from the fit.

4.4.1 Direct measurement of electron density

As it was impossible to obtain a true measurement of electron density from the SED fitting, we decided to directly measure this quantity from the ratio $[\text{O II}] \lambda 3729 / [\text{O II}] \lambda 3726$ analogously to what is done by (Isobe et al. 2023). Figure 4.13 shows the dependence of this ratio over the electron density. To compute this ratio on the JADES galaxies, medium-resolution spectroscopic data of the JADES galaxies from the G395M disperser have been used (Sec. 3.2).

Due to the low signal-to-noise ratio of these lines, a weighted average of all the

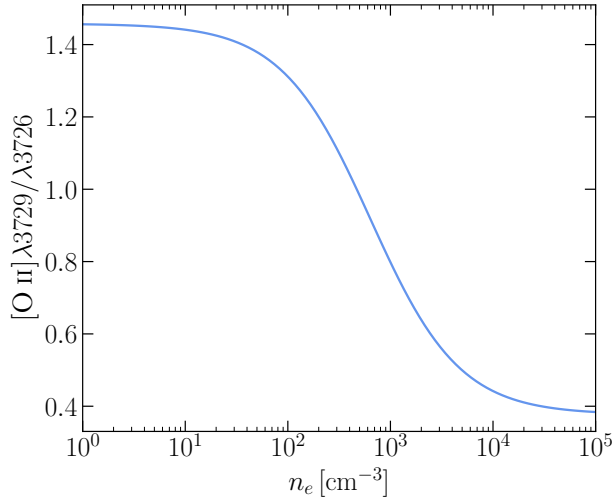


Figure 4.13: The ratio between the [O II] lines as a function of the electron density. Measuring this ratio can give us a constraint on the electron density of the H II regions of these galaxies. Credits: Sanders et al. 2016.

spectra at our disposal is performed. Only the galaxies that presented both the [O III] and [O II] lines in the medium resolution spectroscope are considered.

The average is performed in this way: for each spectrum the [O III] $\lambda 5007$ and $\lambda 4959$ lines are fitted simultaneously with two Gaussians, added to a constant for the continuum. Centroids, amplitude and widths are related between the two lines as described in Sec. 3.6. From this fit the redshift of the galaxy is measured. This step is crucial to perfectly match the wavelengths of the disperser and avoid any calibration discrepancy between different prism and gratings. At this point, the spectra corresponding to the [O II] lines are added together in the rest-frame wavelengths. The signal-to-noise ratios of the [O II] line are used as weights. To perform this weighting, a preliminary fit with a single Gaussian added to a constant is performed on the [O II] doublet to evaluate the intensity of the lines.

On the average of all the spectra, a fit is performed with a double Gaussian with the same width (plus a constant for the continuum). The centroids of the two lines are fixed by the wavelengths of the [O II] lines. In the entire procedure, high-precision wavelengths are used. The values come from the Atomic Line List v3⁴ (van Hoof 2018).

The result is visible in the Figure 4.14

The measured ratio between the two lines is

$$\frac{[\text{O II}]_{\lambda 3729}}{[\text{O II}]_{\lambda 3726}} = (1.1 \pm 0.1) \quad (4.5)$$

Using the values from Sanders et al. 2016 the electron density is

$$n_e = (3 \pm 1) \times 10^2 \text{ cm}^{-3} \quad (4.6)$$

which is compatible with the work of Isobe et al. 2023 at redshift $z \approx 6 - 7$

⁴<https://linelist.pa.uky.edu/newpage/>

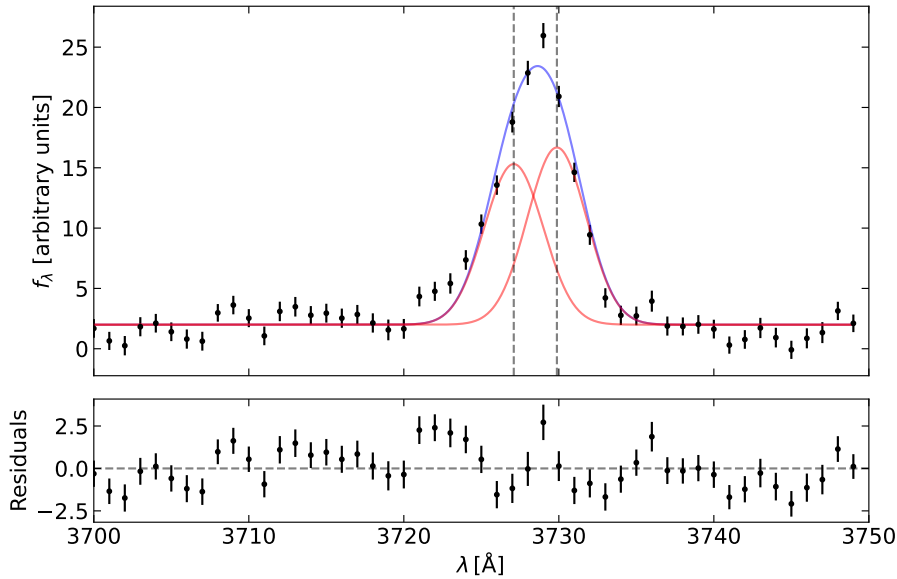


Figure 4.14: The fit of the [O II] doublet to measure the electron density of HII regions. In black the weighted average of the spectra (see text) in blue is the best fit and in red are the two Gaussian components. $\chi^2/\text{ndof} = 71/48$

4.5 Dust content and Balmer decrement

The amount of light absorbed by dust, in particular the parameter A_V , is one of the parameters of greatest interest for understanding how these first galaxies (Sec. 2.2.5) formed. Therefore, I decided to test the A_V results provided by the preliminary SED fitting (the one obtained without cutting the OIII lines) with an independent analysis method.

What I tried to do is to evaluate it using the Balmer decrement: by measuring the fluxes of the lines of the Balmer series and assuming that they are produced in an HII region it is possible to compare them with their theoretical ratios and from this I can compute the degree of dust absorption (always using a Calzetti law to model it). Indeed, the emission lines of the Balmer series are generated in the hydrogen recombination cascade, and their flux ratios are determined by statistical weights. If the ratio of these fluxes deviates from theoretical predictions, it is generally due to the presence of dust, which causes the extinction of the lines. In the fitting process, the intensity ratios between the hydrogen lines are adjusted for dust presence using the Calzetti law (Sec. 4.1.2). According to this law, the extinction parameters at the H α , H β and H γ wavelengths relative to the visual extinction A_V are (Calzetti et al. 2000):

$$\Gamma_\alpha := \frac{A_\alpha}{A_V} = 0.82 \pm 0.16 \quad (4.7)$$

$$\Gamma_\beta := \frac{A_\beta}{A_V} = 1.13 \pm 0.22 \quad (4.8)$$

$$\Gamma_\gamma := \frac{A_\gamma}{A_V} = 1.25 \pm 0.25 \quad (4.9)$$

I set the dust-free ratios of the Balmer lines to $R_{\alpha\beta} := \frac{H\alpha}{H\beta} = 2.86$ and $R_{\gamma\beta} := \frac{H\gamma}{H\beta} = 0.47$ which are values computed at temperature $T = 10\,000$ K and electron density $n_e = 100\text{ cm}^{-3}$, but they slowly vary with density (Dopita & Sutherland 2003). Using Eq. 1.71:

$$A_\beta - A_\alpha = -2.5 \log\left(\frac{f_{\text{obs};\beta}}{f_{\text{obs};\alpha}} R_{\alpha\beta}\right) \quad (4.10)$$

Using Eq. 4.7 e Eq. 4.8:

$$A_V = \frac{2.5}{\Gamma_\beta - \Gamma_\alpha} \log\left(\frac{f_{\text{obs};\beta}}{f_{\text{obs};\alpha}} R_{\alpha\beta}\right) \quad (4.11)$$

The equation holds similarly for $H\gamma$.

To obtain the line fluxes I performed a best-fit procedure of the spectra of the galaxies. The prescriptions used in the fitting are similar to the ones described in Sec. 3.6. However, to reduce the number of free parameters the line widths are set by the measured resolving power (Sec. 3.6) multiplied by a free parameter similar to the ‘R_mult’ coefficient described in Sec. 4.2.

The dust extinction in the visual band is then computed using Eq. 4.11. If $\frac{f_{\text{obs};\alpha}}{f_{\text{obs};\beta}} < R_{\alpha\beta}$, than A_V is set to zero.

The result, limited only to the galaxies in our sample for which the $H\alpha$ line was visible, i.e. to the galaxies at redshifts $6 < z < 7$, is shown in Figure 4.15. You can see there is a big scatter between the two measures. It is noticeable that a large group of galaxies, for which the dust absorption from SED fitting is nearly 0, present a huge dust absorption when measured through the Balmer decrement.

In comparing the dust extinction measured through the Balmer with the one from the SED fitting two factors are fundamental:

- The Balmer decrement analysis does not consider other emission and absorption lines not resolved in the spectrum. In particular:
 - The [N II] lines which increase the observed flux of the $H\alpha$ line.
 - The stellar atmosphere’s absorption lines which reduce the fluxes of both the hydrogen lines
- The dust extinction in the SED fitting case is not only determined by the emission but also by the continuum

For this reason, we aim to estimate the contribution of the [N II] lines and stellar atmosphere absorption lines in affecting the Balmer decrement procedure. This contribution has been estimated using the SED fitting results. The $[\text{N II}]\lambda\lambda 6548, 6583$ fluxes are a direct output of the best-fit SED from BAGPIPES, while the Balmer absorption lines are estimated through Gaussian fitting of the best-fit SED regenerated without the nebular component (Figure 4.16).

Let f_N denote the total flux of the Nitrogen lines, and $f_{\text{atm};\alpha}$ and $f_{\text{atm};\beta}$ represent the absolute value of the atmosphere’s absorption lines at the H_α and H_β wavelengths,

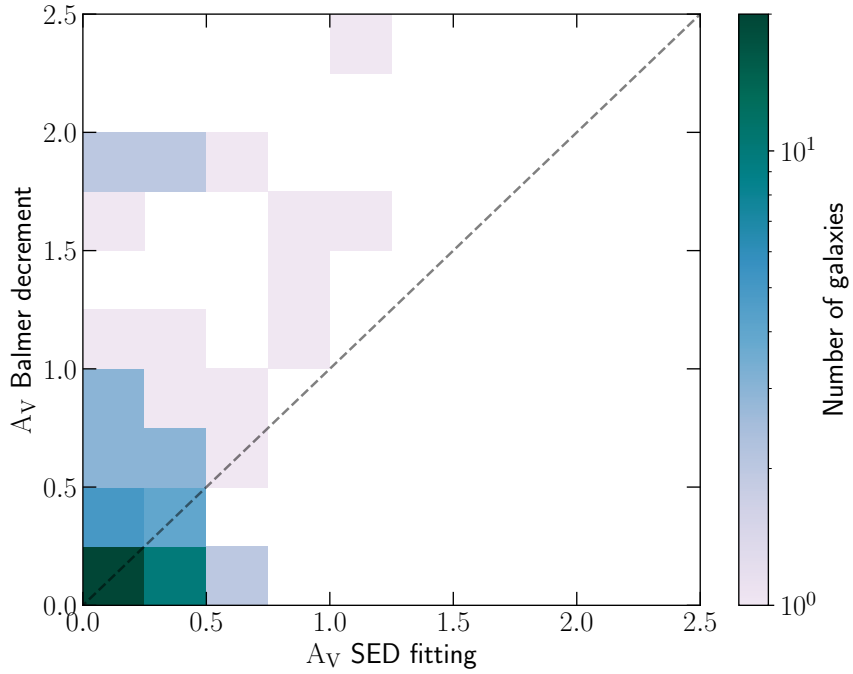


Figure 4.15: A_V comparison between the values from the SED fitting and the values obtained from the Balmer decrement procedure. The majority of the galaxies present a low dust absorption ($A_V < 0.5$). The dashed black line is the bisector of the quadrant.

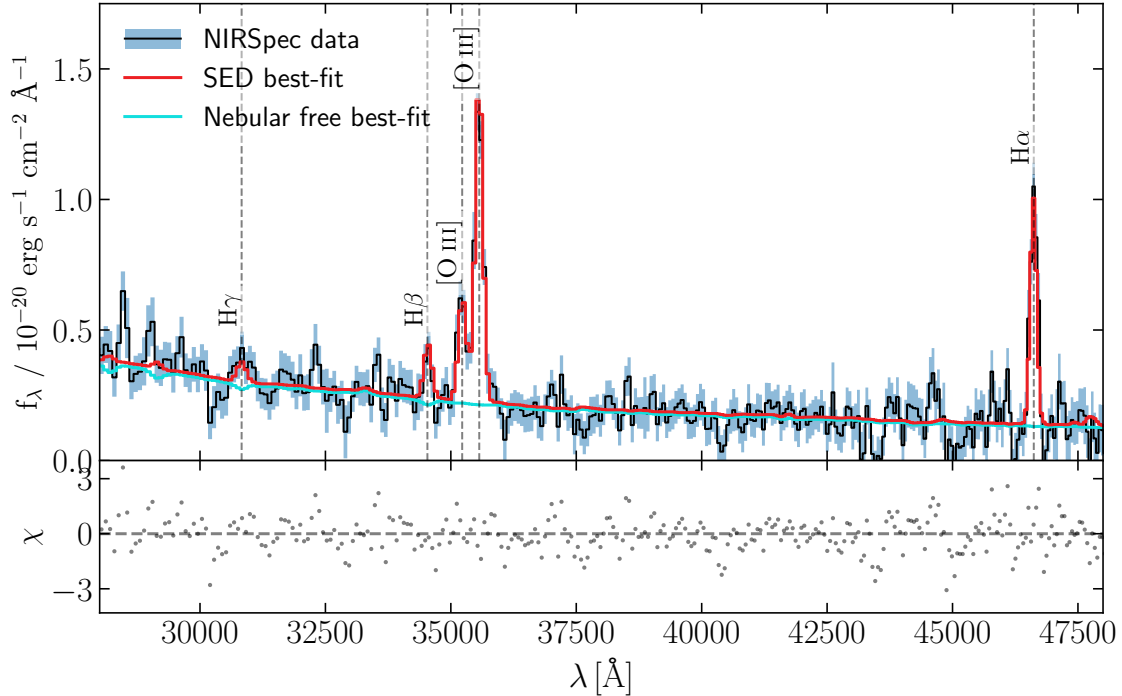


Figure 4.16: SED fitting of a JADES galaxy (NIRSpec ID = 9877) and the best-fit without the nebular emission. The stellar atmosphere's absorption lines are visible below the Blamer lines

respectively. The corrected ratio $R'_{\text{obs};\alpha\beta}$ between the observed emission fluxes of the Balmer emission lines is then given by:

$$R'_{\text{obs};\alpha\beta} = \frac{f_{\text{obs};\alpha} + f_{\text{atm};\alpha} - f_N}{f_{\text{obs};\beta} + f_{\text{atm};\beta}} \quad (4.12)$$

For the galaxies in the sample, I have computed these fluxes. In Table 4.3, the relative importance of these factors is presented over the entire sample of galaxies. The major contribution is the atmospheric absorption at the H β wavelength.

	$f_N/f_{\text{obs};\alpha}$	$f_{\text{atm};\alpha}/f_{\text{obs};\alpha}$	$f_{\text{atm};\beta}/f_{\text{obs};\beta}$
min	0.2%	0.05%	0.5%
mean	0.8%	0.4%	4.2%
max	1.8%	2.0%	17.8%

Table 4.3: The relative importance of the correcting factors to the Balmer decrement computation. minimum, mean, and maximum values are computed over the entire sample of galaxies for which the H α is visible and the SNR of this line is greater than 5

Figure 4.17 shows the updated A_V comparison between the values from the SED fitting and the values obtained from the Balmer decrement procedure corrected for the stellar atmospheres' absorption lines and N II fluxes. While Figure 4.18 shows the difference between the dust extinction A_V obtained with the corrected Balmer decrement and the SED fitting.

The correction (Eq. 4.12) improves without solving the scatter between the two quantities. Moreover, there is a series of points for which $A_{V;\text{SED}} > A_{V;\text{Balmer}}$ where the uncertainty associated with the difference between the dust extinctions is very small. To better quantify this result Table 4.4 shows the χ^2 of the difference $A_{V;\text{SED}} - A_{V;\text{Balmer}}$. Furthermore, two additional quantities are computed: the χ^2 values for the points for which $A_{V;\text{SED}}$ is greater or smaller than $A_{V;\text{Balmer}}$.

	χ^2	Number of galaxies
$A_{V;\text{SED}} \geq A_{V;\text{Balmer}}$	90	29
$A_{V;\text{SED}} < A_{V;\text{Balmer}}$	590	38
Total	680	67

Table 4.4: χ^2 of the difference $A_{V;\text{SED}} - A_{V;\text{Balmer}}$ also for the points for which $A_{V;\text{SED}}$ is greater (smaller) than $A_{V;\text{Balmer}}$

We can conclude that the stellar absorption lines are not sufficient to explain the scatter between the SED and the Balmer decrement measured extinctions. For galaxies that appear dustier according to the Balmer decrement, the most plausible explanation could be a disparity between the galactic extinction and the extinction at the sites of new star formation (the lines suffer attenuation due to the presence of the birth cloud dust). Even more interestingly, there is a large number of galaxies with less dusty lines than the stellar continuum and with little measurement uncertainty

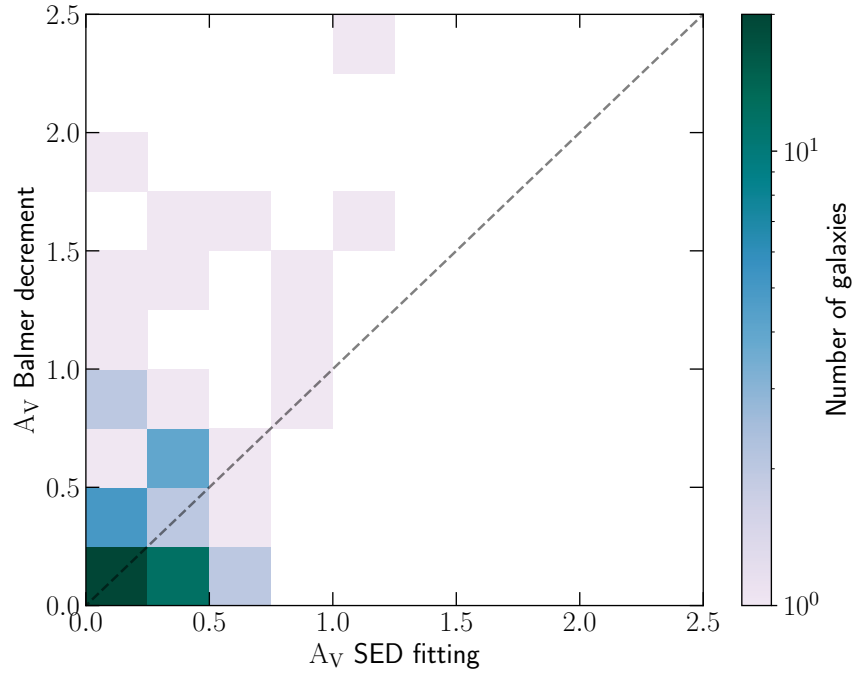


Figure 4.17: A_V comparison between the values from the SED fitting and the values obtained from the Balmer decrement procedure corrected for the stellar atmospheres' absorption lines and NII fluxes

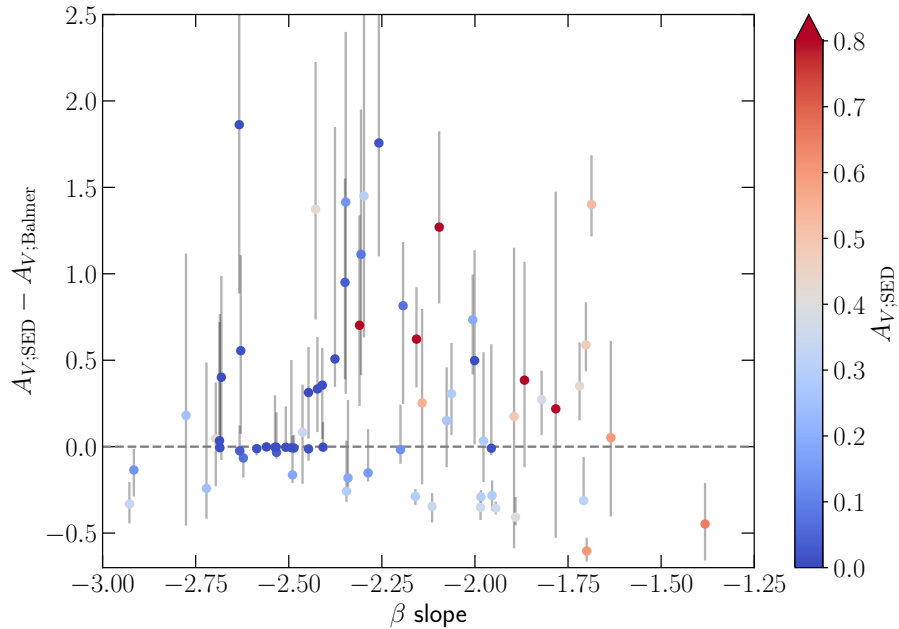


Figure 4.18: A_V difference between the values from the SED fitting and the values obtained from the Balmer decrement as a function of the measured UV β -slope of the galaxies, color-coded with the SED fitting A_V .

(the χ^2 is much greater than the number of galaxies for $A_{V;\text{SED}} < A_{V;\text{Balmer}}$). This indicates that the birth sites appear dust-free in a galaxy that is not, which is unusual and needs further investigation.

In conclusion, we must remember that the disparity between $A_{V;\text{SED}}$ and $A_{V;\text{Balmer}}$ is also visible in some galaxies where the hydrogen emission lines are not well fitted. This likely occurs because the best-fit cannot find a proper set of parameters to accurately reproduce both the continuum and the lines (possibly due to different dust extinction in birth clouds and the galaxy as a whole or a complex galactic environment that is impossible to simulate with our model; see Figure 4.19 as an example). Finally, we must acknowledge that there is a known degeneracy between dust and age in SED fitting (e.g., Pacifici et al. 2023), meaning that the A_V extracted from the SED fitting can sometimes differ from the real value because of the modeled SFH history.

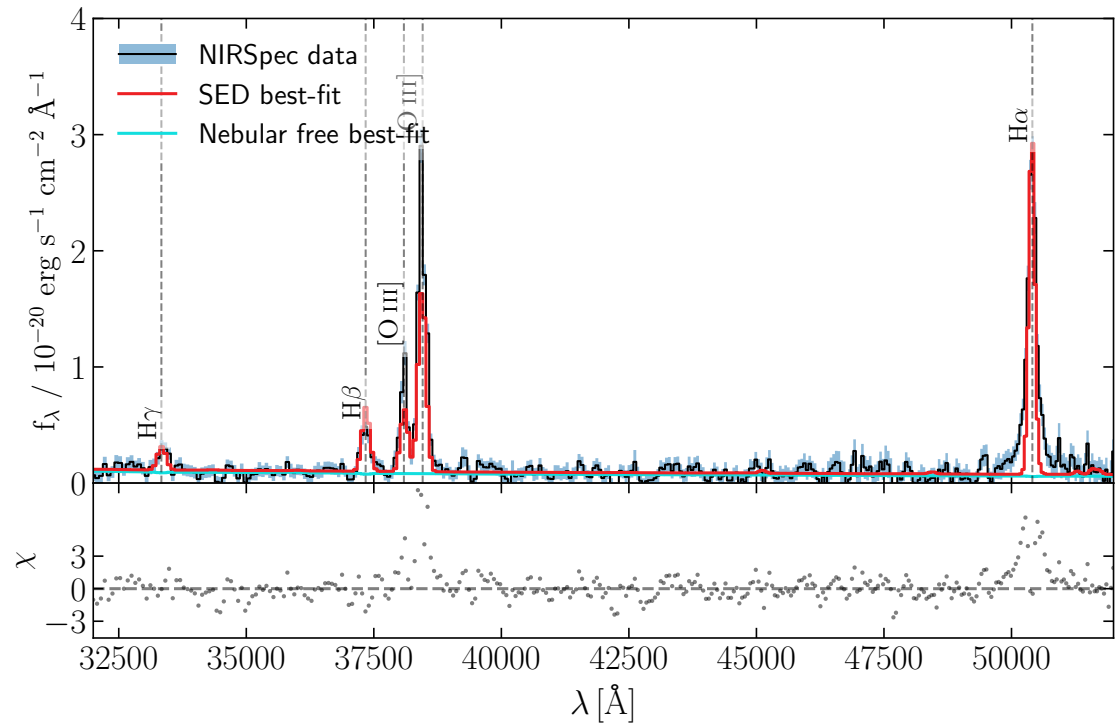


Figure 4.19: The SED best-fit with the masked [O III] lines of the galaxy NIRSpec ID 38509 at redshift $z = 6.7$. A broader component of the $H\alpha$ line is visible meaning that the galactic environment is more complex than what is modeled. The presence of such a broad line component may suggest the presence of an AGN (accreting supermassive black hole) in the galaxy. The galaxy cannot be well-fitted for this reason. We must stress that the Oxygen lines are not fitted well because they are masked in the fitting. This galaxy has been excluded from the sample for further analysis.

C H A P T E R



Results

In this chapter, we will discuss the properties of the star formation histories inferred from the SED fitting of the sample of galaxies at redshift $z > 6$ as a function of other inferred properties of the galaxies, such as their stellar mass, metallicity, dust extinction and redshift. Firstly, Sec. 5.1 exhibit an overview of the computed properties of the sample of galaxies (redshift, metallicity, stellar mass and dust extinction), then Sec. 5.2 highlight the result obtained from the statistical interpretation of the star formation histories of these galaxies. Sec. 5.3 shows results about the specific star formation rates and dust content linked to the mass and redshift of these galaxies.

5.1 Inferred properties of the sample

The analyzed galaxies present physical characteristics, such as redshift, mass, metallicity and dust extinction that are necessary to be known to interpret properly the results of the following analysis. Figure 5.1 shows the distribution of the physical properties I have inferred from the sample. For what concern the redshift, most of the selected galaxies have a redshift between 6 and 7.5, the global quantities that I will obtain in the next sections are therefore more indicative of this redshift region, except when otherwise expressed. The redshift values shown are obtained from the fit without cutting off the [O III] lines¹.

The metallicity measured is obtained without cutting away the [O III] line and has already been commented in the Sec. 4.3.1. The mass and dust extinction measures of the galaxies are obtained by masking the [O III] lines in the SED fitting (Sec. 4.3). For what concerns the mass a comparison between the mass values obtained by varying the shape of the star formation history and without removing these lines will be shown in Figure 5.6.

¹The values of redshift obtained by masking the [O III] lines are compatible with those obtained by not cutting off these lines with a maximum deviation of 1‰

The dust extinction values are generally very low with $\approx 60\%$ of the galaxies with a visual dust extinction $A_V \leq 0.1$ and $\approx 92\%$ with $A_V \leq 0.$. This is compatible with the selection criteria adopted in choosing JADES targets. Most targets are selected from HST observations and/or with high UV fluxes (D'Eugenio et al. 2024), resulting in a greater number of weakly extinct galaxies and thus leading to an observational bias of targets towards less obscured objects.

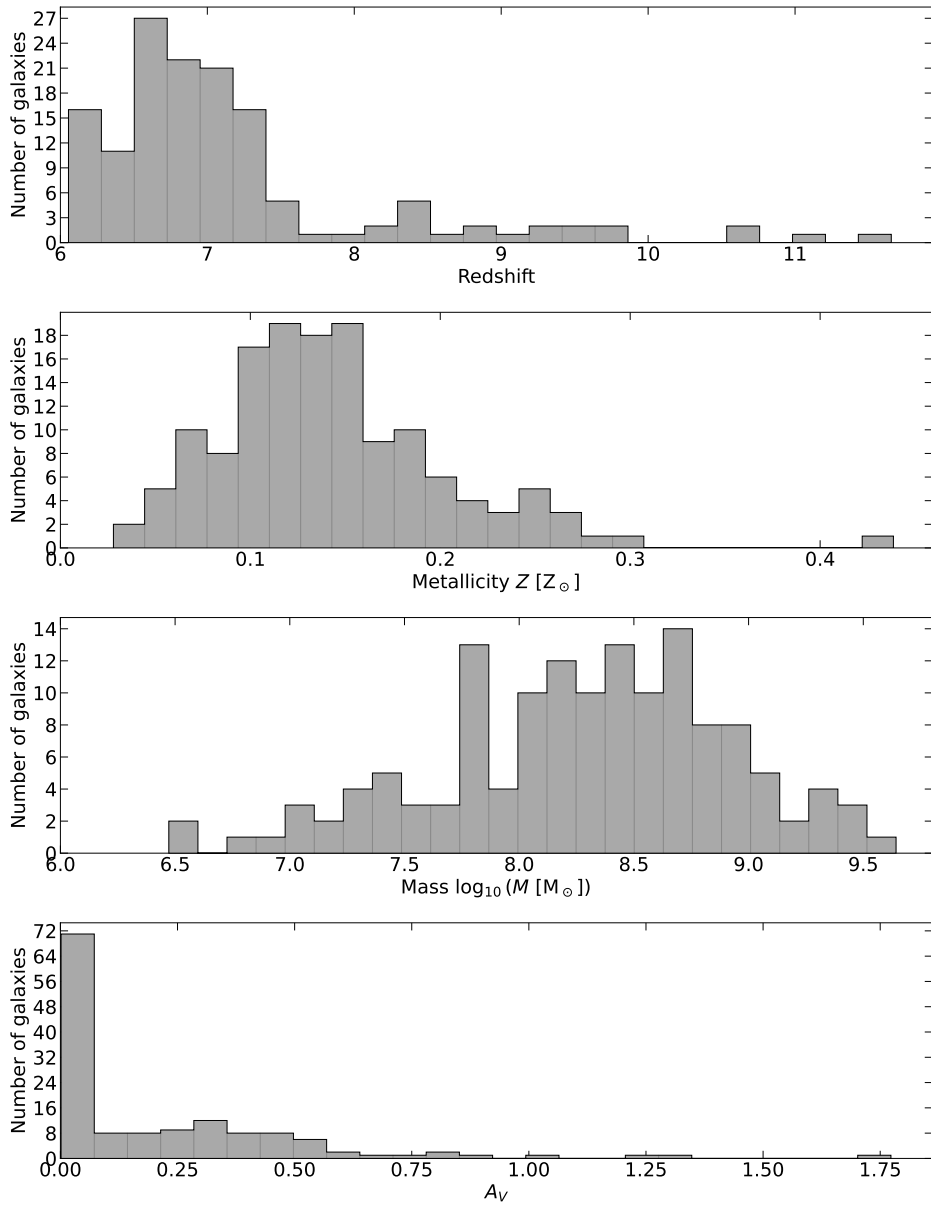


Figure 5.1: Properties of the sample of the galaxies. From top to bottom: redshift, metallicity, mass and dust extinction.

5.2 Star formation histories

One of the aims of the thesis is to statistically characterize the star formation history of galaxies at redshift $z > 6$. This section presents the result obtained from the SED fitting with a ‘step’ model of SFH as described in Sec. 4.1.4.

5.2.1 Burstiness of the star formation history

We have verified whether the galaxies are characterized by a bursty star formation history or not. In particular, we have investigated if the variability in SFH is consistent with the scenario expected by the feedback-free star formation model (Sec. 2.2.4). None of the 141 galaxies has more than two peaks of star formation. It was therefore decided to analyze how many of these galaxies have a bimodal functional shape and to study the time gap in which star formation remained inhibited in these galaxies. The gap in the SFHs of the galaxies is analyzed in the following way:

- If the galaxy presents a bimodal SFH (with two peaks with star formation greater than $2 M_{\odot}/\text{yr}$ interspersed with a star formation rate lower than $5 \times 10^{-2} M_{\odot}/\text{yr}$), the gap time between the two episodes has been computed.
- If the current star formation of the galaxy (in the last 5 Myr bin) is less than $5 \times 10^{-2} M_{\odot}/\text{yr}$, the distance between the star formation peak and the galaxy time was considered as the lower limit for gap time.

To keep only valuable data, only the galaxies for which the gap is visible in both the SFH measured with and without masking the [O III] lines are considered. The results are visible in Figure 5.2. According to the Li et al. 2023 prescriptions, there is no evidence of feedback-free bursts which would be visible as a series of fast bursts interspersed by low star formation periods no longer than 20 Myr. However, we did not expect to see any evidence of this type of process since at the observed redshifts the galaxies have a too low density (Sec. 4.4.1) compared to what the authors think is necessary to trigger an almost feedback-free star formation.

5.2.2 Mini-quenching evidences

Although it was not possible to observe the presence of bursts compatible with a feedback-free model, the observation of phases of suppressed stellar population for periods of around 100 Myr is particularly relevant.

Other studies showed that star formation was stochastic in early cosmic times and in low-mass galaxies Looser et al. 2023b, Tacchella et al. 2023, Mason et al. 2023, Whitler et al. 2023. Such rapid variability could take galaxies through starburst episodes and phases with suppressed star formation: so-called mini-quenching events.

The presence of quiescent galaxies at redshift $z > 6$ has been both simulated Dome et al. 2024b and directly observed Looser et al. 2023a and much more are identified at slightly lower redshifts (Carnall et al. 2023).

Compared to other similar works, the peculiarity of this thesis is the observation of

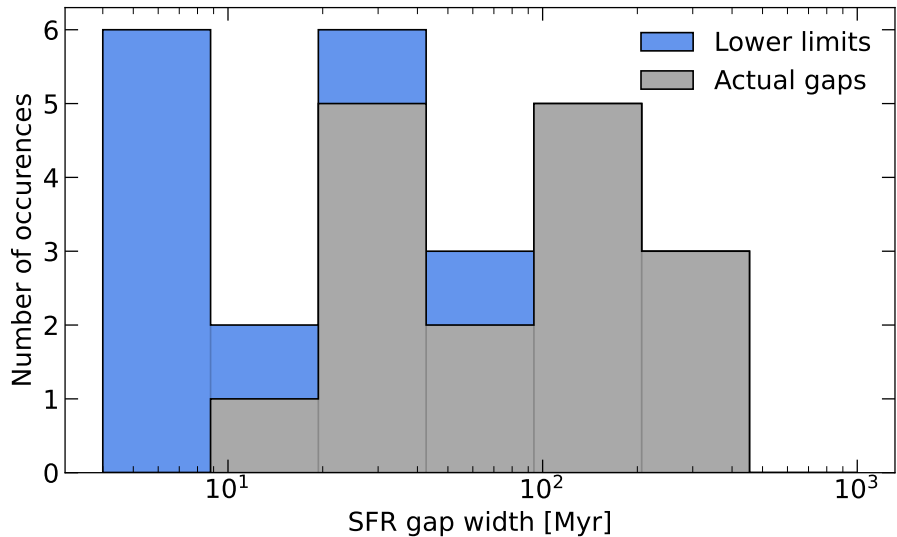


Figure 5.2: The gap time between two episodes of high star formation (see the text). In blue the lower bounds for the gap times measured in galaxies for which the star formation is suppressed at the present time.

galaxies after the quenching period, i.e. the observation of galaxies that have resumed their star formation after a period of inactivity. Instead, the works mentioned previously were only able to detect galaxies that are quenching at the time of observation and not in the past. In our sample, from what can be observed in Figure 5.2: 9 galaxies present a quenching period still in progress (the galaxies in blue) while 16 have presented a quenching period in the past according to what was fit by the SFH.

In figure Figure 5.3 two examples of quenched star formation are shown, one with quenching in the past and one currently quenched. The first one presents strong emission lines but with a moderate UV slope $\beta = -1.6$ which suggests a strong increase in the star formation rate over the last 5 to 10 Myr; at the same time a Balmer jump is visible, which shows the presence of a second, older stellar population. Indeed, this is actually the SFH shape deduced from the SED fitting. The second galaxy instead shows weak lines and a strong slope in the UV which could suggest the presence of strong star formation in the last 100 Myr, suppressed in the last 5-10 Myr. The best-fitting solution of the SED suggests a burst of 5 to 10 Myr in the past relative to the time of the galaxy.

The average quiescent time obtained in this work $t_q \approx 100$ Myr is compatible with the results of the FLARES simulations Lovell et al. 2023b, however both the scattering on the quenching times (we have a strong variability in the quenching times, from 10 to 300 Myr) and the fraction of galaxies that present a quenching period over the total amount of galaxies is higher than expected in simulations (Dome et al. 2024b, Lovell et al. 2023b). In particular Dome et al. 2024b expects to find between 0.6% to 0.9% in a quenching phase at redshift $z \approx 6$, while we are finding $9/141 \approx 6.4\%$ of such galaxies. A value 7 to 10 times higher.

It should be noted that the result obtained may be affected by the known age-dust

metallicity for which the spectrum of an older galaxy with few dust-extinction is very similar to the one of a younger extinct galaxy in the UV and optical rest-frame bands. Moreover, if the star formation zones are dustier than the galaxy as a whole, the emission lines would be particularly extinct, making the star formation appear older. However, in this work, the dust extinction has been assumed to be the same on the lines and the continuum and this type of analysis is left to a future continuation of the analysis. It would be interesting to investigate whether the spectrum of certain galaxies in the sample, which suggests a quenching phase, could be due to a higher level of dust extinction (or different extinction for lines and continuum extinction) rather than actual quenching. This analysis is not performed in this thesis and is left for further studies.

Galaxies that have a star formation gap in the past are particularly delicate to identify. A more detailed study of these galaxies that can identify whether a different combination of parameters can explain the observed spectrum, even without mini-quenching, will be important in the future.

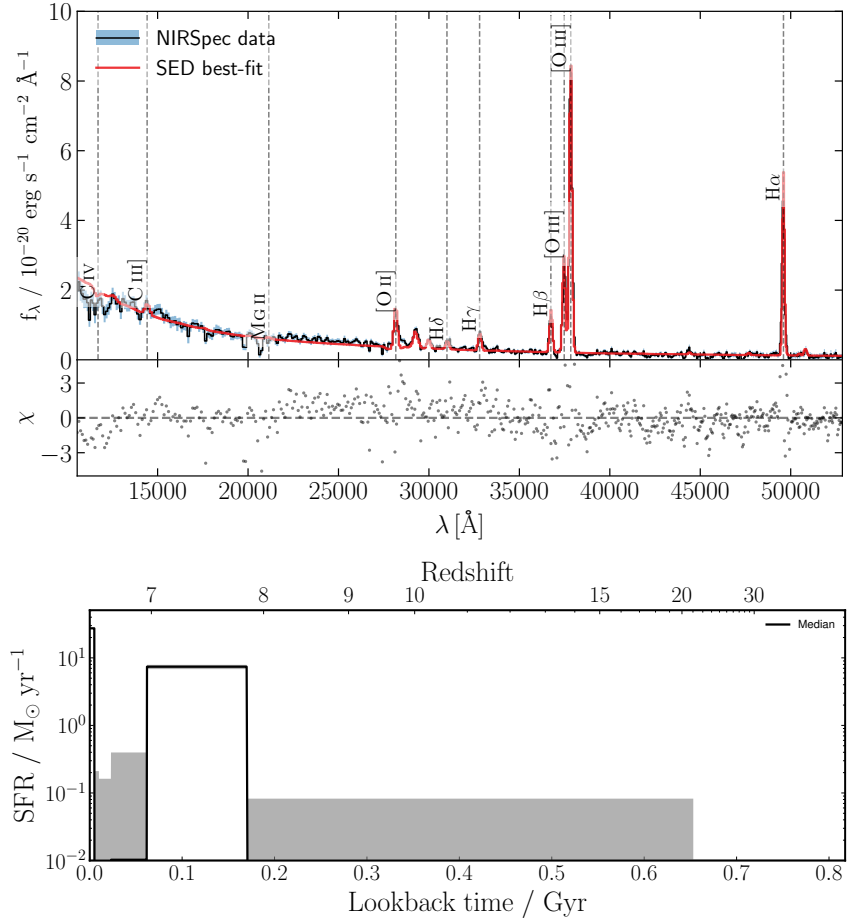


Figure 5.3: Example of SFH of one of the galaxies (NIRSpec ID 78891) with a quenching period in the past. A moderate Balmer jump is visible together with strong emission lines.

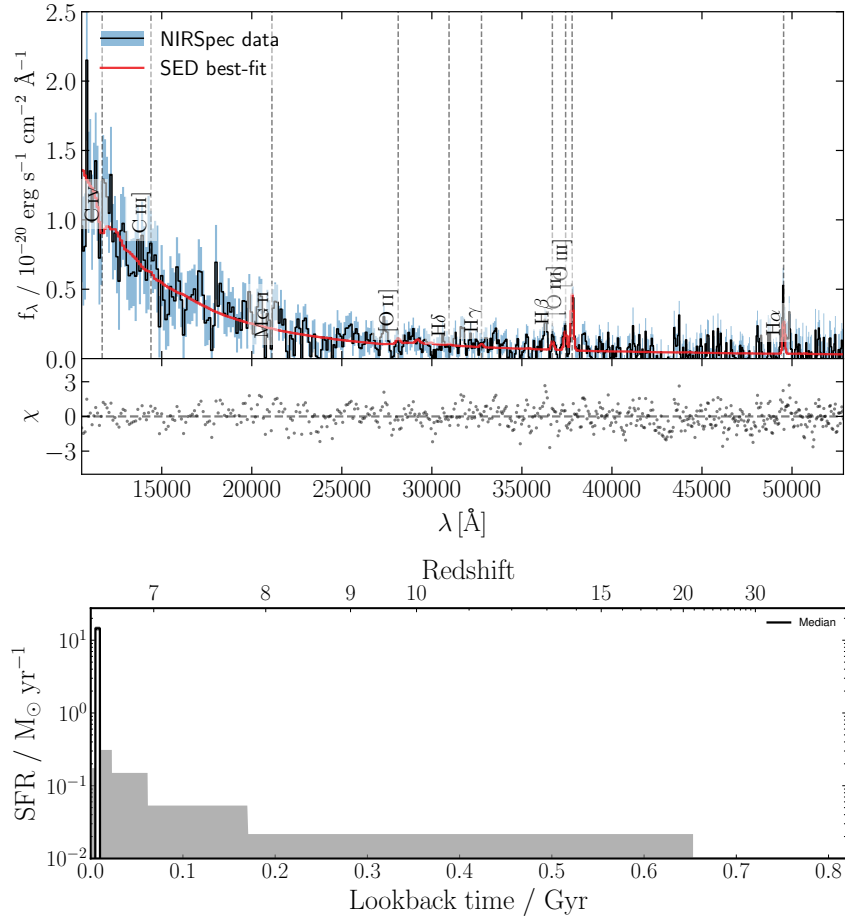


Figure 5.4: Example of SFH of one of the galaxies (NIRSpec ID 71983) which appears to be in a quenching period: the emission lines are very dim, but the UV slope is high $\beta = 2.4$

5.2.3 Characteristics of the SFH

Excluding the galaxies presented in the previous section Sec. 5.2.2, the sample reveals that most of the galaxies ($\approx 80\%$) present a continuous SFH that decreases with increasing lookback time. $\approx 20\%$ of the galaxies have only the last 5 Myr bin (the one nearest to the galaxy time) has a substantial star formation rate. Intending to study the star formation rate of the galaxies, this behavior is problematic. Indeed, it is not possible to distinguish the real timescale at which star formation occurs. For this reason, the entire sample of galaxies has been re-analyzed with BAGPIPES using a growing exponential SFH shape:

$$\text{SFR}(t) = \text{SFR}_0 e^{-t/\tau} \quad (5.1)$$

where SFR_0 is the current star formation rate (i.e. $\text{SFR}_0 = \text{SFR}(t = 0)$), t is the lookback time and τ the characteristic time of the star formation. The star formation is set to zero at redshifts greater than $z = 20$ assuming this is the epoch of the first stars to form (Dayal & Ferrara 2018). The fitting with the step function shows us that not every galaxy's SFH may be well-fitted by a simple exponential SFH profile, however, in this section, we are particularly interested in the fast-forming galaxies that cannot be well-fitted by the step functions and in this case, the exponential is a

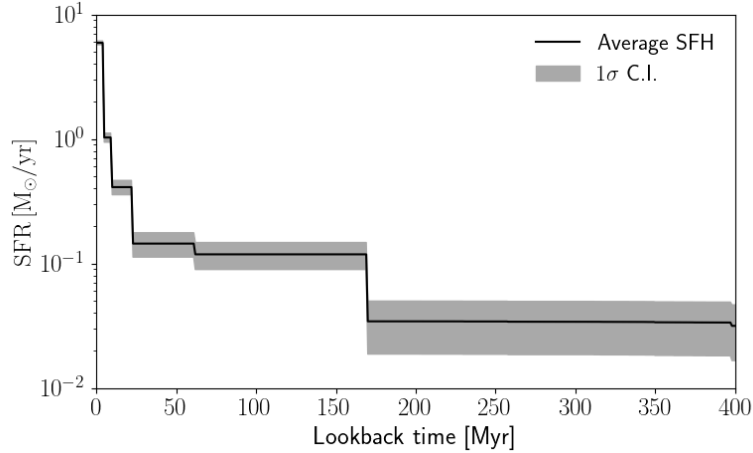


Figure 5.5: The average SFH of the 141 analyzed galaxies. The average has been computed normalizing the mass of the galaxies to $10^8 M_\odot$. The majority of the galaxies have a fast-growing SFH.

good simple solution to immediately have the characteristic time of star formation. We can now derive the specific star formation rate sSFR for this SFH profile. The sSFR is the ratio between the star formation rate at the galaxy time divided by the stellar mass of the galaxy, and it represents a measure of the star formation per unit of mass. The specific star formation rate characterizes how the instantaneous star formation is determined by the galaxy's past star formation history, For an exponential star formation rate, using Eq. 5.1, we can derive:

$$\text{sSFR} := \frac{\text{SFR}_0}{M_\star} = \frac{\text{SFR}_0}{\int_0^{t_{20}} dt \text{SFR}_0 e^{-t/\tau}} \xrightarrow{t_{20} \rightarrow \infty} \tau^{-1} \quad (5.2)$$

where t_{20} is the lookback time relative to the galaxy time of the $z = 20$ epoch (i.e. $z(t_{20}) = 20$). The approximation derives from the cut of the star formation at redshift $z = 20$. The result obtained in Eq. 5.2 improves with smaller τ . The exponential shape is the one which proceeds at constant SFR.

Stellar masses We now want to compare the stellar mass inferred from the different SED fitting performed in this thesis. As a summary, the galaxies have been fitted with 3 different models of star formation:

- The non-parametric ‘step’ model with the [O III] lines unmasked (Sec. 4.1.5)
- The non-parametric ‘step’ model with the [O III] lines masked (Sec. 4.3)
- The growing exponential model with the [O III] lines masked (Described in the current section)

To check the consistency between the results obtained with these three models I have compared the stellar mass found with these three models (see Figure 5.6). You can see that there is a trend in the data: low-mass galaxies are even less massive with the exponential model and massive galaxies are generally even more massive with the exponential model. The reason may be that the star formation observed, on average,

is faster in less massive galaxies (as it will be shown in Figure 5.7) with many galaxies with a characteristic star forming time faster than 5 Myr. These are the galaxies for which the ‘step’ function cannot well reproduce the fast-growing SFH resulting in higher masses (In the ‘step’ model the SFR must remain constant for at least 5 Myr which is the first bin size). On the opposite side, at higher masses, the SFH is often longer and complex. To fit older populations the growing exponential τ has to be large, forcing the star formation rate to remain high for a long time even if the true SFH could be interspersed with moments of low star formation as highlighted in Sec. 5.2.1. This tends to increase the estimated stellar mass. Considering both the deviation and the scattering, the difference between the various models is typically 0.3 dex.

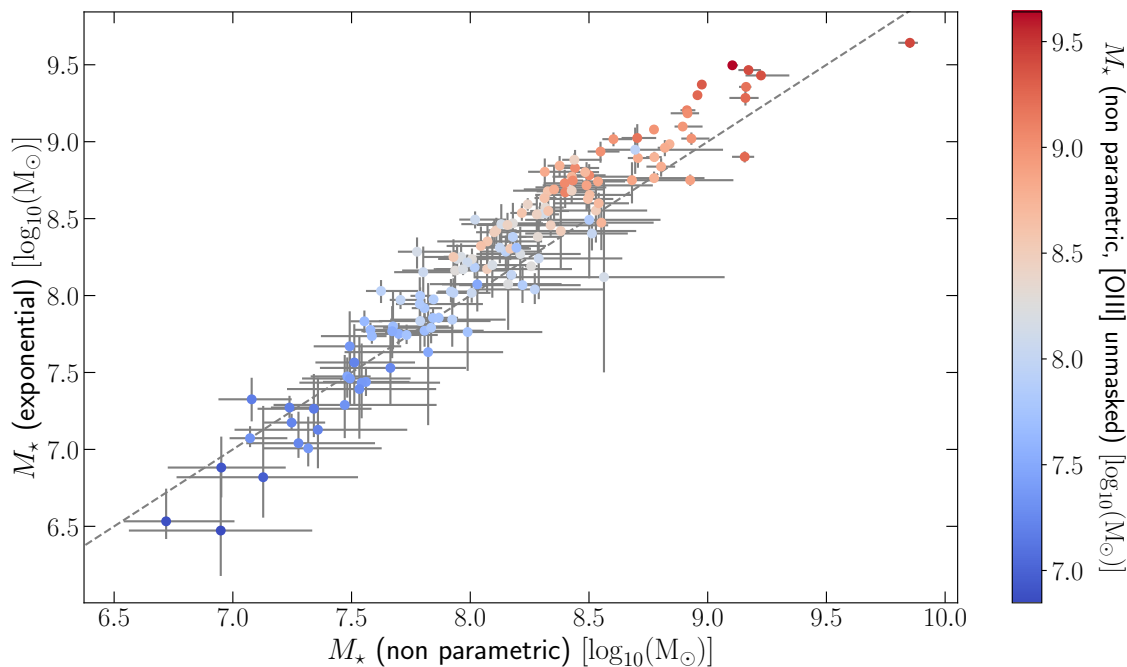


Figure 5.6: The stellar mass obtained with the different models. On the y -axis the the growing exponential model, on the x -axis the ‘step’ model and the colors mark the ‘step’ model results obtained without masking the [OIII] lines. A slight trend is visible in the plot as described in the text. The deviation plus the scattering has a magnitude of 0.3 dex.

5.3 Dust and super-Eddington galaxies

This section investigates the relations between the mass of the galaxies, specific star formation rate, dust content and redshifts. The main objective is twofold, on the one hand, to verify whether these quantities are related to each other and on the other to study if there is any correlation between super-Eddington galaxies and dust extinction in the same galaxies, as prescribed by the model presented in Sec. 2.2.5.

In this section we are particularly interested in galaxies with fast star production, for this reason, we use the data obtained with an exponential SFH model (Sec. 5.2.3)

which is more sensitive to the fast ($\lesssim 5$ Myr) characteristic time of star formation of the galaxies with strong specific star formation rates.

5.3.1 Mass - sSFR - dust extinction

The first result of interest is the relationship between the stellar mass of galaxies, dust extinction, and the characteristic star formation time τ (which is equal to the inverse of the specific star formation rate for the exponential model).

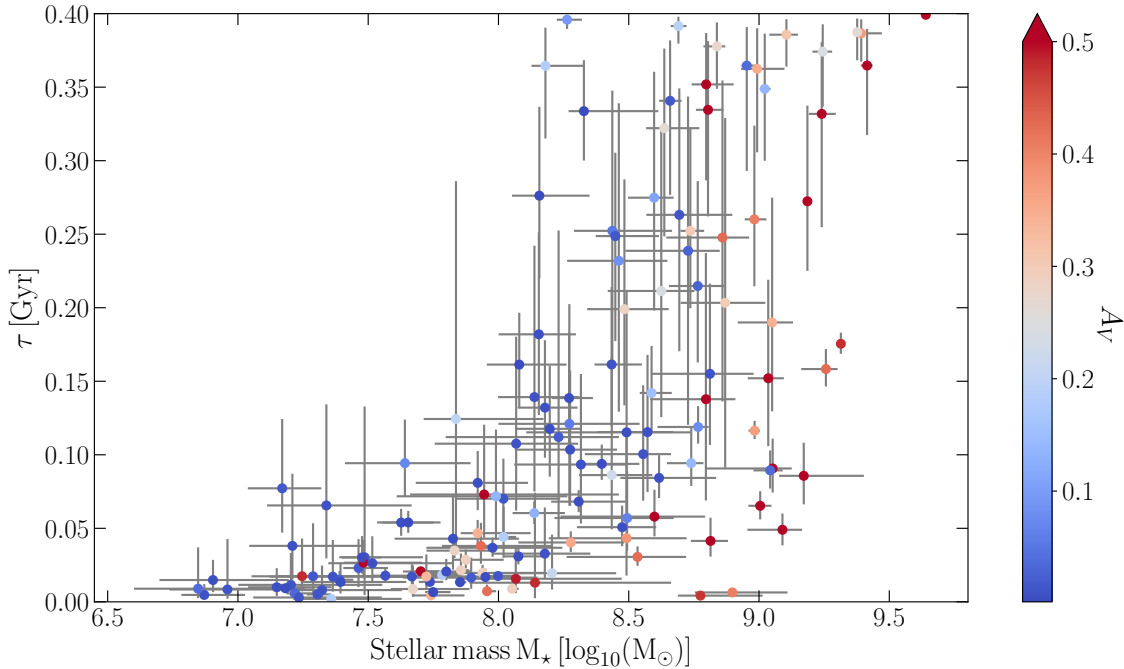


Figure 5.7: Stellar mass vs exponential characteristic star formation time. The points are colored with the dust extinction of the galaxy A_V . Completely red points have $A_V \geq 0.5$

Figure 5.7 shows the relationship between these quantities. Two main facts stand out:

- All galaxies are located within a narrow region of the mass diagram - τ : galaxies with stellar masses between $10^{6.5} \leq M_* < 10^{8.5}$ have $\tau < 150$ Myr while galaxies with $M_* > 10^{8.5}$ have higher τ on average. No galaxies are observed with $M_* > 10^{10}$.
- At fixed τ , more massive galaxies have greater dust extinction.

Location of the galaxies in the diagram The observed galaxies are disposed along a curved stripe in the diagram stellar-mass - τ . The low-mass limit of this stripe may be due to the sensitivity of NIRSpec and the selection criteria adopted (Figure 5.8). I have generated mock spectra to find what was the limiting curve of the selection criterion (Sec. 3.5) adopted. The limiting sensitivity has been found exploiting the fact that the SNR (signal-to-noise ratio) has the following

dependencies:

$$\text{SNR} \propto M_{\star} \quad (5.3)$$

$$\text{SNR} \propto t_{\text{exp}}^{1/2} \quad (5.4)$$

where t_{exp} is the exposure time of the spectrum. For sure the lack of points in the

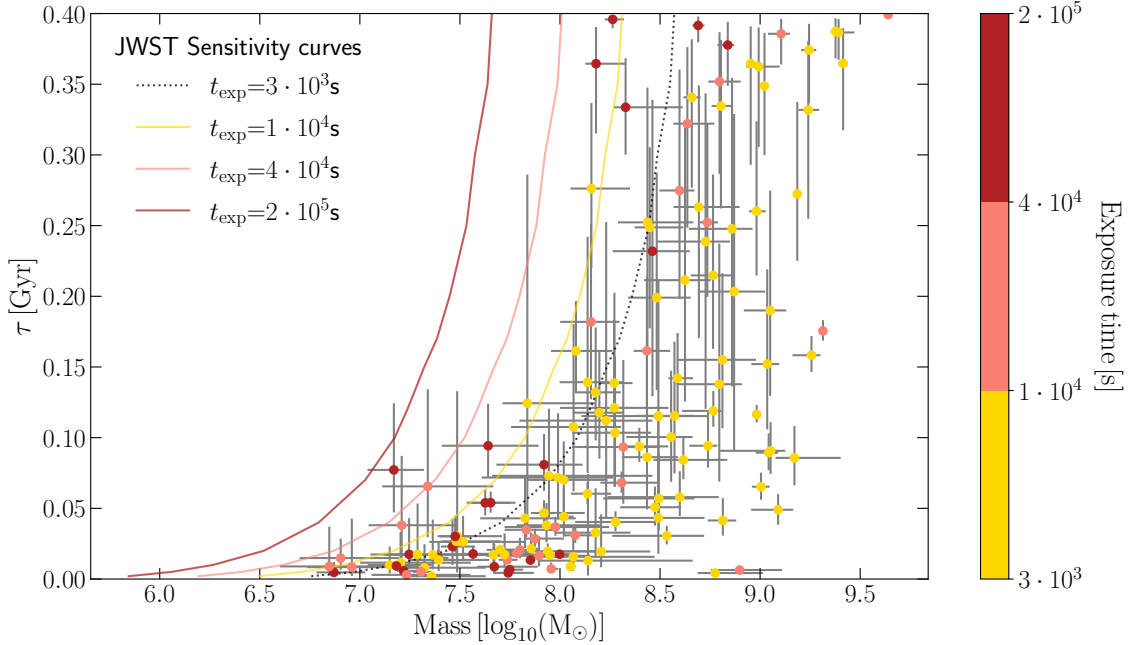


Figure 5.8: The stellar mass - τ plane and the sensitivity curves found. The points are colored with the exposure time used to take the spectrum of that galaxy.

left part of the plot is a consequence of the sensitivity of the observation, however, you can also see a lack of points immediately to the right of the sensitivity curves from stellar masses $10^{7.5}M_{\odot} \leq M_{\star} < 10^9M_{\odot}$ with $\tau > 0.2$ Gyr. This fact will be later investigated in Sec. 5.3.2.

Even in the right part of the plot, at masses $M \gtrsim 10^9M_{\odot}$ the number of galaxies is low, and it decreases towards higher masses. Here we are focusing only on the distribution of masses independently on τ , which could already be characterized from Figure 5.1. The decreasing number of galaxies with increasing mass may be a consequence of the decreasing probability of finding massive galaxies. To confirm this hypothesis we do a rough estimation² of the expected number of galaxies that should be observed at masses $M \geq 10^9M_{\odot}$ given the number of galaxies that are present in the analyzed sample with masses $M \leq 10^{8.5}M_{\odot} < 10^9M_{\odot}$. To compute this estimation I use the stellar mass function $\phi_{\star}(M_{\star})$ at redshift $z = 6$, which is the number density of galaxies in the Universe per stellar mass, proposed by Stefanon

²Here I am assuming the JADES data target selection criterion to be agnostic to the galaxy mass. However, this estimate can still give some clues about the variation in the number of galaxies expected as their stellar mass increases.

et al. 2021 and here described:

$$\begin{aligned}\phi_{\star}(M_{\star} = 10^{8.5} M_{\odot}) &\approx 6.2 \times 10^{-3} \text{ Mpc}^{-3} \text{dex}^{-1} \\ \phi_{\star}(M_{\star} = 10^9 M_{\odot}) &\approx 2.2 \times 10^{-3} \text{ Mpc}^{-3} \text{dex}^{-1} \\ \phi_{\star}(M_{\star} = 10^{9.5} M_{\odot}) &\approx 6.9 \times 10^{-4} \text{ Mpc}^{-3} \text{dex}^{-1} \\ \phi_{\star}(M_{\star} = 10^{10} M_{\odot}) &\approx 1.7 \times 10^{-4} \text{ Mpc}^{-3} \text{dex}^{-1}\end{aligned}$$

Above $M_{\star} = 10^{8.5} M_{\odot}$ the galaxies are not affected by observation sensitivity limit (Figure 5.8). Between $M_{\star} = 10^{8.5} M_{\odot}$ and $M_{\star} = 10^9 M_{\odot}$ there are $N_{8.5}^{\text{obs}} = 23$ observed galaxies in the analyzed sample at redshifts $6 < z < 7$. This is the value used to estimate the number of expected galaxies in the sample at higher masses. So, we can expect to observe:

$$N_9^{\text{ext}} = \frac{\phi_{\star}(M_{\star} = 10^9 M_{\odot})}{\phi_{\star}(M_{\star} = 10^{8.5} M_{\odot})} N_{8.5}^{\text{obs}} \approx 8 \quad (5.5)$$

between $M_{\star} = 10^9 M_{\odot}$ and $M_{\star} = 10^{9.5}$. A similar equation holds for higher mass ranges. Likewise, $N_{9.5}^{\text{ext}}$ is expected to be $N_{9.5}^{\text{ext}} \approx 2$ where only one galaxy has been observed in the sample. Finally, the expected number of even more massive galaxies is expected to be well below 1 where, indeed, no galaxies have been detected. There is, therefore, no evidence to say that the right limit of the galaxies in the Figure 5.8 is nothing more than a natural low frequency of massive galaxies.

What is instead of interest is the almost total absence of galaxies with a mass greater than $M \gtrsim 10^8 M_{\odot}$ and $\tau < 50$ Myr. This observation suggests that massive galaxies are unlikely to form too quickly.

Dust extinction The second characteristic to notice in Figure 5.7 is the dust attenuation in the analyzed galaxies. Two features are relevant:

- **At fixed τ , more massive galaxies have higher dust extinctions.** This behavior was expected, indeed supposing constant dust to stellar mass ratio f_d , the dust extinction is proportional to the dust column density (N_c):

$$A_V \propto N_c \propto \rho_d R = \frac{f_d M_{\star}}{R^3} R \quad (5.6)$$

where ρ_d is the dust density and R the radius of the galaxy. At high-redshift, the mass-radius of the galaxy follows the function $R \propto M_{\star}^{0.19}$ (Morishita et al. 2024) measured on high confidence photometric candidates galaxies observed through JWST. The radius in the previous equation is the effective radius³ of the galaxy. Using the mass-radius relation, more massive galaxies should have higher dust extinctions, which is in fact what is observed. Indeed, using

- **No dependence of A_V on τ is visible.** According to the super-Eddington model described in Sec. 2.2.5, galaxies with a sSFR $> 25 \text{ Gyr}^{-1}$ are expected to have a strong enough radiation field to clear the galaxy from dust. Using

³Radius which contains half of the light of the galaxy

Eq. 5.2 we would expect a very low dust extinction for each galaxy which satisfies

$$\tau < \frac{1}{25 \text{ Gyr}^{-1}} = 0.04 \text{ Gyr} \quad (5.7)$$

However, this limit is not observed and galaxies with high sSFR are observed to be as dusty as their counterpart with slower star formation.

5.3.2 Redshift - sSFR - mass

Another result obtained is the characterization of star formation as a function of redshift and stellar mass. Also in this case the exponential star formation history

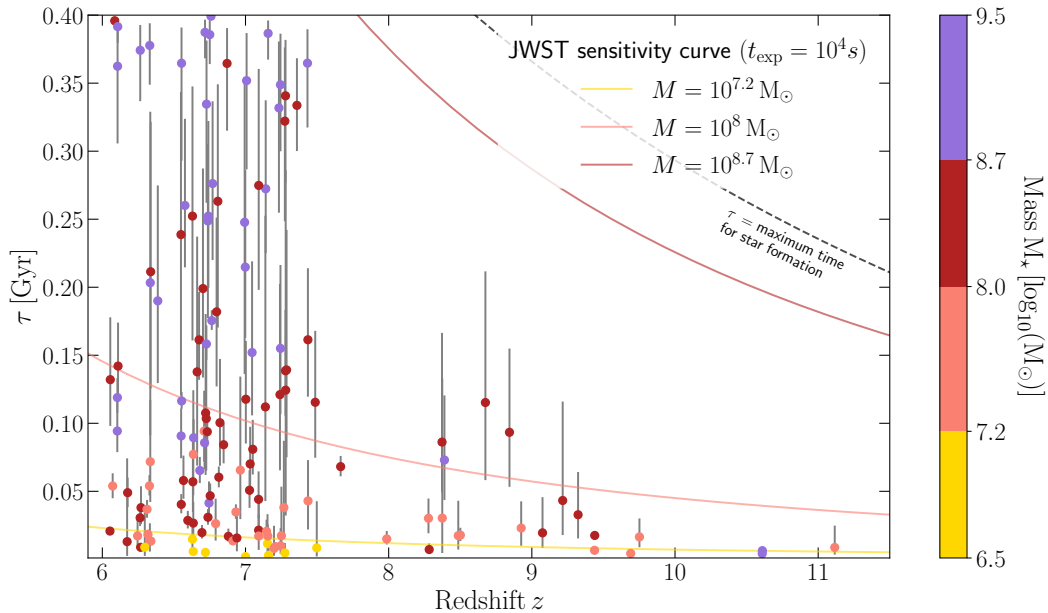


Figure 5.9: The redshift - τ plane and the sensitivity curves found. The points are colored with the stellar masses of the galaxies. The dashed black line is the line for which 1τ is equal to the available star formation time for the galaxy, which is the cosmic time between redshift $z = 20$ and the redshift of the galaxy.

model was used. Figure 5.9 shows the results obtained together with the expected sensitivity curves. Galaxies at higher redshifts appear increasingly likely at smaller τ characteristic times. From the figure, it is impossible to state whether this is an intrinsic property of the galaxies or only a bias due to the varying sensitivity curves with redshift. Indeed, the sensitivity is lower at higher redshifts due to the larger luminance distance of the objects. Similarly to Figure 5.8, the sensitivity curves were traced by generating mock spectra of galaxies with exponential SFH and varying characteristic time of star formation and finding those that would have exceeded the adopted selection criterion described in Sec. 3.5.

This section aims to find whether the characteristic star formation time depends on mass and/or on redshift. To correctly look for the correlation between these

quantities, we have to consider that part of the galaxies existing in the Universe cannot be present in the analyzed sample due to the sensitivity limit of the instrument and the selection criterion adopted.

We parametrize τ taking into account two conditions:

- τ has to be larger than zero, i.e. galaxies cannot form instantaneously;
- The probability that τ is larger than the Universe age t_U at the time of the galaxy has to be low. The star formation histories described by $\tau \gg t_U$ converge to a constant rate of star formation from $z = 0$ to the galaxy's redshift. Moreover, a high τ corresponds to a SFH with a step function at redshift $z \approx 20$ profile that may be unphysical. For these reasons, we expect the probability distribution at large τ to go to zero.

With these constraints, it was decided to describe the distribution of characteristic times τ with a beta prime distribution:

$$p(\tau) = \text{Beta}'(\tau; \alpha, \beta) \propto \tau^{\alpha-1} (1 + \tau)^{-\alpha-\beta} \quad (5.8)$$

The galaxies with masses $7.2 \leq \log_{10}(M_\star [\text{M}_\odot]) < 8$ have been divided into 2 sets based on redshifts (the first set contains galaxies with $6 < z < 7.5$, the second one $8 \leq z < 11.5$). The same division has been done for galaxies with masses $8 \leq \log_{10}(M_\star [\text{M}_\odot]) < 8.7$. For each one of these four sets the α and β posterior has been computed in the way that will be described shortly.

Giving a uniform prior on α and β and calling D the dataset of observed galaxies and I any other information about the observations such as the sensitivity limit, we have that:

$$p(\alpha\beta | DI) \propto \mathcal{L}(D | \alpha\beta I) \quad (5.9)$$

where \mathcal{L} is the likelihood of the data sample. It is reasonable to assume that the measurements are independent galaxy by galaxy, then calling c_i the sensitivity limit of the i -th galaxy and τ_i its characteristic time measure and being N the number of galaxies in the analysis set:

$$p(\alpha\beta | DI) \propto \prod_{i=1}^N \mathcal{L}(\tau_i | \alpha\beta I) = \prod_{i=1}^N \frac{\int_0^{c_i} d\tilde{\tau} \text{Beta}'(\tilde{\tau}; \alpha, \beta) p(\tau_i | \tilde{\tau})}{\int_0^{c_i} d\tilde{\tau} \text{Beta}'(\tilde{\tau}; \alpha, \beta)} \quad (5.10)$$

where $p(\tau_i | \tilde{\tau})$ is the error distribution on the i -th measure which is obtained directly from the SED fitting posterior on τ_i . The denominator accounts for the impossibility of observing galaxies with τ greater than the limiting sensitivity.

The sensitivity limit has been computed galaxy by galaxy considering the exposure time t_{exp} , the redshift of the galaxy z , its stellar mass M_\star and its dust extinction A_V . The sensitivity limit is assumed to be 'hard' i.e. the probability of observing a galaxy with $\tau_i > c_i$ is immediately null. Calling c_0 the maximum τ for which a galaxy of stellar mass $M_0 = 10^8 \text{ M}_\odot$ without dust is visible with an exposure of $t_0 = 10^4 \text{ s}$ at redshift $z_0 = 6$, than the limiting sensitivity on τ for a galaxy is:

$$c = c_0 \sqrt{\frac{t_{\text{exp}}}{t_0}} \left(\frac{d_L(z_0)}{d_L(z)} \right)^2 \frac{M_\star}{M_0} 10^{-0.4(2.8A_V)} \quad (5.11)$$

c_0 has been computed from mock spectra, while the first term comes from the fact that the signal-to-noise ratio increases with the square root of the exposure time. The second term accounts for the varying luminosity distance d_L with redshift and the third term considers that the galaxy's luminosity increases with its mass when any other parameter is fixed. Finally, the last term takes into account the dust extinction: the main selection criterion (Sec. 3.5) is based on the SNR at $\lambda_{\text{SNR}} = 200 \text{ nm}$. According to the Calzetti law (Sec. 4.1.2)

$$A_{200} = 2.8A_V \quad (5.12)$$

which means that the observed flux F_{obs} at this wavelength, respect to the intrinsic unattenuated one F_{int} is:

$$\frac{F_{\text{obs}}}{F_{\text{int}}} = 10^{-0.4(2.8A_V)} \quad (5.13)$$

The posterior on α and β and the obtained distributions on τ are visible in Figure 5.10, while the results are visible in Table 5.1. At least two facts are relevant:

- The distribution of the characteristic times τ is different depending on the mass: at fixed redshift, the distributions for the two different mass ranges are completely different from each other. Massive galaxies have a generally longer formation history.
- The distribution of characteristic star formation times is redshift dependent. The difference in the distribution tells us that at higher redshifts the characteristic star formation time is shorter on average.

M_\star	z	α	β	$\langle \tau \rangle [\text{Myr}]$	$\sigma_\tau [\text{Myr}]$
$10^{7.2} \leq M_\star [\text{M}_\odot] < 10^8$	$6 < z < 7.5$	$2.22^{+0.59}_{-0.53}$	56^{+24}_{-20}	41^{+14}_{-8}	29^{+14}_{-5}
	$8 < z < 11.5$	$3.0^{+1.4}_{-1.1}$	220^{+130}_{-95}	14^{+4}_{-3}	$8.7^{+5.4}_{-2.0}$
$10^8 \leq M_\star [\text{M}_\odot] < 10^{8.7}$	$6 < z < 7.5$	$1.91^{+0.39}_{-0.30}$	$6.1^{+4.0}_{-3.0}$	370^{+130}_{-130}	340^{+140}_{-120}
	$8 < z < 11.5$	$2.4^{+1.3}_{-1.0}$	43^{+32}_{-25}	62^{+57}_{-18}	44^{+120}_{-14}

Table 5.1: The values obtained for the distributions of τ in each analyzed set. $\tau \sim \text{Beta}'(\alpha, \beta)$. $\langle \tau \rangle$ is the average star formation time extracted from the distribution and σ_τ is the standard deviation of the distribution

As a consequence of the last point of the previous paragraph, the number of super-Eddington galaxies is therefore expected to increase with redshift. In this regard, it is interesting to infer from the computed τ distributions what is the expected fraction of super-Eddington galaxies in the two redshift ranges. Note that the results proposed here are valid only assuming the completeness of the galaxy sample observed with the third JADES release, which is here assumed.

As it has been described in Sec. 2.2.5, according to Ferrara 2024, I consider a galaxy to be super-Eddington if its specific star formation rate is:

$$\text{sSFR} > 25 \text{ Gyr}^{-1} \quad (5.14)$$

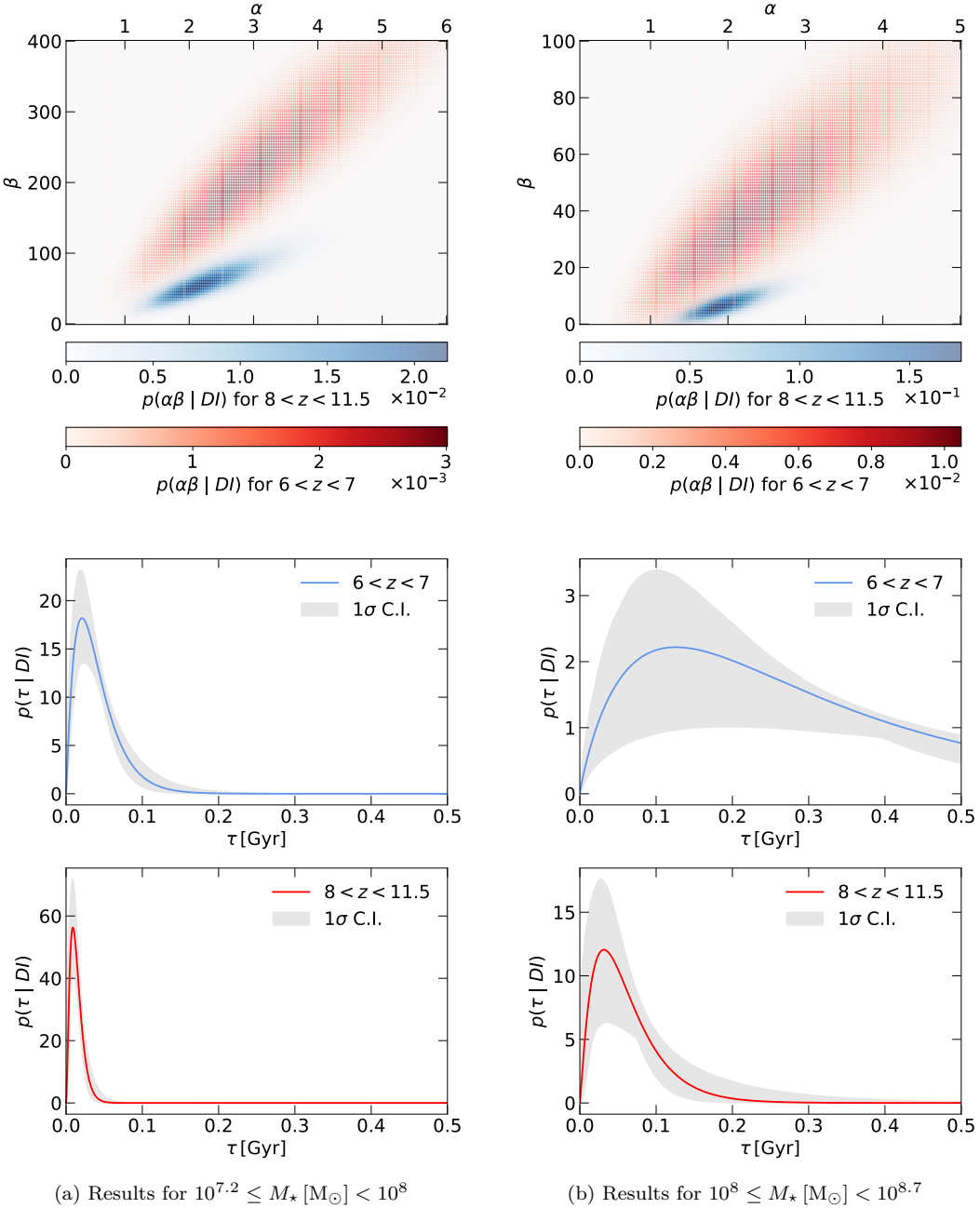


Figure 5.10: On the left the graphs refer to the lower masses intervals, on the right to the higher masses range. For each of the two sets of masses: at the top the posteriors on α and β for the two ranges of redshifts, in the middle the τ distribution for redshifts $6 < z < 7$ with its uncertainty visible as a gray shaded region, at the bottom the τ distribution for redshifts $8 < z < 11.5$.

using Eq. 5.2 we have that the fraction of super-Eddington galaxies in a set of galaxies for which $\tau \sim \text{Beta}'(\alpha, \beta)$ is:

$$f_{\text{Edd}} = \int_0^{40 \text{ Myr}} dx \text{ Beta}'(x; \alpha, \beta) \quad (5.15)$$

The expected fraction of super-Eddington galaxies is mass-dependent and is generally increasing with redshift. Table 5.2 shows the values obtained from the inferred distributions. The comparison with the [Ferrara 2024](#) model for the expected fraction of super-Eddington galaxies is meaningless because of the mass-dependence relation found in this thesis. Therefore, to the best of our knowledge of this thesis, we can only say that the global fraction of super-Eddington galaxies is a sample-dependent quantity (compared to the quantity estimated by Ferrara which was a value independent of the mass). For example, a survey focused on lower-mass galaxies would find a much higher fraction of super-Eddington galaxies.

It is interesting to note that the fraction of super Eddington galaxies differs by more than 3σ both with varying redshift and with varying mass, confirming that the distribution of characteristic times of galaxies depends on both of these quantities.

f_{Edd}	$6 < z < 7.5$	$8 < z < 11.5$
$10^{7.2} \leq M_\star [\text{M}_\odot] < 10^8$	$0.59^{+0.11}_{-0.14}$	$0.99^{+0.01}_{-0.05}$
$10^8 \leq M_\star [\text{M}_\odot] < 10^{8.7}$	$0.03^{+0.03}_{-0.01}$	$0.36^{+0.18}_{-0.16}$

Table 5.2: The fraction of super-Eddington galaxies as a function of mass and redshift.

CHAPTER



Summary and conclusions

Thanks to its sensitivity and wavelength coverage, the NIRSpec spectrograph on the JWST is the perfect instrument to study the properties of galaxies in the first billion years of the Universe. The spectroscopic data of galaxies from the JADES 3rd release represent a unique view into the cosmic dawn between redshifts $6 < z < 12$.

In this thesis, we use the spectral energy distribution fitting technique to infer the physical properties of these primordial galaxies, such as their star formation history, dust extinction, metallicity, and redshift. We use BAGPIPES to perform the SED analysis, which is a package that adopts a grid of synthetic stellar population and line emission models to reproduce the spectra and photometric data of observed galaxies. Therefore the results of the SED fittings are the best-fitted free parameters associated with the stellar populations (i.e. stellar mass, SFH, stellar age) into interstellar medium properties (i.e. ionization parameter, dust extinction, metallicity).

In this thesis, we statistically characterize the star formation history of galaxies at redshift $z > 6$ from the JADES 3rd release aiming to find evidence of bursty star formation and correlation between the star formation history and physical properties of the galaxy. We perform three different SED fitting procedures to test the bagpipes code and assess any uncertainties and biases in the results: one with a non-parametric star formation history model, one fixing the metallicity of the galaxies using the result of the first fitting and masking the [O III] lines, and one with a growing exponential SFH model.

The key results of this thesis are as follows:

- A group of galaxies presents strong [O III] emission lines which alter the results of the SED fitting. When these lines are not masked, the measured ionization parameter is very high ($\log \mathcal{U} \gtrsim -0.5$) and the specific star formation rate is extreme ($sSFR \gtrsim 500 \text{ Gyr}^{-1}$ with values as high as $sSFR \sim 1000 \text{ Gyr}^{-1}$). Neither the use of stellar population which includes the evolution of binary star systems nor the use of higher electronic density in H II regions, where the [O III] are expected to form, change the result.

- The electronic density measured from the $[\text{O II}]\lambda\lambda 3729, 3726$ line ratio measured from an SNR-weighted average of the spectra of the entire sample of galaxies is $n_e = (3 \pm 1) \times 10^2 \text{ cm}^{-3}$ which is greater than the typical values in local galaxies and compatible with the results of other works at high redshift (e.g. Isobe et al. 2023)
- Approximately 6% of the galaxies in the analyzed sample exhibit very low star formation rates ($\text{SFR} < 5 \times 10^{-2} M_\odot/\text{yr}$) in the last 5 Myr, despite having had high star formation rates in the past. This fraction of galaxies with inhibited star formation is about ten times higher than expected from simulations (e.g., Dome et al. 2024a) at these redshifts. One possibility, not explored in this thesis, is that star-forming regions may be dustier than the galaxy. This could result in suppressed emission lines, even if star formation is ongoing. Consequently, these dusty star-forming regions might be misinterpreted as older stellar populations due to their low emission lines.
- There is no evidence of rapid bursts of star formation compatible with feedback-free star formation models (Sec. 2.2.4). This result was expected because electron density in the analyzed galaxies is too low for feedback-free models to be applicable.
- The dust extinction is mass and star formation rate dependent. Massive galaxies have stronger extinction. On the other hand, at fixed stellar mass, dust is higher in galaxies that have formed their current stellar mass in shorter time scale.
- Galaxies that are expected to be super-Eddington due to their high specific star formation rate are not less extinct than other galaxies. This result is in contrast with the dust-free model described in Sec. 2.2.5.
- The characteristic time of star formation is found to be mass and redshift-dependent. At higher redshift star formation evolves rapidly with intense bursts. At fixed redshift, the star-formation history evolves more slowly in more massive galaxies. This result suggests that star formation in galaxies is initially fast and bursty and becomes more steady over time when more gas is converted into stars and the stellar mass increases.

The results obtained in this thesis represent only the beginning of the investigation into the star formation histories (SFH) of early galaxies and their relation to physical properties. Even though this thesis utilizes one of the largest and deepest spectroscopic samples of galaxies at redshift $z > 6$, even larger statistical samples of galaxy spectra with a high signal-to-noise ratio (SNR) would improve the quality of the results obtained. Upcoming observations with JWST will provide such a sample. The future prospects of this work can be summarized as follows:

- A better understanding of the oxygen lines issue is needed to investigate the reasons for the different results of the SED fitting when these lines are masked compared to when they are not. Possible contamination from AGNs should be checked by cross-referencing data from multiwavelength surveys to detect X-ray (e.g., using the Chandra deep field Giacconi et al. 2002) and/or strong infrared

emission in dust-obscured AGNs (e.g., using future JWST/MIRI data, which have already been used to discover new AGNs at high redshift [Lyu et al. 2024](#), [Yang et al. 2023](#)). Another possible approach would be to use more updated stellar population models that could better model the emission of the nebular regions in star-bursting primordial galaxies (e.g., X-ray binaries not treated in BPASS such as [Lecroq et al. 2024](#)).

- A deeper analysis of the difference in dust content measured by SED fitting compared to the Balmer decrement techniques. It would be interesting to separate the dust extinction on the continuum from the dust extinction on emission lines. Moreover, further study is required for galaxies presenting high dust extinction from SED fitting but negligible dust extinction from line measurements, as star-forming regions, where emission lines are produced, are expected to be more extinguished than the starlight continuum.
- Another future approach is to use different SED fitting packages (e.g., PPFX [Cappellari 2017, 2023](#); PROSPECTROR [Johnson et al. 2021](#); GALAPY [Ronconi et al. 2024](#)) to confirm and identify limitations of the results obtained. Of particular interest would be to compare the results with those obtained from SED fitting packages that do not consider emission lines in the physical characterization of galaxy parameters (such as PPFX).
- Finally, larger samples of spectroscopic data would help to better characterize the distribution of characteristic timescales of star formation across different redshifts and masses.

Acknowledgments

This thesis, the result of my work, has only been made possible thanks to the support and help of many people. First of all, I would like to express my deepest gratitude to my supervisors, Dr. Stefano Carniani and Prof. Michele Cignoni, without whom this work would not have taken shape. Their valuable advice, from selecting the topic to the final writing stages, has guided me throughout, and I could always rely on their professionalism, availability, and support. A special thank you also goes to Eleonora Parlanti: our discussions helped me improve and broaden my understanding of this work. I am deeply grateful to Antonio for the comparisons and discussions that deepened my comprehension of the theoretical background of this work.

This thesis concludes a long journey supported by people who have been essential to me. My sincerest thanks go to my parents, who have always encouraged my curiosity and given me the opportunity to reach this far. Their constant support during difficult moments has been the driving force behind this achievement. I am deeply grateful to my dear friends Emanuele, Giorgio, Rachele, Annalisa, and Marco, who, throughout these years, have been a vital source of joy and have lightened the burden of long study periods. The moments we have shared have always been both a refuge and a source of happiness. Knowing I could always count on you has been invaluable as you've supported me on this long journey that began many years ago. Special thanks also go to my fellow astrophysics students, without whom I might not have completed all my exams so successfully. A particular thank you goes to Marco and Alice, wonderful friends and companions of unforgettable moments in Pisa. Getting to know them has truly been one of the most delightful parts of my master's journey. I cannot forget to thank Pierro and the 'Fermiani' group for their friendship over these years, their company during lunches, and many other shared moments. A heartfelt thank you to Debo for the unique friendship we have shared over the years, for the long conversations, the valuable advice, and for assisting me through the early years of university. Thanks to all of you, you have lightened the load of these years and filled them with wonderful memories. The academic achievement I present here is also a result of your diverse but invaluable support.

Finally, my heartfelt thanks go to my wonderful Vittoria. You are my companion in deep astrophysical discussions, a patient proofreader, a typography designer, a faithful support during difficult days, and a guide in the best ones. You, my life partner, never failed to support me even when I was not sure of myself. I will never stop thanking you for making our time together the most beautiful ever. There is always a piece of you in everything I am achieving.

Bibliography

- Adams, N. J., Conselice, C. J., Ferreira, L., et al. 2023, MNRAS, 518, 4755, doi: [10.1093/mnras/stac3347](https://doi.org/10.1093/mnras/stac3347)
- Alves de Oliveira, C., Birkmann, S. M., Böker, T., et al. 2018, in Society of Photo-Optical Instrumentation Engineers (SPIE) Conference Series, Vol. 10704, Observatory Operations: Strategies, Processes, and Systems VII, 107040Q, doi: [10.1117/12.2313839](https://doi.org/10.1117/12.2313839)
- Anders, E., & Grevesse, N. 1989, GeoCoA, 53, 197, doi: [10.1016/0016-7037\(89\)90286-X](https://doi.org/10.1016/0016-7037(89)90286-X)
- Arrabal Haro, P., Dickinson, M., Finkelstein, S. L., et al. 2023, ApJL, 951, L22, doi: [10.3847/2041-8213/acdd54](https://doi.org/10.3847/2041-8213/acdd54)
- Behroozi, P., Conroy, C., Wechsler, R. H., et al. 2020, MNRAS, 499, 5702, doi: [10.1093/mnras/staa3164](https://doi.org/10.1093/mnras/staa3164)
- Bernardi, M., Meert, A., Sheth, R. K., et al. 2013, MNRAS, 436, 697, doi: [10.1093/mnras/stt1607](https://doi.org/10.1093/mnras/stt1607)
- Bisigello, L., Caputi, K. I., Colina, L., et al. 2016, ApJS, 227, 19, doi: [10.3847/0067-0049/227/2/19](https://doi.org/10.3847/0067-0049/227/2/19)
- Blumenthal, G. R., Faber, S. M., Primack, J. R., & Rees, M. J. 1984, Nature, 311, 517, doi: [10.1038/311517a0](https://doi.org/10.1038/311517a0)
- Böker, T., Beck, T. L., Birkmann, S. M., et al. 2023, PASP, 135, 038001, doi: [10.1088/1538-3873/acb846](https://doi.org/10.1088/1538-3873/acb846)
- Bond, J. R., Cole, S., Efstathiou, G., & Kaiser, N. 1991, ApJ, 379, 440, doi: [10.1086/170520](https://doi.org/10.1086/170520)
- Bouwens, R. J., Oesch, P. A., Stefanon, M., et al. 2021, AJ, 162, 47, doi: [10.3847/1538-3881/abf83e](https://doi.org/10.3847/1538-3881/abf83e)
- Boylan-Kolchin, M. 2023, Nature Astronomy, 7, 731, doi: [10.1038/s41550-023-01937-7](https://doi.org/10.1038/s41550-023-01937-7)
- Bromm, V., Kudritzki, R. P., & Loeb, A. 2001, ApJ, 552, 464, doi: [10.1086/320549](https://doi.org/10.1086/320549)
- Bruzual, G., & Charlot, S. 2003, MNRAS, 344, 1000, doi: [10.1046/j.1365-8711.2003.06897.x](https://doi.org/10.1046/j.1365-8711.2003.06897.x)
- Bullock, J. S., & Boylan-Kolchin, M. 2017, ARA&A, 55, 343, doi: [10.1146/annurev-astro-091916-055313](https://doi.org/10.1146/annurev-astro-091916-055313)
- Bunker, A. J., Cameron, A. J., Curtis-Lake, E., et al. 2023a, arXiv e-prints, arXiv:2306.02467, doi: [10.48550/arXiv.2306.02467](https://doi.org/10.48550/arXiv.2306.02467)
- . 2023b, arXiv e-prints, arXiv:2306.02467, doi: [10.48550/arXiv.2306.02467](https://doi.org/10.48550/arXiv.2306.02467)
- Byrne, C. M., Stanway, E. R., Eldridge, J. J., McSwiney, L., & Townsend, O. T. 2022, MNRAS, 512, 5329, doi: [10.1093/mnras/stac807](https://doi.org/10.1093/mnras/stac807)
- Calzetti, D., Armus, L., Bohlin, R. C., et al. 2000, ApJ, 533, 682, doi: [10.1086/308692](https://doi.org/10.1086/308692)
- Cappellari, M. 2017, MNRAS, 466, 798, doi: [10.1093/mnras/stw3020](https://doi.org/10.1093/mnras/stw3020)
- . 2023, MNRAS, 526, 3273, doi: [10.1093/mnras/stad2597](https://doi.org/10.1093/mnras/stad2597)
- Carnall, A. C., Leja, J., Johnson, B. D., et al. 2019, ApJ, 873, 44, doi: [10.3847/1538-4357/ab04a2](https://doi.org/10.3847/1538-4357/ab04a2)
- Carnall, A. C., McLure, R. J., Dunlop, J. S., & Davé, R. 2018, MNRAS, 480, 4379, doi: [10.1093/mnras/sty250](https://doi.org/10.1093/mnras/sty250)

- Carnall, A. C., McLure, R. J., Dunlop, J. S., et al. 2023, *Nature*, 619, 716, doi: [10.1038/s41586-023-06158-6](https://doi.org/10.1038/s41586-023-06158-6)
- Carniani, S., Hainline, K., D'Eugenio, F., et al. 2024, arXiv e-prints, arXiv:2405.18485, doi: [10.48550/arXiv.2405.18485](https://doi.org/10.48550/arXiv.2405.18485)
- Castellano, M., Fontana, A., Treu, T., et al. 2022, *ApJL*, 938, L15, doi: [10.3847/2041-8213/ac94d0](https://doi.org/10.3847/2041-8213/ac94d0)
- Charlot, S., & Longhetti, M. 2001, *MNRAS*, 323, 887, doi: [10.1046/j.1365-8711.2001.04260.x](https://doi.org/10.1046/j.1365-8711.2001.04260.x)
- Chatzikos, M., Bianchi, S., Camilloni, F., et al. 2023, *RMxAA*, 59, 327, doi: [10.22201/ia.01851101p.2023.59.02.12](https://doi.org/10.22201/ia.01851101p.2023.59.02.12)
- Chon, S., Hosokawa, T., & Omukai, K. 2021, *MNRAS*, 502, 700, doi: [10.1093/mnras/stab061](https://doi.org/10.1093/mnras/stab061)
- Ciesla, L., Elbaz, D., Ilbert, O., et al. 2023, arXiv e-prints, arXiv:2309.15720, doi: [10.48550/arXiv.2309.15720](https://doi.org/10.48550/arXiv.2309.15720)
- Clarke, C. J., & Bromm, V. 2003, *MNRAS*, 343, 1224, doi: [10.1046/j.1365-8711.2003.06765.x](https://doi.org/10.1046/j.1365-8711.2003.06765.x)
- Conroy, C. 2013, *ARA&A*, 51, 393, doi: [10.1146/annurev-astro-082812-141017](https://doi.org/10.1146/annurev-astro-082812-141017)
- Davé, R., Thompson, R., & Hopkins, P. F. 2016, *MNRAS*, 462, 3265, doi: [10.1093/mnras/stw1862](https://doi.org/10.1093/mnras/stw1862)
- Dayal, P., & Ferrara, A. 2018, *PhR*, 780, 1, doi: [10.1016/j.physrep.2018.10.002](https://doi.org/10.1016/j.physrep.2018.10.002)
- Dekel, A., Sarkar, K. C., Birnboim, Y., Mandelker, N., & Li, Z. 2023, *MNRAS*, 523, 3201, doi: [10.1093/mnras/stad1557](https://doi.org/10.1093/mnras/stad1557)
- Dekel, A., & Silk, J. 1986, *ApJ*, 303, 39, doi: [10.1086/164050](https://doi.org/10.1086/164050)
- D'Eugenio, F., Cameron, A. J., Scholtz, J., et al. 2024, arXiv e-prints, arXiv:2404.06531, doi: [10.48550/arXiv.2404.06531](https://doi.org/10.48550/arXiv.2404.06531)
- Di Cesare, C., Graziani, L., Schneider, R., et al. 2023, *MNRAS*, 519, 4632, doi: [10.1093/mnras/stac3702](https://doi.org/10.1093/mnras/stac3702)
- Dodelson, Scott; Schmidt, F. 2021, Modern cosmology, 2nd edn. (Academic Press)
- Dome, T., Tacchella, S., Fialkov, A., et al. 2024a, *MNRAS*, 527, 2139, doi: [10.1093/mnras/stad3239](https://doi.org/10.1093/mnras/stad3239)
- . 2024b, *MNRAS*, 527, 2139, doi: [10.1093/mnras/stad3239](https://doi.org/10.1093/mnras/stad3239)
- Donnan, C. T., McLeod, D. J., Dunlop, J. S., et al. 2023, *MNRAS*, 518, 6011, doi: [10.1093/mnras/stac3472](https://doi.org/10.1093/mnras/stac3472)
- Dopita, M. A., & Sutherland, R. S. 2003, Astrophysics of the diffuse universe, doi: [10.1007/978-3-662-05866-4](https://doi.org/10.1007/978-3-662-05866-4)
- Efstathiou, G. 2000, *MNRAS*, 317, 697, doi: [10.1046/j.1365-8711.2000.03665.x](https://doi.org/10.1046/j.1365-8711.2000.03665.x)
- Eisenstein, D. J., Johnson, B. D., Robertson, B., et al. 2023, arXiv e-prints, arXiv:2310.12340, doi: [10.48550/arXiv.2310.12340](https://doi.org/10.48550/arXiv.2310.12340)
- Eldridge, J. J., Stanway, E. R., Xiao, L., et al. 2017a, *PASA*, 34, e058, doi: [10.1017/pasa.2017.51](https://doi.org/10.1017/pasa.2017.51)
- . 2017b, *PASA*, 34, e058, doi: [10.1017/pasa.2017.51](https://doi.org/10.1017/pasa.2017.51)
- Fabian, A. C., Celotti, A., & Erlund, M. C. 2006, *MNRAS*, 373, L16, doi: [10.1111/j.1745-3933.2006.00234.x](https://doi.org/10.1111/j.1745-3933.2006.00234.x)
- Faucher-Giguère, C.-A. 2018, *MNRAS*, 473, 3717, doi: [10.1093/mnras/stx2595](https://doi.org/10.1093/mnras/stx2595)
- Faucher-Giguère, C.-A., Lidz, A., & Hernquist, L. 2008, *Science*, 319, 52, doi: [10.1126/science.1151476](https://doi.org/10.1126/science.1151476)
- Ferrara, A. 2024, *A&A*, 684, A207, doi: [10.1051/0004-6361/202348321](https://doi.org/10.1051/0004-6361/202348321)
- Ferrara, A., Pallottini, A., & Dayal, P. 2023, *MNRAS*, 522, 3986, doi: [10.1093/mnras/stad1095](https://doi.org/10.1093/mnras/stad1095)

- Ferruit, P., Jakobsen, P., Giardino, G., et al. 2022, A&A, 661, A81, doi: [10.1051/0004-6361/202142673](https://doi.org/10.1051/0004-6361/202142673)
- Finkelstein, S. L., Bagley, M. B., Arrabal Haro, P., et al. 2022, ApJL, 940, L55, doi: [10.3847/2041-8213/ac966e](https://doi.org/10.3847/2041-8213/ac966e)
- Finkelstein, S. L., Bagley, M. B., Ferguson, H. C., et al. 2023, ApJL, 946, L13, doi: [10.3847/2041-8213/acad4](https://doi.org/10.3847/2041-8213/acad4)
- Fiore, F., Ferrara, A., Bischetti, M., Feruglio, C., & Travascio, A. 2023, ApJL, 943, L27, doi: [10.3847/2041-8213/acb5f2](https://doi.org/10.3847/2041-8213/acb5f2)
- Furlanetto, S. R., & Mirocha, J. 2023, MNRAS, 523, 5274, doi: [10.1093/mnras/stad1799](https://doi.org/10.1093/mnras/stad1799)
- Gardner, J. P., Mather, J. C., Clampin, M., et al. 2006, SSRv, 123, 485, doi: [10.1007/s11214-006-8315-7](https://doi.org/10.1007/s11214-006-8315-7)
- Geen, S., Rosdahl, J., Blaizot, J., Devriendt, J., & Slyz, A. 2015, MNRAS, 448, 3248, doi: [10.1093/mnras/stv251](https://doi.org/10.1093/mnras/stv251)
- Giacconi, R., Zirm, A., Wang, J., et al. 2002, ApJS, 139, 369, doi: [10.1086/338927](https://doi.org/10.1086/338927)
- Giavalisco, M., Ferguson, H. C., Koekemoer, A. M., et al. 2004, ApJL, 600, L93, doi: [10.1086/379232](https://doi.org/10.1086/379232)
- Girelli, G., Pozzetti, L., Bolzonella, M., et al. 2020, A&A, 634, A135, doi: [10.1051/0004-6361/201936329](https://doi.org/10.1051/0004-6361/201936329)
- Gong, Y., Yue, B., Cao, Y., & Chen, X. 2023, ApJ, 947, 28, doi: [10.3847/1538-4357/acc109](https://doi.org/10.3847/1538-4357/acc109)
- Harrison, C. M., Costa, T., Tadhunter, C. N., et al. 2018, Nature Astronomy, 2, 198, doi: [10.1038/s41550-018-0403-6](https://doi.org/10.1038/s41550-018-0403-6)
- Harrison, E. R. 1970, PhRvD, 1, 2726, doi: [10.1103/PhysRevD.1.2726](https://doi.org/10.1103/PhysRevD.1.2726)
- Heringer, E., Pritchett, C., Kezwer, J., et al. 2017, ApJ, 834, 15, doi: [10.3847/1538-4357/834/1/15](https://doi.org/10.3847/1538-4357/834/1/15)
- Isobe, Y., Ouchi, M., Nakajima, K., et al. 2023, ApJ, 956, 139, doi: [10.3847/1538-4357/acf376](https://doi.org/10.3847/1538-4357/acf376)
- Jakobsen, P., Ferruit, P., Alves de Oliveira, C., et al. 2022, A&A, 661, A80, doi: [10.1051/0004-6361/202142663](https://doi.org/10.1051/0004-6361/202142663)
- Jiang, L., Kashikawa, N., Wang, S., et al. 2021, Nature Astronomy, 5, 256, doi: [10.1038/s41550-020-01275-y](https://doi.org/10.1038/s41550-020-01275-y)
- Johnson, B. D., Leja, J., Conroy, C., & Speagle, J. S. 2021, ApJS, 254, 22, doi: [10.3847/1538-4365/abef67](https://doi.org/10.3847/1538-4365/abef67)
- JWST User Documentation. 2016, JWST User Documentation (JDox), JWST User Documentation Website
- Kim, C.-G., Ostriker, E. C., & Kim, W.-T. 2013, ApJ, 776, 1, doi: [10.1088/0004-637X/776/1/1](https://doi.org/10.1088/0004-637X/776/1/1)
- Klypin, A., Poulin, V., Prada, F., et al. 2021, MNRAS, 504, 769, doi: [10.1093/mnras/stab769](https://doi.org/10.1093/mnras/stab769)
- Konrad, S., & Bartelmann, M. 2022, Nuovo Cimento Rivista Serie, 45, 737, doi: [10.1007/s40766-022-00037-y](https://doi.org/10.1007/s40766-022-00037-y)
- Kroupa, P. 2001, MNRAS, 322, 231, doi: [10.1046/j.1365-8711.2001.04022.x](https://doi.org/10.1046/j.1365-8711.2001.04022.x)
- Larson, R. B. 1998, MNRAS, 301, 569, doi: [10.1046/j.1365-8711.1998.02045.x](https://doi.org/10.1046/j.1365-8711.1998.02045.x)
- Larson, R. B., & Tinsley, B. M. 1978, ApJ, 219, 46, doi: [10.1086/155753](https://doi.org/10.1086/155753)
- Lecroq, M., Charlot, S., Bressan, A., et al. 2024, MNRAS, 527, 9480, doi: [10.1093/mnras/stad3838](https://doi.org/10.1093/mnras/stad3838)
- Leitherer, C., Schaerer, D., Goldader, J. D., et al. 1999, ApJS, 123, 3, doi: [10.1086/313233](https://doi.org/10.1086/313233)
- Leja, J., Carnall, A. C., Johnson, B. D., Conroy, C., & Speagle, J. S. 2019, ApJ, 876, 3, doi: [10.3847/1538-4357/ab133c](https://doi.org/10.3847/1538-4357/ab133c)
- Leja, J., Johnson, B. D., Conroy, C., van Dokkum, P. G., & Byler, N. 2017, ApJ, 837, 170,

doi: [10.3847/1538-4357/aa5ffe](https://doi.org/10.3847/1538-4357/aa5ffe)

- Li, Z., Dekel, A., Sarkar, K. C., et al. 2023, arXiv e-prints, arXiv:2311.14662, doi: [10.48550/arXiv.2311.14662](https://doi.org/10.48550/arXiv.2311.14662)
- Looser, T. J., D'Eugenio, F., Maiolino, R., et al. 2023a, arXiv e-prints, arXiv:2302.14155, doi: [10.48550/arXiv.2302.14155](https://doi.org/10.48550/arXiv.2302.14155)
- . 2023b, arXiv e-prints, arXiv:2306.02470, doi: [10.48550/arXiv.2306.02470](https://doi.org/10.48550/arXiv.2306.02470)
- Lovell, C. C., Harrison, I., Harikane, Y., Tacchella, S., & Wilkins, S. M. 2023a, MNRAS, 518, 2511, doi: [10.1093/mnras/stac3224](https://doi.org/10.1093/mnras/stac3224)
- Lovell, C. C., Roper, W., Vijayan, A. P., et al. 2023b, MNRAS, 525, 5520, doi: [10.1093/mnras/stad2550](https://doi.org/10.1093/mnras/stad2550)
- Lyu, J., Alberts, S., Rieke, G. H., et al. 2024, ApJ, 966, 229, doi: [10.3847/1538-4357/ad3643](https://doi.org/10.3847/1538-4357/ad3643)
- Mason, C. A., Trenti, M., & Treu, T. 2023, MNRAS, 521, 497, doi: [10.1093/mnras/stad035](https://doi.org/10.1093/mnras/stad035)
- McLeod, D. J., Donnan, C. T., McLure, R. J., et al. 2024, MNRAS, 527, 5004, doi: [10.1093/mnras/stad3471](https://doi.org/10.1093/mnras/stad3471)
- Meszaros, P. 1975, A&A, 38, 5
- Mirocha, J., & Furlanetto, S. R. 2023, MNRAS, 519, 843, doi: [10.1093/mnras/stac3578](https://doi.org/10.1093/mnras/stac3578)
- Mo, H., van den Bosch, F. C., & White, S. 2010, Galaxy Formation and Evolution
- Morishita, T., Stiavelli, M., Chary, R.-R., et al. 2024, ApJ, 963, 9, doi: [10.3847/1538-4357/ad1404](https://doi.org/10.3847/1538-4357/ad1404)
- Moster, B. P., Naab, T., & White, S. D. M. 2018, MNRAS, 477, 1822, doi: [10.1093/mnras/sty655](https://doi.org/10.1093/mnras/sty655)
- Mutch, S. J., Croton, D. J., & Poole, G. B. 2013, MNRAS, 435, 2445, doi: [10.1093/mnras/stt1453](https://doi.org/10.1093/mnras/stt1453)
- Naidu, R. P., Oesch, P. A., van Dokkum, P., et al. 2022, ApJL, 940, L14, doi: [10.3847/2041-8213/ac9b22](https://doi.org/10.3847/2041-8213/ac9b22)
- Nath, B. B., Vasiliev, E. O., Drozdov, S. A., & Shchekinov, Y. A. 2023, MNRAS, 521, 662, doi: [10.1093/mnras/stad505](https://doi.org/10.1093/mnras/stad505)
- Pacifici, C., Iyer, K. G., Mobasher, B., et al. 2023, ApJ, 944, 141, doi: [10.3847/1538-4357/acacff](https://doi.org/10.3847/1538-4357/acacff)
- Pallottini, A., & Ferrara, A. 2023, A&A, 677, L4, doi: [10.1051/0004-6361/202347384](https://doi.org/10.1051/0004-6361/202347384)
- Perivolaropoulos, L., & Skara, F. 2022, NewAR, 95, 101659, doi: [10.1016/j.newar.2022.101659](https://doi.org/10.1016/j.newar.2022.101659)
- Planck Collaboration, Aghanim, N., Akrami, Y., et al. 2020a, A&A, 641, A1, doi: [10.1051/0004-6361/201833880](https://doi.org/10.1051/0004-6361/201833880)
- . 2020b, A&A, 641, A6, doi: [10.1051/0004-6361/201833910](https://doi.org/10.1051/0004-6361/201833910)
- Press, W. H., & Schechter, P. 1974, ApJ, 187, 425, doi: [10.1086/152650](https://doi.org/10.1086/152650)
- Renzini, A. 2023, MNRAS, 525, L117, doi: [10.1093/mnrasl/slad091](https://doi.org/10.1093/mnrasl/slad091)
- Rodighiero, G., Bisigello, L., Iani, E., et al. 2023, MNRAS, 518, L19, doi: [10.1093/mnrasl/slac115](https://doi.org/10.1093/mnrasl/slac115)
- Rodríguez-Puebla, A., Primack, J. R., Avila-Reese, V., & Faber, S. M. 2017, MNRAS, 470, 651, doi: [10.1093/mnras/stx1172](https://doi.org/10.1093/mnras/stx1172)
- Ronconi, T., Lapi, A., Torsello, M., et al. 2024, A&A, 685, A161, doi: [10.1051/0004-6361/202346978](https://doi.org/10.1051/0004-6361/202346978)
- Sanders, R. L., Shapley, A. E., Kriek, M., et al. 2016, ApJ, 816, 23, doi: [10.3847/0004-637X/816/1/23](https://doi.org/10.3847/0004-637X/816/1/23)
- Schneider, R., & Maiolino, R. 2024, A&A Rv, 32, 2, doi: [10.1007/s00159-024-00151-2](https://doi.org/10.1007/s00159-024-00151-2)
- Scoville, N., Faisst, A., Capak, P., et al. 2015, ApJ, 800, 108, doi: [10.1088/0004-637X/800/2/108](https://doi.org/10.1088/0004-637X/800/2/108)
- Searle, L., Sargent, W. L. W., & Bagnuolo, W. G. 1973, ApJ, 179, 427, doi: [10.1086/151882](https://doi.org/10.1086/151882)

- Seaton, M. J. 1979, MNRAS, 187, 73, doi: [10.1093/mnras/187.1.73P](https://doi.org/10.1093/mnras/187.1.73P)
- Senchyna, P., Plat, A., Stark, D. P., & Rudie, G. C. 2023, arXiv e-prints, arXiv:2303.04179, doi: [10.48550/arXiv.2303.04179](https://doi.org/10.48550/arXiv.2303.04179)
- Sheth, R. K., & Tormen, G. 1999, MNRAS, 308, 119, doi: [10.1046/j.1365-8711.1999.02692.x](https://doi.org/10.1046/j.1365-8711.1999.02692.x)
- Silk, J., Di Cintio, A., & Dvorkin, I. 2014, in Proceedings of the International School of Physics ‘Enrico Fermi’ Course 186 ‘New Horizons for Observational Cosmology’ Vol. 186, Vol. 186, 137–187, doi: [10.3254/978-1-61499-476-3-137](https://doi.org/10.3254/978-1-61499-476-3-137)
- Springel, V., White, S. D. M., Jenkins, A., et al. 2005, Nature, 435, 629, doi: [10.1038/nature03597](https://doi.org/10.1038/nature03597)
- Stanway, E. R., & Eldridge, J. J. 2018, MNRAS, 479, 75, doi: [10.1093/mnras/sty1353](https://doi.org/10.1093/mnras/sty1353)
- Stefanon, M., Bouwens, R. J., Labb  , I., et al. 2021, ApJ, 922, 29, doi: [10.3847/1538-4357/ac1bb6](https://doi.org/10.3847/1538-4357/ac1bb6)
- Steinhardt, C. L., Sneppen, A., Clausen, T., et al. 2023, arXiv e-prints, arXiv:2305.15459, doi: [10.48550/arXiv.2305.15459](https://doi.org/10.48550/arXiv.2305.15459)
- Storey, P. J., & Zeippen, C. J. 2000, MNRAS, 312, 813, doi: [10.1046/j.1365-8711.2000.03184.x](https://doi.org/10.1046/j.1365-8711.2000.03184.x)
- Str  mgren, B. 1939, ApJ, 89, 526, doi: [10.1086/144074](https://doi.org/10.1086/144074)
- Tacchella, S., Dekel, A., Carollo, C. M., et al. 2016, MNRAS, 457, 2790, doi: [10.1093/mnras/stw131](https://doi.org/10.1093/mnras/stw131)
- Tacchella, S., Johnson, B. D., Robertson, B. E., et al. 2023, MNRAS, 522, 6236, doi: [10.1093/mnras/stad1408](https://doi.org/10.1093/mnras/stad1408)
- Trinca, A., Schneider, R., Valiante, R., et al. 2024, MNRAS, 529, 3563, doi: [10.1093/mnras/stae651](https://doi.org/10.1093/mnras/stae651)
- Tsuna, D., Nakazato, Y., & Hartwig, T. 2023, MNRAS, 526, 4801, doi: [10.1093/mnras/stad3043](https://doi.org/10.1093/mnras/stad3043)
- Tumlinson, J. 2006, ApJ, 641, 1, doi: [10.1086/500383](https://doi.org/10.1086/500383)
- van Hoof, P. A. M. 2018, Galaxies, 6, 63, doi: [10.3390/galaxies6020063](https://doi.org/10.3390/galaxies6020063)
- Venditti, A., Graziani, L., Schneider, R., et al. 2023, MNRAS, 522, 3809, doi: [10.1093/mnras/stad1201](https://doi.org/10.1093/mnras/stad1201)
- Walcher, J., Groves, B., Budav  ri, T., & Dale, D. 2011, Ap&SS, 331, 1, doi: [10.1007/s10509-010-0458-z](https://doi.org/10.1007/s10509-010-0458-z)
- Waldron, W. L. 1984, ApJ, 282, 256, doi: [10.1086/162198](https://doi.org/10.1086/162198)
- Weinberg, S. 2008, Cosmology (Oxford University Press)
- Whitler, L., Stark, D. P., Endsley, R., et al. 2023, MNRAS, 519, 5859, doi: [10.1093/mnras/stad004](https://doi.org/10.1093/mnras/stad004)
- Wright, A. H., Robotham, A. S. G., Driver, S. P., et al. 2017, MNRAS, 470, 283, doi: [10.1093/mnras/stx1149](https://doi.org/10.1093/mnras/stx1149)
- Yang, G., Caputi, K. I., Papovich, C., et al. 2023, ApJL, 950, L5, doi: [10.3847/2041-8213/acd639](https://doi.org/10.3847/2041-8213/acd639)
- Zavala, J. A., Buat, V., Casey, C. M., et al. 2023, ApJL, 943, L9, doi: [10.3847/2041-8213/acacf](https://doi.org/10.3847/2041-8213/acacf)
- Zeldovich, Y. B. 1972, MNRAS, 160, 1P, doi: [10.1093/mnras/160.1.1P](https://doi.org/10.1093/mnras/160.1.1P)
- Ziparo, F., Ferrara, A., Sommovigo, L., & Kohandel, M. 2023, MNRAS, 520, 2445, doi: [10.1093/mnras/stad125](https://doi.org/10.1093/mnras/stad125)